The Pennsylvania State University

The Graduate School

PHYSICS AND APPLICATIONS OF EXCEPTIONAL SURFACES

A Dissertation in

Engineering Science and Mechanics

by

Sina Soleymani

Submitted in Partial Fulfillment
of the Requirements
for the Degree of

Doctor of Philosophy

December 2021

The dissertation of Sina Soleymani is submitted for review of the following:

Sahin K. Ozdemir
Associate Professor of Engineering Science and Mechanics
Dissertation Advisor
Chair of Committee

Shengxi Huang
Assistant Professor of Electrical Engineering and Biomedical Engineering

Parisa Shokouhi
Associate Professor of Engineering Science and Mechanics

Melik C. Demirel
Huck Chair in Biomimetic Materials; Pearce Professor of Engineering

Albert Segall
Professor of Engineering Science and Mechanics
Graduate Officer of Engineering Science and Mechanics

ABSTRACT

In this dissertation, I present my theoretical and experimental research about exceptional points, its applications in optics, and the experimental realization of the exceptional surface concept. Whispering gallery mode microresonators which are the platform of our study is briefly discussed, and their characterization methods are presented. Non-Hermitian photonics and related phenomena and the background are discussed briefly. The exotic features of non-Hermitian physics and the spectral degeneracies known as exceptional points are explained and the design of a resonator-based photonic system which allows tuning the system controllably to and from EPs is demonstrated via creating non-Hermiticity via unidirectional coupling between two optical modes of the resonator. We have demonstrated, for the first time, chiral and degenerate perfect absorption on exceptional surfaces and studied thermal behavior of WGM microresonators on the exceptional surfaces. In addition to exceptional surfaces and chiral perfect absorption, we investigated theoretically optical forces in non-Hermitian systems, in particular in a parity-time symmetric coupled waveguide system. First, we utilized generalized Wigner-Smith operator and eigenmode optimization methods to maximize optical forces on a nanoparticle in a Hermitian coupled waveguide system confirming that these two methods give similar results. Since Wigner-Smith operator method is not applicable in non-Hermitian settings, we use eigenmode optimization method in PT-symmetric coupled waveguides system to demonstrate optimal forces and their control. I have also contributed to the theoretical efforts of two collaborative studies. In the first one, we have studied optomechanical coupling in a microbottle resonator to achieve high mechanical frequency and quality factors for room temperature quantum optomechanics. In the second one, we studied exceptional points in the tunable collective light-matter interactions in a system of a Terahertz cavity field coupled to molecular vibrations.

TABLE OF CONTENTS

LIST OF FIGURES

ACKNOWLEDGEMENTS

I would like to express my deep appreciation and gratefulness to my advisor, Prof. Sahin Kaya Ozdemir for his support, guidance, and patience throughout my dissertation. He has provided the necessary resources, equipment, and space to explore novel ideas and been a source of motivation for me to perform high impact research. I will always appreciate and remember his countless motivational support and assistance to acquire and master various experimental and theoretical skills during my studies. Prof. Ozdemir supported my progress in gaining the micro/nano fabrication skills in the Pennsylvania States University's nanofabrication facility which is one of the best facilities in the nation.

I would like to thank members of the PhD exam committee Prof. Melik C. Demirel, Prof. Parisa Shokouhi, and Prof. Shengxi Huang for reviewing this thesis, their comments, suggestions, and support which have been useful and sincerely appreciated.

I have greatly enjoyed interacting with students and post-docs R. Neuweiler, D. Peng, J. Nicastro, and Dr. Mohammad Mokim in our group, as well as visiting scientists and professors, Dr. H. Yilmaz, Prof. Takashi Yamamoto, Kevin Pichler. I thank them for their help and many interesting discussions and conversations.

It was a pleasure to collaborate with Prof. Ramy El-Ganainy and Dr. Qi Zhong from Michigan Tech University. I am grateful for their support and hospitality during my visit to Michigan Tech, and for many simulating discussions throughout our collaboration. I would like to thank Prof. Stefan Rotter and Kevin Pichler of Vienna Tech University, Prof. Coskun Kocabas of the University of Manchester, and Prof. Takashi Yamamoto of Osaka University for fruitful collaborations and their support and help during my dissertation

Funding Acknowledgment: I would like to thank National Science Foundation (NSF) for their support during my Ph.D. program.

Last but not least, I want to thank my family, my parents and my sisters for their love, continuous support, and their patience during my years of absence from home. Without their support none of these would be accomplished. It is to them I want to dedicate this thesis.

Sina Soleymani

Chapter 1

Introduction

1.1 Background

Physical systems can be broadly classified into two as Hermitian corresponding to systems completely isolated from their surroundings and non-Hermitian corresponding to systems exchanging energy, matter or information with their surroundings. Physics of light-matter interactions has been traditionally studied within Hermitian settings. Revisiting this physics in non-Hermitian settings opens up new theoretical and experimental opportunities which may lead to functional devices and processes which cannot be observed in Hermitian settings or may lead to enhanced functions. Many interesting features of Hermitian and non-Hermitian systems emerge in the vicinity of spectral degeneracies. Hermitian degeneracies are referred to as diabolic points (DPs) where the eigenvalues are degenerate, but the corresponding eigenvectors are orthogonal. Non-Hermitian spectral degeneracies are known as exceptional points (EPs), where not only the eigenvalues but also the associated eigenvectors are degenerate [1-6]. Since, the experimental study of the optical systems at the singularity is almost very difficult, and most of the works has been done so far are in the vicinity of the EPs, here we offer experimental realization of EPs called Exceptional Surfaces (ESs), which are essentially a surface of the EPs. Creating an ES makes our optical system robust against fabrication imperfections and experimental difficulties, therefore, we can feasibly study light and matter interactions at this exotic surface, with characteristics of the EP [10-21].

Our toolbox for studying ESs is whispering gallery mode microresonators, which have been used for optical sensing, due to their high-quality factor, high intensity and therefore significant light-matter interactions. Additionally, microresonators are an excellent platform for

detecting any temperature and humidity change in the environment. We use tapered fibers to couple the light to microresonators and fiber optics components to create the ESs [22-40].

1.2 Thesis Outline

In chapter 2, we introduce whispering gallery mode (WGM) microresonators because these resonators are used as the platform for our study of non-Hermitian photonics. We discuss fabrication and characterization of various types of resonators, their mode structure, field distributions, mode volumes, and loss mechanisms. Moreover, we discuss coupling light into and out of WGM resonances using tapered fibers. We introduce coupled mode theory (CMT) which describes the coupling between clockwise (CW) and counterclockwise (CCW) modes of WGM resonators.

In chapter 3 we present an overview of studies in the field of non-Hermitian photonics, including parity-time (PT) symmetric systems. We will also introduce how PT-symmetric systems are designed and how one can tune an optical system to its EPs. Furthermore, we discuss some of the applications of non-Hermitian systems, such as observation of nonreciprocal light transmission in a PT-symmetric WGM resonator system and the demonstration of enhanced response of a resonator to perturbations when it is operated at an EP.

Chapter 4 describes the experimental realization of exceptional surfaces (ESs) which is the main result of this thesis. We will present the results of numerical simulations and our experiments performed using an on-chip microsphere resonator. In this study, ES are created by achieving a unidirectional coupling between CW and CCW modes of the WGM resonator.

Chapter 5 is dedicated to the discussion and experimental demonstration of chiral perfect absorption on an ES. Quartic absorption spectrum at an EP is demonstrated for the first time in this study.

Chapter 6 presents our theoretical and experimental results on thermal response of WGMs when the resonator is operated on an ES.

In chapter 7 we will present our collabrative theoretical work on optical forces in PT-symmetric coupled waveguides. We discuss optical forces acting on a particle in this system at the EP, in the exact PT-symmetric phase, and in the broken PT-symmetric phase.This work is a collaboration with Prof. Rotter's group.

Chapter 2

Whispering Gallery Mode Microresonators

Whispering Gallery Mode (WGM) microresonators are outstandingly high-quality factor resonators, which enable enhanced light-matter interactions due to their long photon lifetimes (spectral confinement) and very small mode volumes (spatial confinement). These make WGM resonators suitable for studying fundamental of light-matter interactions at a theoretical level as well as for building new functionalities and devices for applications. For example, WGM resonators have proven to be excellent systems for cavity optomechanics [41], spectral filtering [75], (bio)sensing [76], quantum electrodynamics (QED) [28]. This chapter contains a brief overview of WGM resonators, their fabrication, characterization, and modelling.

2.1 Introduction

Whispering gallery modes was introduced by Lord Rayleigh to explain why the whispers on one side could be heard by others on the other side of the dome in St Paul's Cathedral in 1878 [42]: Sound waves propagate along the circular boundary of the domes through total internal reflection (TIR) The same concept has been realized in optics by fabricating photonic structures with circular boundaries from materials whose refractive index is higher than the refractive index of the surrounding environment (e.g., typically air $n = 1$ or water $n = 1.33$). In addition to this refractive index contrast, the radius of the structure should be large enough to locally satisfy the condition for TIR. When these are satisfied, light inside the resonator will reflect back into the resonator from the boundary and therefore circulate inside it and close to its boundaries. Since it is difficult to satisfy perfect TIR along a circular boundary with the available material systems, a portion of the field inside the resonator leaks out into the surroundings. This field is referred to as

an evanescent field and its intensity exponentially decreases with the distance from the boundary of the resonator. Thus the confinement of light inside the resonator depends on several parameters such as the shape of the resonator, refractive index of the material used to fabricate the resonator, radius of the structure, and the wavelength of the light. Resonance condition for a structure with circular boundary such as a WGM resonator can be written as

$$m\lambda = 2\pi R n_{eff} \qquad (2.1)$$

Where λ is the wavelength of the light, R is the radius of the microresonator, n_{eff} is the effective refractive index of the WGM which takes into account the refractive indices of the resonator and the surrounding environment, and m is a positive integer number.

Figure. 2-1 presents the SEM image of a microdisk resonator we fabricated, a ray optics illustration of the total internal reflection (TIR) and light propagation in a microresonator, and field distribution inside the microresonator obtained using Finite element simulation in COMSOL Multiphysics, which clearly shows the confinement of the field along the resonator boundary. Figure. 2-2 presents various shapes and geometries that have been used and studied as WGM microresonators.

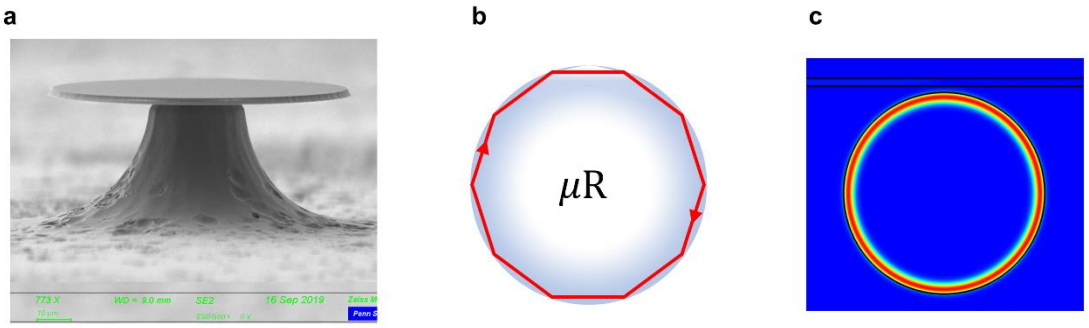

Figure 2-1: (a) SEM image of a microdisk resonator, (b) Ray optics illustration of the light propagation and TIR. (c) Electric field distribution of the transverse electric mode inside a microresonator obtained using COMSOL simulation.

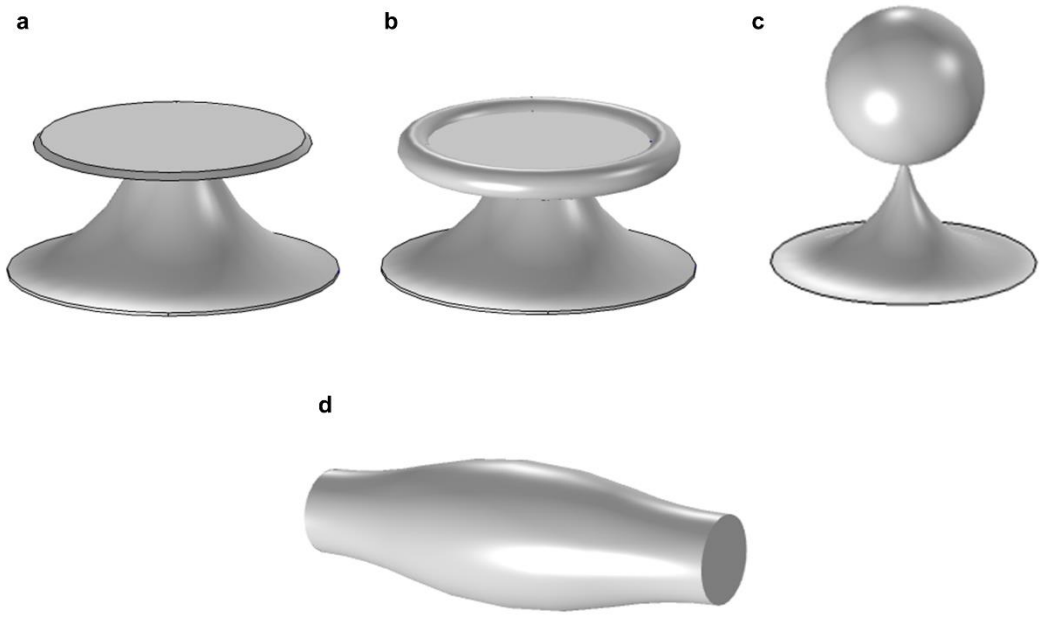

Figure 2-2: Typical geometries used as WGM microresonators. (a) microdisk, (b) microtoroid, (c) microsphere, and (d) microbottle.

2.2 Fabrication of WGM Microresonators

On-chip microdisk, microtoroid and microsphere resonators are fabricated using standard microfabrication techniques. In our studies, we have used silica resonators. We start with silica on silicon wafers. The thickness of the silica layer plays a role in the quality factor of the final resonator [43]. We started with $4\mu m$ silica grown on a <100> prime, float zone, intrinsic silicon wafer. Basic fabrication steps are as follows [77]: 1) Prebaking at 110 degrees for 3 minutes; 2) An adhesion promoter (HMDS) is spin-coated on the surface 3000 rpm for 30 seconds; 3) A layer of positive photoresist (Shipley1813) is coated on the wafer by spin coating at (4000 rpm for 45 seconds); 4) After pre-baking (soft bake) at 110 degrees for 1 minute which drives off excess photoresist solvent, photolithography is performed by exposing the wafers with UV light (at $8mW/cm^2$

intensity for 9.5 seconds) through a mask with circular rings; 5) Wafer is then subject to developing (with CD26 for 1 min, then rinsed with DI water and dried with Nitrogen). The wafer is then hard-baked at 125 °C for 5 minutes so that the photoresist remained after developing solidifies to make a more durable layer; 6) The wafer is then etched using hydrofluoric acid (BOE1:6 with the etching rate of 80nm/min) until all silica is removed, leaving behind silica disks covered with photoresist. This process can be monitored visually making use of the fact that silicon is hydrophilic and silica is hydrophobic. Since HF etching is isotropic, the resulting silica disks have wedge shaped side-wall profiles. The wedge angle is dependent on the amount of undercutting of the photoresist pads and thus on the etching rate and time. After etching the wafer is cleaned with acetone, methanol and DI water. 7) The wafer is cleaved into smaller sizes (0.25 inch in 1 inch) so that in each chip there is a single row of disks. To protect the structures from particle contamination during cleaving, a photoresist layer is spin coated followed by soft-baking at 110 for 1 minute before cleaving. After cleaving the samples are cleaned in acetone for 5 minutes, rinsed in methanol and DI water and dried using high purity nitrogen to ensure that photoresist is completely removed. 8) To isolate the silica disks from the silicon substrate, we employed dry etching with XeF_2 or SF_6. This creates an undercut structure in the form of silica disks standing on silicon pillars. The amount of undercut is controlled by the XeF_2 (or SF_6) etching process (In each cycle of etching, a sample with a row of resonators is exposed to 3 Torr of XeF_2 for 30 seconds, and then the etching chamber is purged via Nitrogen for 1 minute, each cycle etches 2 microns of silicon isotropically) and size of the disk. The resulting structures are referred to as microdisk. Figure 2-3 presents an illustration of main steps of the fabrication process.is presenting the fabrication steps of the on-chip microresonators.

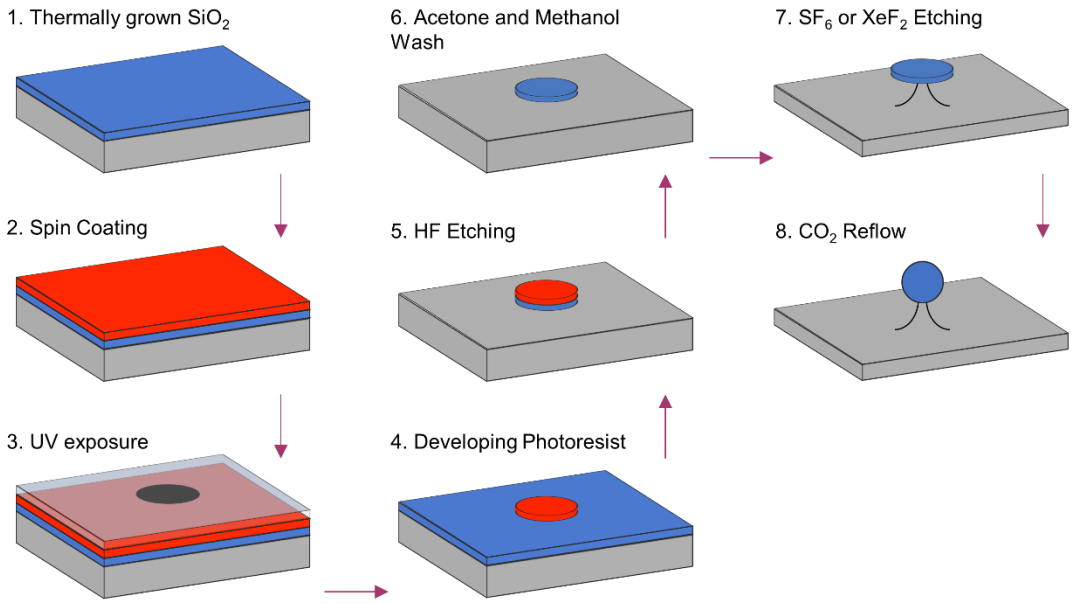

Figure 2-3: Fabrication steps of on-chip microresonators. Blue, red and grey colors represent SiO_2, photoresist, and Si materials, respectively.

These on-chip microdisks can then be turned into microtoroids or microsphere resonators through a reflow process using CO_2 laser (Synrad, $10-50\ MW/m^2$ controlled via pulse width modulation) which selectively heat and reflow the undercut silica disks without affecting the silicon support pillars. A CO_2 laser is used because the silica has a very strong absorption line within the emission band of CO_2 laser (~10μm). Thus, irradiation of the structure melts silica disk along the periphery. During this process silicon pillar stays cooler and serves as a heat sink. Due to the melting of silica disk and the presence of surface tension, the disk shrinks in size forming a toroidal shape boundary. As the irradiation continues, the disk shrinkage continues and finally comes to a stop when the absorbed power becomes very small (i.e., because the effective area and cross-section decreases with shrinking) so that there is no change anymore. Thus, reflow process is self-

terminating process. One can stop the reflow before this self-terminating point. The reflow process is controlled by the amplitude, pulse shape, and duration of the function generator controlling the laser.

By properly choosing the cross-section of the silicon pillar where it connects to the silica, the CO_2 laser parameters, the reflow process can be used to produce microtoroids, or microsphere resonators. For smaller pillar sizes the chance of obtaining the microsphere is higher. Figure. 2-4 is demonstrating a setup to fabricate the silica microsphere or microtoroid resonators via CO_2 laser.

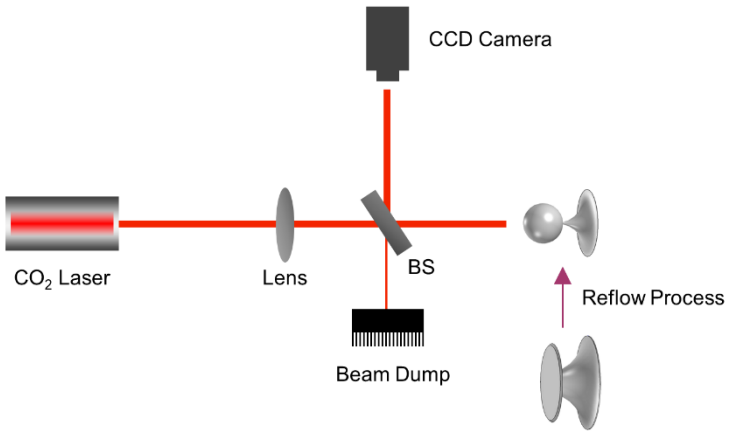

Figure 2-4: The setup used for reflow of silica microdisks to fabricate on-chip microtoroids and microspheres.

The same reflow process with CO_2 laser can be used to fabricate microsphere resonators at the tip of silica fibers. For this purpose, we start with a silica fiber (with diameter of 125 microns). After stripping to remove the plastic jacket, we clean the fiber with IPA followed by cleaving. Then the tip of the fiber is irradiated with CO_2 laser. The melting of the silica and the surface tension then produce a microsphere at the tip of the fiber. The size of the microsphere could be tuned by the reflow parameters. One can start with a fiber tip which is tapered and then reflow this tapered

fiber with CO2 irradiation. The starting size of the tapered tip will determine the final size of the microsphere together with the irradiation parameters.

Microbottle resonators are fabricated in two different ways. In the first method, the stripped and cleaned portion of a silica fiber is irradiated with CO_2 laser, which results in a bulge which is then used as resonator. During this process, one can stretch or compress the fiber, too, as well as start with a fiber section which is already tapered to a certain diameter. The second method involves heating and pulling of a silica fiber on hydrogen flame. First, one side of stripped fiber is heated and pulled (i.e., similar to tapered fiber fabrication step). Then the hydrogen flame is moved along the fiber to another tapered location on the fiber, and this new point is heated while the fiber is pulled. Heating and pulling at two different points on the fiber creates two bottle necks between which there is a bulged region that serves as a microbottle resonator. The distance between two heating and pulling regions determines the final diameter of the bulged region, length of the resonator, its quality factor (Q) and free spectral range (FSR). Figure. 2-6 demonstrates the heating and pulling setup used for the fabrication of microbottle resonators. Additionally, in Fig. 2-7 the examples of fabricated microresonators are presented.

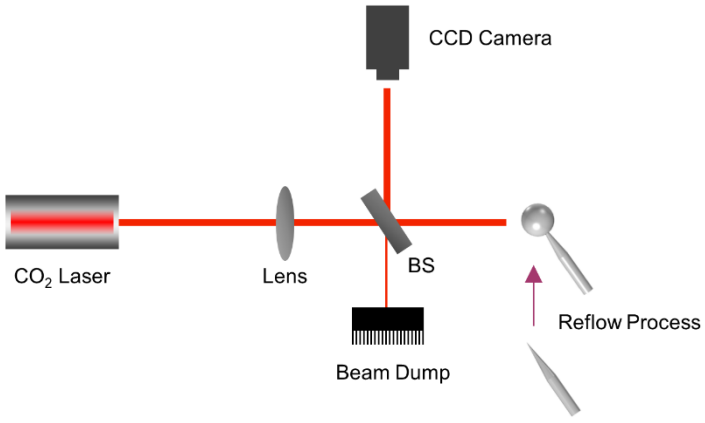

Figure 2-5: Setup for fabricating microspheres at the tip of a silica fiber.

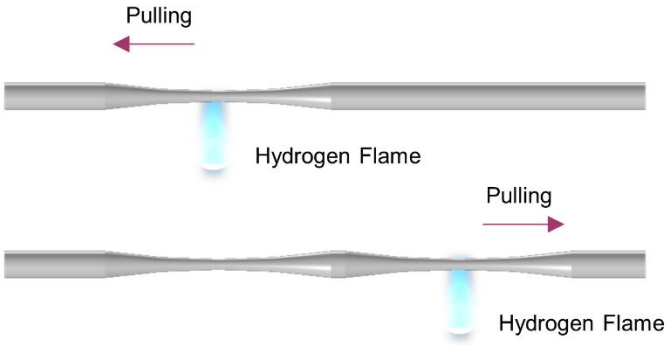

Figure 2-6: Heat and pull method for fabricating microbottle resonators.

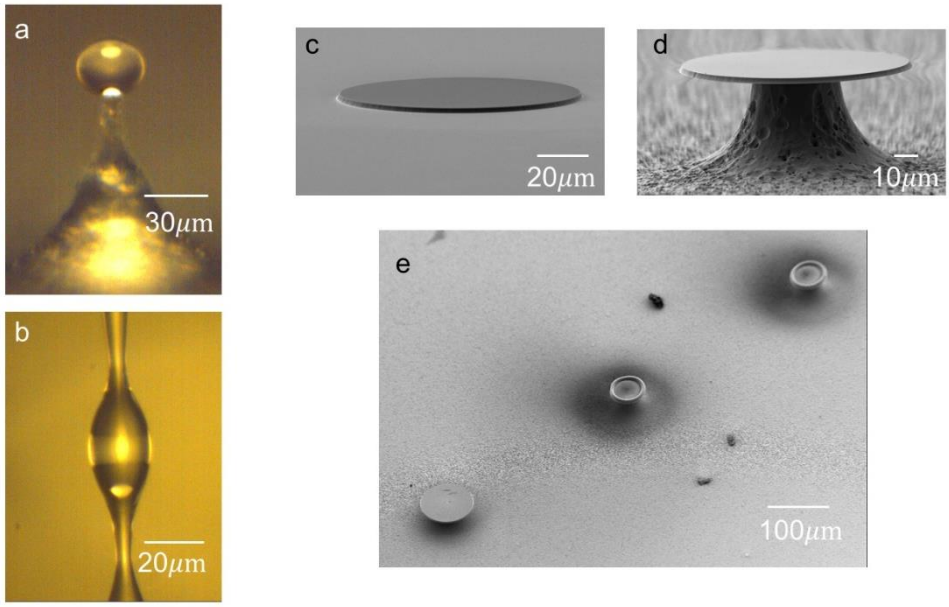

Figure 2-7: Examples of fabricated microresonators. (a) Optical microscope image of on chip microsphere. (b) Optical microscope image of microbottle resonator. (c) SEM image of an on chip microdisk before XeF_2 etching. (d) SEM image of an on chip microdisk resonator after XeF_2 etching. I SEM image of microdisk resonators before CO_2 reflow and microtoroid resonators after CO_2 reflow.

2.3 Tapered Fiber Fabrication and Coupling Methods

One can couple light in and out of WGM resonators only evanescently. Several techniques have been utilized for this purpose, such as prisms, waveguides, half-block fibers, scatterers, or tapered fibers [77]. Easy fabrication of the tapered fibers, controllability of the position of microresonator with respect to the tapered fiber, and the highest coupling efficiency among all coupling methods are advantages of tapered fiber-based coupling. Figure. 2-8 illustrates the heat-and-pull method for fabricating tapered fibers. In this method, a part of a commercially available silica optical fiber (cladding diameter of $125\mu m$ and core diameter of $9\mu m$) is first stripped of the protective coating and cleaned using IPA. The cleaned part is heated via hydrogen flame (with hydrogen flow of $\sim 250 ml/min$) and slowly pulled towards left and right at $0.075 mm/sec$ using stepper motors. This heating and pulling process leads to adiabatic and gradual shrinking of the diameter of the tapered fiber. This tapered section allows the light inside the fiber leak outside evanescently. The chip containing the resonator is placed on a 3D piezo stage which allows the tune the position of a resonator with respect to the tapered fiber. Once the proper distance and location is achieved, a portion of the light inside the fiber couples into the resonator mode evanescently from the tapered section. After a roundtrip time inside the resonator a portion of the light inside the resonator couples back into the fiber. Figure 2-9 presents the optical microscope images of tapered fiber coupled microresonators.

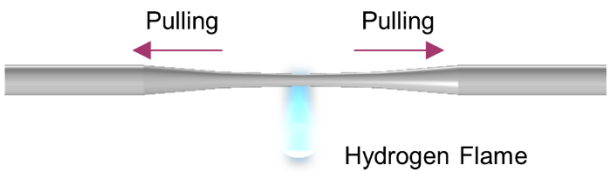

Figure 2-8: Tapering fiber by heating and pulling from both sides.

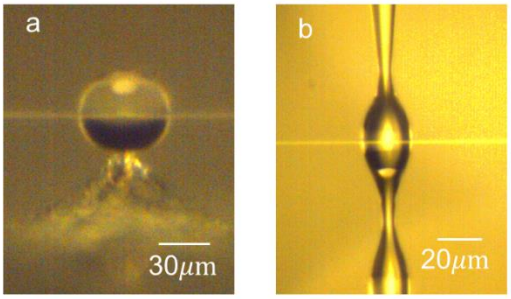

Figure 2-9: Optical Microscope images of (a) microsphere resonator coupled to tapered fiber, (b) microbottle resonator coupled to tapered fiber.

2.4 Loss, Quality Factor, Free Spectral Range and Photon Lifetime

In order to characterize WGM microresonators, it is essential to consider several important features, such as the quality factor (Q), free spectral range (FSR) and the photon life time inside the resonator. These features are mainly determined by the optical losses of the WGM of the resonator.

2.4.1. Loss sources

There are various loss mechanisms in a resonator that affect the spectral and spatial confinement of light inside the resonator. A mode with larger loss has a smaller quality factor and shorter photon lifetime. Typical loss mechanisms [44] are material absorption loss γ_{abs}, surface roughness induced scattering loss γ_{sca}, radiation loss γ_{rad} which originates from the size of the resonator (i.e., the smaller the size the more difficult to achieve total internal reflection for a resonator material of given refractive index or a smaller resonator will have higher radiation loss for a longer wavelength light), and taper-resonator coupling loss γ_{coup}. Additionally, a larger

silicon pillar may have an overlap with the resonator mode in silica opening a large leakage route from low refractive index silica region to a high refractive index silicon region. The choice of the resonator material depends on its suitability for fabrication and its loss at the spectral band of interest. For example, silica its suitable for the telecommunication band due to its low loss in that region. If a silica resonator is used in the visible band, the loss will be higher.

Absorption, scattering, and radiation losses are often referred to as intrinsic losses while the coupling losses are referred to as external losses. Coupling loss (or external loss γ_{ex}) can be controlled by varying the distance between the tapered fiber and the resonator. The progress in fabrication technologies have allowed to engineer the shapes and sizes of WGM resonators to have reduced losses [43] leading to higher quality factors and longer photon lifetimes. Measuring the transmission spectra of a resonator using a tunable laser and recording the transmitted light at the end of the fiber by a detector helps to quantify the overall loss of the resonance mode. The linewidth of the resonance in the transmission spectra is a signature of the total loss of the WGMs. The intrinsic loss of a resonator is fixed when the fabrication is finished, and the wavelength band of interest is fixed. In contrast, coupling loss or the external loss can be varied by changing the coupling distance between the WGM and the tapered fiber. Thus, by tuning the gap between the resonator and the tapered fiber, one can make the external loss larger or smaller than the intrinsic loss.

2.4.2. Quality Factor

Quality factor (Q) of a resonance mode is a figure of merit to characterize the loss. Quality factor, in simple words, is the ratio of the stored energy to the dissipated energy at each roundtrip inside the resonator. Once a resonance is measured in the transmission spectrum, one can estimate its frequency and its full-width at half-maximum (FWHM) which then can be used to calculate the quality factor as:

$$Q = \frac{\omega_0}{\Delta\omega} = \frac{\lambda_0}{\Delta\lambda} \qquad (2.2)$$

where $\Delta\omega$ and $\Delta\lambda$ are the measured linewidth of the resonance (i.e., FWHM) in frequency and wavelength spectra, respectively, and ω_0 and λ_0 are the resonance frequency and wavelength. If the loss incurred on the light field during the propagation inside the resonator is α, the quality factor of the resonator can be written as

$$Q = \frac{2\pi n}{\alpha\lambda_0} \qquad (2.3)$$

where n, and λ are the refractive index of the material used to fabricate the resonator and the resonance wavelength, respectively.

Measured quality factor Q_{loaded} of a resonance mode is determined by the combined effect of coupling loss (external loss) and the intrinsic loss (i.e., sum of the absorption, radiation, and scattering losses) as [45]:

$$\frac{1}{Q_{loaded}} = \frac{1}{Q_{ex}} + \frac{1}{Q_0} \quad (2.4)$$

where Q_0 is associated with the intrinsic quality factor of the microresonator (i.e., quality factor due to intrinsic losses $\gamma_0 = \gamma_{abs} + \gamma_{rad} + \gamma_{sca}$, satisfying $\gamma_0 = 1/Q_0$) and $Q_{ex}$is associated with the external quality factor and determined by the external loss or coupling loss (i.e., $\gamma_{ex} = 1/Q_{ex}$). From the expression in Eq. (2.4), it is clear that if the coupling losses are minimized approaching zero, the loaded quality factor will approach to the intrinsic quality factor (i.e., $Q_{loaded} \rightarrow Q_0 \; if \; Q_{ext} \rightarrow \infty$). Similarly, when $Q_{ext} = Q_0$, we have $Q_{loaded} = Q_0/2 = Q_{ext}/2$. Thus, one can tune the loaded quality factor by varying the external quality factor. This is achieved by varying the distance between the resonator and the waveguide (tapered fiber). One can broadly divide coupling regions into three regimes: 1) Undercoupling regime where external coupling losses are much smaller than the intrinsic losses, that is $Q_{ext} \gg Q_0$, leading to $Q_{loaded} \cong Q_0$. Thus,

measurements in the deep undercoupling regime will provide a good estimate of the intrinsic quality factor of the resonance mode. 2) Critical coupling where external coupling losses are equal to the intrinsic losses, that is $Q_{ext} = Q_0$, leading to $Q_{loaded} = Q_0/2 = Q_{ext}/2$. Critical coupling is identified as the resonator-waveguide gap at which the transmission becomes zero. 3) Overcoupling regime where the distance between the resonator and the taper is minimal, leading to $Q_{ext} \ll Q_0$. In this regime the loaded quality factor is mainly determined by the coupling losses.

2.4.3. Photon Lifetime in WGM Microresonators

Losses in a resonance mode determine how long a photon will circulate inside the resonator until it is lost. This time scale is referred to as the photon lifetime and is defined as the time required for the energy inside the resonator to reach 1/e of its maximum value. If the propagation loss is α, the propagation length is given as $L_p = 1/\alpha$ from which one can calculate the photon lifetime as

$$\tau = \frac{nL_p}{c} = \frac{n}{\alpha c} \quad (2.5)$$

where c is the speed of light and n is the refractive index of the resonator material. Similarly, it is possible to calculate the photon life time from the quality factor of the resonator as [46]

$$\tau = \frac{Q}{\omega_0} \quad (2.6)$$

The photon lifetime is also related to the decay rate via $\tau = 1/\gamma_t$.

2.4.4. Free Spectral Range

The free spectral range (FSR) of a resonator is the frequency or wavelength difference between two successive transmission peaks or dips is given by,

$$\Delta f_{FSR} \approx \frac{\lambda_0^2}{n2\pi R} \quad (2.7)$$

which implies that as the size of the microresonator increases, its FSR decreases. For many applications such as sensing, it is crucial to have larger FSR. But this means that the resonator should be made smaller which in turn may lead to excess radiation loss. So, when designing and operating a resonator, these issues should be carefully checked and optimized.

2.4.5. Finesse

Finesse is the measurement of the narrowness of the resonance with respect to its FSR:

$$F = \frac{\Delta f_{FSR}}{FWHM} \qquad (2.8)$$

It is clear that resonances with high quality factor (i.e., narrower FWHM) and larger FSR have high fineness.

2.5 Mode Volume and Mode Distribution

2.5.1 Mode Volume in WGM Microresonators

While the quality factor quantifies the spectral confinement of light inside a resonator, mode volume quantifies its spatial confinement. It is typically desired to have resonators with smaller mode volumes but higher quality factors. Higher quality factor mean longer photon lifetime and smaller mode volume means higher intensity. Thus, a higher Q/V leads to stronger light matter interactions. The mode volume of a resonator is found by the ratio of the spatial integration of the field intensity to the peak intensity of the mode [47]:

$$V = \frac{\int \varepsilon(\boldsymbol{r})\left|\overrightarrow{E(\boldsymbol{r})}\right|^2 dV}{\max\left(\varepsilon(\boldsymbol{r})\left|\vec{E}(\boldsymbol{r})\right|^2\right)} \qquad (2.9)$$

where $\vec{E}$ is the electric field.

$$\left|\vec{E}\right|^2 = \vec{E}_x^2 + \vec{E}_y^2 + \vec{E}_z^2 \qquad (2.10)$$

and the integration is evaluated over all space which includes the regions the evanescent field extends to. Typically, resonators with smaller dimensions and higher refractive indices have smaller mode volumes.

2.5.2 Mode Distribution

WGM microresonators depending on their shapes and dimensions can exhibit distinct mode distributions. Fundamental modes typically have the highest confinement and smallest mode volume when compared to the higher order modes. Therefore, it is always preferred to use the fundamental mode in experiments involving light-matter interactions. Smaller microresonators present fewer orders of mode distributions. Figure 2-10. Presents mode distributions obtained with Lumerical for different microresonators.

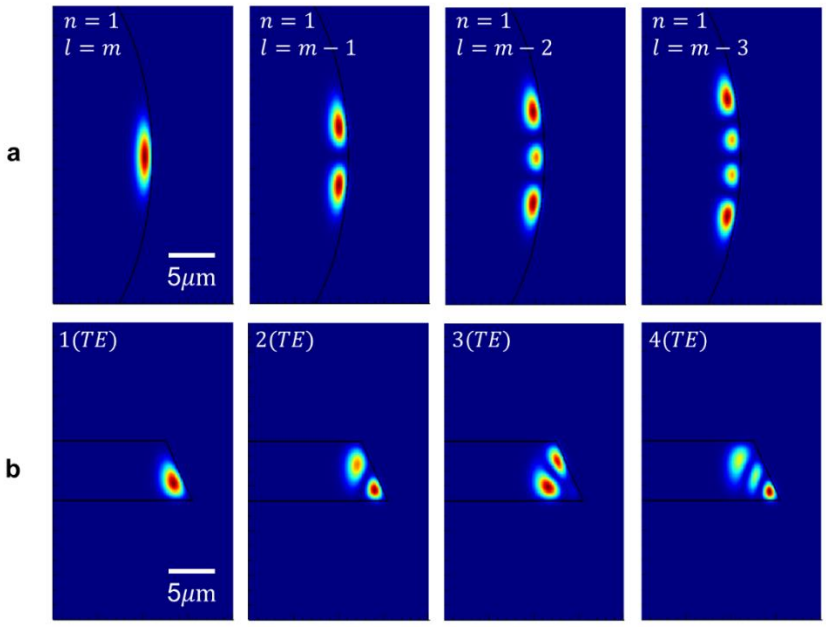

Figure 2-10: Fundamental and higher order mode profiles for (a) silica microsphere resonator with a diameter of $60\mu m$ and (b) a silica microdisk resonator with diameter of $100\mu m$. l, n are angular and radial mode numbers, respectively, and m is the relative index of refraction [78].

2.6 Resonator-waveguide coupling

The time evolution of the intracavity field (i.e., field inside the resonator)a in a waveguide coupled resonator system (Figure 2-11) is expressed as [45]

$$\frac{da}{dt} = -\left(i\omega_0 + \frac{\gamma_0+\gamma_{ex}}{2}\right)a - \sqrt{\gamma_{ex}}a_{in} \qquad (2.11)$$

where the γ_{ex} and γ_0 are the coupling decay rate and the intrinsic decay rate, respectively, ω_0 is the resonance frequency, and a_{in} is the input field.

The output field a_o is described by the input-output relation

$$a_o = a_{in} + \sqrt{\gamma_{ex}}a \qquad (2.12)$$

Transmission normalized to the input field can be calculated using

$$T = \frac{|a_{out}|^2}{|a_{in}|^2} \qquad (2.13)$$

In the steady state condition and after applying the Fourier transformation we obtain the intracavity field as

$$\left(i\Delta\omega - \left(\frac{\gamma_0+\gamma_{ex}}{2}\right)\right)a - \sqrt{\gamma_{ex}}a_{in} = 0 \qquad (2.14)$$

$$a = \frac{\sqrt{\gamma_{ex}}a_{in}}{i\Delta\omega - \left(\frac{\gamma_0+\gamma_{ex}}{2}\right)} \qquad (2.15)$$

where $\Delta\omega = \omega - \omega_0$ is detuning between the resonance frequency and the probing light field. Using Eq. (2.15) in the input-output relation in Eq. (2.12), we find the transmission as,

$$T(\Delta\omega) = \left|1 + \frac{\gamma_{ex}}{i\Delta\omega - \left(\frac{\gamma_0+\gamma_{ex}}{2}\right)}\right|^2 = 1 - \frac{\gamma_{ex}\gamma_0}{\Delta\omega^2 + \left(\frac{\gamma_0+\gamma_{ex}}{2}\right)^2} \qquad (2.16)$$

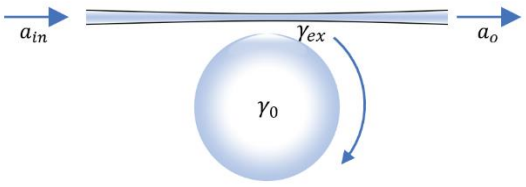

Figure 2-11: Waveguide coupled resonator system. In our experiments, the coupling waveguide is a tapered fiber.

When the frequency of the probing laser is spectrally away from the resonance frequency (i.e., $\Delta\omega \rightarrow \infty$), transmission becomes 1. Moreover, once the resonator is fabricated intrinsic loss is fixed (i.e., $\gamma_0 = constant.$) and therefore the gap distance between the resonator and tapered fiber determines the transmission value at the zero-detuning frequency (i.e., $\Delta\omega = 0$). Hence, as we discussed previously, we can define three distinct coupling conditions as undercoupling, critical coupling, and overcoupling based on the comparative values of intrinsic and external decay rates. At the undercoupling regime, the coupling induced decay rate is smaller than the intrinsic loss of the microresonator, $\gamma_0 > \gamma_{ex}$, and the gap distance between the resonator and fiber taper is large. When the intrinsic loss value is much bigger than the external loss, the coupling regime is called as the deep undercoupling. In this region, the measured quality factor approximates well to the intrinsic quality factor of the resonance mode and the transmission approaches to unity.

By decreasing the gap distance between the microresonator and the tapered fiber, we can move from the undercoupling regime to the critical coupling regime. At the critical coupling regime, the intrinsic decay rate and the external decay rates are equal, $\gamma_0 = \gamma_{ex}$ and therefore one can expect that the (2.16) at the zero detuning from the resonance frequency becomes $T(\Delta\omega = 0) = 0$. Additionally, the measured quality factor at the critical coupling is half of the value of the intrinsic quality factor of the microresonator, since $\frac{1}{Q_{total}} = \frac{1}{Q_{ex}} + \frac{1}{Q_0}$, and $Q_{total} = Q_0/2$.

Further decreasing the tapered fiber and microresonator gap distance moves the system into the overcoupling regime. At the over coupling regime, due to the further enhancement of the external decay rate, the total quality factor decreases and reaches its minimum at the zero gap. Moreover, the transmission at zero detuning increases but does not reach to 1. Figure 2-12. Presents different coupling regimes as well as the comparison of the intrinsic and coupling losses.

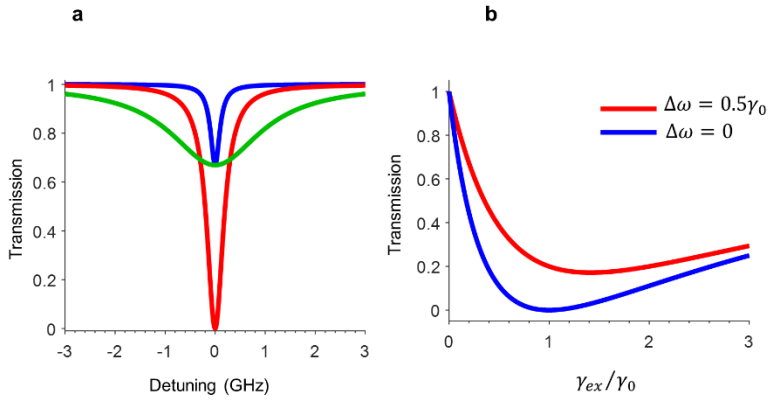

Figure 2-12: (a) Transmission spectra obtained at different coupling regimes, with blue, red, and green curves corresponding to the undercoupling ($\gamma_{ex} = \gamma_0/10$), critical coupling ($\gamma_{ex} = \gamma_0$), and overcoupling ($\gamma_{ex} = 10\gamma_0$) regimes. (b) Transmission at zero and non-zero detuning for different coupling regions. Zero transmission at $\gamma_{ex} = \gamma_0$ and zero detuning is clearly seen.

Chapter 3

Non-Hermitian Optical Systems

In this chapter, we briefly introduce and discuss non-Hermiticity in optical systems. Exceptional points (EPs) and the parity-time (PT) symmetry in photonics is discussed. Methods of creating EP and tuning the system to and from the vicinity of an EP are discussed. We note that although we discuss here optical systems, the concepts of non-Hermiticity, PT-symmetry and EPs are valid and observed in other physical systems such as acoustics, electronics, microwave, and thermal systems [14].

3.1 Introduction

Physical systems can be classified into two categories; Hermitian and non-Hermitian systems. While the Hermitian systems are well-isolated from other systems and their surroundings (thus are closed), non-Hermitian systems are open systems that are in continuous energy (i.e., in the form of loss or gain), information and material exchange with other systems or their environments.

Closed systems are described by Hermitian Hamiltonians and they are characterized by real eigenvalues, orthogonal eigenvectors, unitary evolution, and conserved probabilities. A Hermitian Hamiltonian satisfies,

$$H = H^{\dagger} = (H^{*})^{T} \quad (3.1)$$

where '†' denotes Hermitian conjugation, '*' is complex conjugation and 'T' is transposition. On the other hand, open systems are described by non-Hermitian Hamiltonians which have complex eigenvalues, exhibit non-unitary evolution and non-conserved probabilities. The imaginary part of the eigenvalues can either be associated to loss or the gain in a system. A striking difference between Hermitian and non-Hermitian system emerges in their respective spectral degeneracies. The spectral degeneracy, where two or more eigenvalues of a Hermitian system become equal to each other is referred to as a diabolic point (DP). Such spectral degeneracies for a non-Hermitian system are called as an exceptional point (EP). At a DP the corresponding eigenvectors are orthogonal to each other. However, at an EP the eigenvectors associated with the degenerate eigenvalues coalesce with each other (i.e., they are non-orthogonal) [48]. As such, a system's dynamics and its response to external perturbations of a system at an EP is significantly different than that of a system at a DP.

3.2 Parity-Time Symmetric Optical Systems

A class of non-Hermitian systems with gain and loss is referred to as parity-time (PT) symmetric systems, which is introduced by Carl Bender [21]. Interestingly, PT-symmetric systems exhibit either real eigenvalues (when the system is in the exact PT-phase) or complex conjugate eigenvalue pairs (when the system is in the broken PT-phase). The transition between the exact and the broken phase takes place at an EP, which is often referred to as a PT-phase transition.

Parity-time operator, $\hat{P}\hat{T}$ is combination of the parity operator $\hat{P}$ (or position operator) and the time reversal operator $\hat{T}$. The action of the $\hat{P}\hat{T}$ operator is described as

$$\hat{P}\hat{T}(x,t,i) \rightarrow (-x,-t,-i) \quad (3.2)$$

where x denotes the position in space, t is the time, and $i = \sqrt{-1}$. The parity operator exchanges the position of systems whereas the time reversal operator rewinds the time. A PT-symmetric Hamiltonian commutes with the $\hat{P}\hat{T}$ operator, that is $[\hat{H}, \hat{P}\hat{T}] = 0$ (i.e., $\hat{H}\hat{P}\hat{T} - \hat{P}\hat{T}\hat{H} = 0$).

Let us consider Schrodinger equation for a single particle,

$$i\hbar\frac{\partial}{\partial t}\psi(x,t) = \hat{H}\psi(x,t) \quad (3.5)$$

where $\psi(x,t)$ is describing the wave function, $\hbar$ is the reduced plank constant and the Hamiltonian is given by

$$\hat{H} = -\frac{\hbar^2}{2m}\frac{\partial^2}{\partial x^2} + V(x) \quad (3.6)$$

with $V(x)$ denoting the potential and m corresponding to the mass of the particle. For this Hamiltonian to be PT-symmetric, the complex potential $V(x)$ should satisfy

$$V_r(x) = V_r(-x) \text{ and } V_i(x) = -V_i(-x) \quad (3.7)$$

The paraxial equation of the electromagnetic wave propagation has the same form as the Schrodinger equation [2]

$$i\frac{dE(x,z)}{dz} + \frac{1}{2k}\frac{d^2E(x,z)}{dx^2} + k_0\big(N(x) + iK(x)\big)E(x,z) = 0 \quad (3.3)$$

where the $E(x,z)$ is the electric field, and $n(x) = N(x) + iK(x)$ is the complex refractive index distribution over the x-axis, with $N(x)$ and $K(x)$ corresponding to its real and imaginary parts, respectively, $k_0$is the free space wavevector, and $k = n_0k_0$. Enforcing PT-symmetry on this system by applying the $\hat{P}\hat{T}$ operator, we find that $n(x)$ should satisfy

$$N(x) = N(-x), \qquad K(x) = -K(-x) \quad (3.4)$$

In other words, for an optical system to be PT-symmetric, the real part of the refractive index distribution must be an even function while its imaginary part must be an odd function. Since

a positive $K(x)$ is associated with loss and the negative $K(x)$ is associated with gain, PT-symmetric optical systems can be created by asymmetric gain and loss distribution [2].

A generic Hamiltonian for a non-Hermitian system composed of two sub-systems with complex frequencies $\omega_1 - i\gamma_1$ and $\omega_2 - i\gamma_2$ that are coupled to each other by strength k is given by:

$$H = \begin{bmatrix} \omega_1 - i\gamma_1 & k \\ k & \omega_2 - i\gamma_2 \end{bmatrix} \quad (3.8)$$

The eigenvalues of this Hamiltonian are

$$\omega_{\mp} = \omega_0 - i\chi \mp \sqrt{k^2 + \Gamma^2} \quad (3.9)$$

where $\chi = \frac{\gamma_1+\gamma_2}{2}$, $\omega_0 = \frac{\omega_1+\omega_2}{2}$ and $\Gamma = \frac{\omega_1-\omega_2}{2} + \frac{i(\gamma_1-\gamma_2)}{2}$. Clearly, the eigenvalues become degenerate, that is $\omega_+ = \omega_- = \omega_0 - i\chi$, and an EP emerges when $k^2 + \Gamma^2 = 0$. For this Hamiltonian to represent a PT-symmetric system, the eigenvalues should be real or complex conjugate of each other. To have real eigenvalues, one should set $\chi = 0$, that is $\gamma_1 + \gamma_2 = 0$. This then imposes $\gamma_1 = -\gamma_2 = \gamma$, implying that if the first sub-system is lossy with $\gamma_1 > 0$, the second sub-system should have gain (i.e., positive γ_1 denotes loss while negative γ_1 denotes gain) that compensates the loss γ_1. However, this is not sufficient to have real eigenvalues. We should also make sure that $k^2 + \Gamma^2 \geq 0$, which implies $\omega_1 = \omega_2 = \omega_0$ and $k^2 - \gamma^2 \geq 0$. As a result, the generic PT-symmetric Hamiltonian can be written as,

$$H = \begin{bmatrix} \omega_0 - i\gamma & k \\ k & \omega_0 + i\gamma \end{bmatrix} \quad (3.10)$$

With the eigenvalues given as $\omega_{\mp} = \omega_0 \mp \sqrt{k^2 - \gamma^2}$. Clearly, the eigenvalues are real for $k^2 > \gamma^2$ (exact PT-phase); imaginary for $k^2 < \gamma^2$ (broken PT-phase); and degenerate at $\omega_{\mp} = \omega_0$

(EP). Thus, by tuning the coupling strength and the loss-gain parameter, one can move the system from exact to broken PT phase through an EP. One should note that in a PT-symmetric system in the exact phase, the system has real eigenvalues (i.e., energies) but power is not conserved.

Non-Hermiticity, including PT-symmetry, in photonics have led to several counterintuitive and outstanding applications such as loss induced transparency and lasing [18-20], unidirectional clocking and reflection, enhanced sensing [30-31].

Figure 3-1 presents the variation of the real and imaginary parts of the eigenfrequencies as a function of coupling strength. Figure 3-1(a) presents the bifurcation of the eigenfrequencies of a generic Hamiltonian as a function of coupling strength, while the loss imbalance is fixed. In Figure 3-1(b) the bifurcations of the eigenvalues for the PT-symmetric Hamiltonian are presented as a function of coupling strength while gain and loss values are fixed. Additionally, the transition from Broken-PT to the PT-Phase through the EP is illustrated.

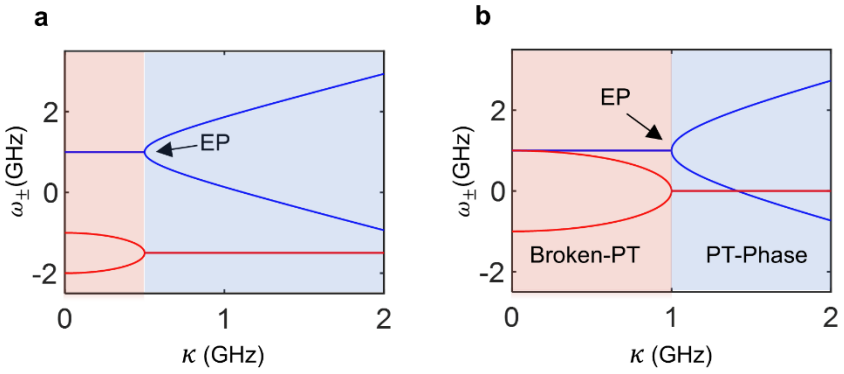

Figure 3-1: (a) Variation of eigenfrequencies of the generic Hamiltonian as a function of coupling strength while the loss imbalance is fixed, (b) Variation of eigenfrequencies of the PT-symmetric Hamiltonian as a function of coupling strength while the gain and loss values are fixed.

3.3 Exceptional Points

Exceptional points are the spectral degeneracies of non-Hermitian systems, including PT-symmetric systems. In a PT-symmetric systems exceptional points (EPs) emerge in the transition from the exact PT-phase to the broken PT-phase regimes. EPs in optical systems can be created in different ways. For example, in PT-symmetric systems, an EP emerges when the coupling strength k or the balanced gain-loss γ is tuned such that $k^2 = \gamma^2$. In the case of coupled resonators (or coupled waveguides), the coupling strength can be tuned by varying the distance between the resonators (or the waveguides) [78]. In loss-only coupled systems with zero-detuning, EP emerges when the coupling strength is tuned to become equal to the loss-difference between the systems, or at fixed coupling strength the loss-imbalance is varied. In the case of coupled waveguides (or coupled resonators), the loss of one of the waveguides (or one of the resonators) can be varied by introducing a lossy element into its mode volume [18]. EPs have been shown to occur in a single WGM microresonator by coupling the clockwise (CW) and counter-clockwise (CCW) modes of the resonator. In the experiments, the coupling between CW and CCW modes has been achieved by introducing a Rayleigh scatterer into the mode volume of the resonator. This symmetric coupling induces mode splitting. Then a second scatterer is introduced into the mode volume of the resonator and its position is varied until the mode splitting vanishes, which assures the emergence of an EP [4]. The second scatterer breaks the symmetric coupling and establishes asymmetric coupling between CW and CCW modes.

As mentioned before, at an EP not only the eigenfrequencies but also the associated eigenvectors coalesce with each other. This implies that the system loses its dimensionality at an EP. As a result, the system becomes sensitive to perturbations. This can be easily understood from Fig. 3-2 which presents the eigenfrequencies of a Hermitian and a non-Hermitian system when two of the system parameters are varied. It is clearly seen that the eigenenergy space of a Hermitian system exhibits two cones whose apex coincide at the diabolic point (DP). When the system is at

the DP, a perturbation will shift the eigenfrequencies along the cones. As a result, the eigenfrequencies bifurcate linearly with increasing perturbation strength. A plot of the eigenfrequencies of a non-Hermitian system exhibits two Riemann sheets with an EP at their intersection. When the system is perturbed when it is at the EP, the eigenfrequencies will not bifurcate linearly but instead exhibit a bifurcation which is proportional to the square root of the perturbation strength. Thus, a system operating at an EP will exhibit a larger response than that operating at a DP for the same perturbation strength. The response becomes larger if the EP is formed by the coalescence of more than two eigenfrequencies. For an N-fold EP (i.e., the number of coalescing eigenvalues and eigenvectors is N), the eigenfrequency bifurcation or splitting scales as ϵ^(1/N) for a perturbation of ϵ while splitting for the system at DP is just ϵ. Therefore, for small perturbations a system at EP exhibits much larger response.

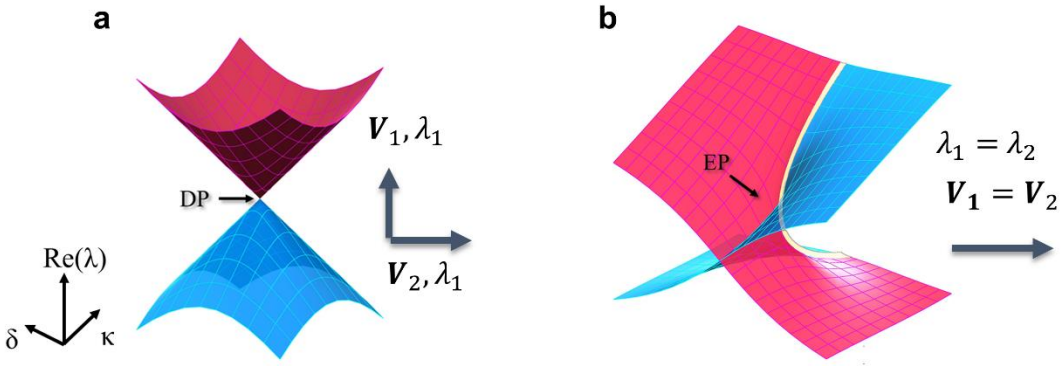

Figure 3-2: (a) Diabolic point in a Hermitian system (closed system), (b) Exceptional Point in a non-Hermitian system (open system).

Chapter 4

Exceptional Surfaces and Optical Realization

4.1 Introduction

Exceptional points (EPs) are isolated spectral degeneracies in the parameter space of a non-Hermitian system. As discussed earlier, they are very sensitive to perturbations. This feature has been exploited for enhancing the response of sensors [30]. However, this feature also restricts the application domain of EPs, because this sensitivity to small perturbations makes it difficult, if not impossible, to operate a system exactly at an EP or in the very close vicinity of an EP due to instabilities. For example, any small imperfection in the fabrication of the resonators or fluctuations in the coupling conditions in a waveguide-coupled resonator system will move the system away from the EP. Additionally, in the single resonator system where two nanoscatterers or nanotips are used to bring the system at an EP [10], any fluctuations, vibrations, or instabilities in the positions of the scatterers or tips will move the system away from its EP. Therefore, there is a need for techniques or methods that ensures a physical system always operate at an EP despite the presence of instabilities and imperfections discussed above. Exceptional surfaces (Ess) are proposed to address this challenge [30]. An ES is a hypersurface in the parameter space of a physical system where every point on the surface is an EP. Figure 4-1 shows a comparison of an EP and ES. In the following we will discuss how ESs can be implemented in waveguide-coupled resonator systems.

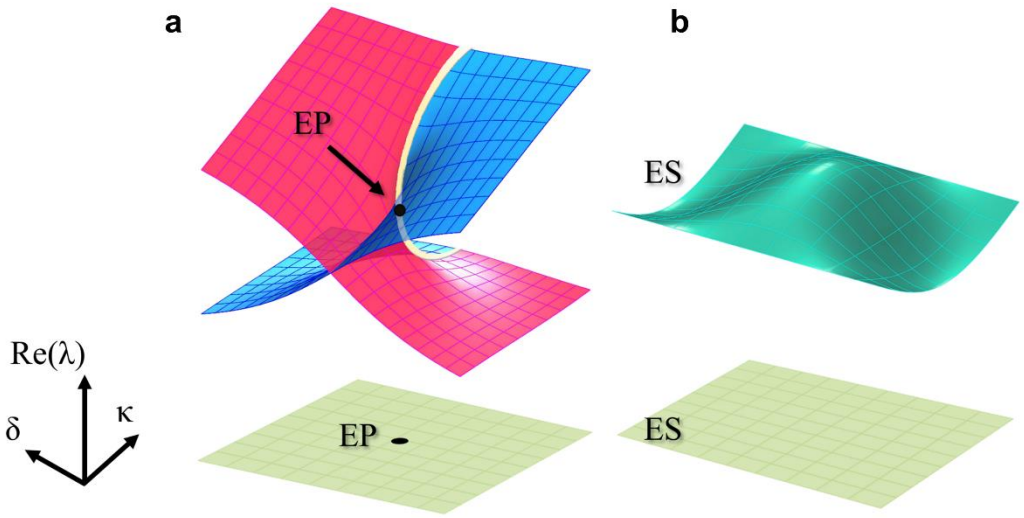

Figure 4-1: Illustration of an (a) exceptional point (EP), and an (b) exceptional Surface (ES).

4.2 Exceptional Surface in a waveguide-coupled resonator system

As we discussed in the previous chapter, asymmetric coupling between the CW and CCW modes of a WGM resonator leads to the emergence of an EP. In 2019, Zhong *et al* have shown that an ES emerges if the coupling between the CW and CCW modes are made nonreciprocal or unidirectional, in the sense that one of the modes, say CW, couples to the other mode, say CCW, but the CCW mode does not couple to the CW mode [30]. It was also proposed that such a setting can be achieved if one end of the waveguide is terminated with a symmetric partially reflecting mirror (Fig. 4-2).

Let us consider the system in Fig. 4-2 and derive the mathematical expressions describing this system. Denoting the intracavity field amplitudes in the CW and CCW directions as $a_{cw}$and a_{ccw}, respectively, we can write the set of coupled mode equations as [30]

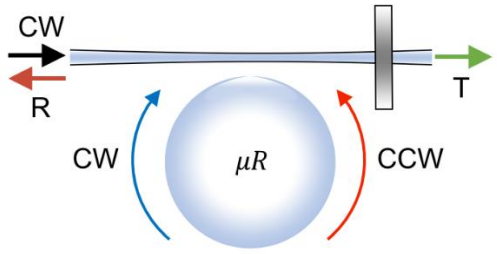

Figure 4-2: Terminating only one end of the waveguide by a partially reflecting mirror establishes unidirectional coupling between CW and CCW modes, leading to emergence of ES. Here, light input in the CW mode direction couples to CCW but the light input in the CCW mode direction does not couple to the CW mode. T and R denote the transmission and reflection.

$$i\frac{d}{dt}\begin{bmatrix} a_{cw} \\ a_{ccw} \end{bmatrix} = H_{ES}\begin{bmatrix} a_{cw} \\ a_{ccw} \end{bmatrix} \quad (4.1)$$

where the system Hamiltonian is given by

$$H_{ES} = \begin{bmatrix} \omega_0 - i\gamma & 0 \\ \alpha\mu^2 & \omega_0 - i\gamma \end{bmatrix} \quad (4.2)$$

with ω_0, γ, and μ denoting the resonance frequency, losses of the CW and CCW modes, and the coupling strength between the waveguide and the resonator, respectively, and $\alpha = r_m exp\,(i2\Phi)$ with r_m representing the reflectivity of the end-mirror. The off-diagonal element of H_{ES} with value zero implies that CCW mode does not couple to the CW mode, and the non-zero off-diagonal element represents the strength of the coupling from CW to CCW. This asymmetric coupling is the source of non-Hermiticity in this system.

The eigenvalues $\omega_{1,2}$ and the associated eigenvectors $\tilde{a}_{1,2}$ of H_{ES} are given by

$$\omega_{1,2} = \omega_0 - i\gamma, \qquad \tilde{a}_{1,2} = (0,1)^T \quad (4.3)$$

which shows that both the eigenvalues and the associated eigenvectors coalesce with each other. It is clearly seen that as long as the unidirectionality of the coupling is maintained (i.e., one of the off-diagonal elements remains zero), the system is always at an EP. Thus, the system will always have degenerate eigenvalues and eigenvectors, even if μ and/or α fluctuate or are perturbed. Thus,

varying any two of the parameters μ, r_m, and Φ will form a hypersurface in the parameter space where all the points on the hypersurface is an EP. Thus, this hypersurface is an ES.

Any perturbation that destroys he unidirectionality of the coupling between the CW and CCW modes will lift the system off the ES leading to frequency splitting. Such a perturbation could be induced by a Rayleigh scatterer which leads to symmetric scattering of CW to CCW and CCW to CW, thus leading to non-zero off-diagonal elements. Assuming a perturbation of strength ε, the splitting scales as $\Delta\omega \approx \sqrt{\varepsilon}$. If the system is operated far from an EP (i.e., for example by setting a symmetric coupling or by removing the end mirror), the frequency splitting will be $\Delta\omega \approx \varepsilon$. If the $\phi = \varphi_1 + \varphi_2$, where φ_1 and φ_2 are the phase gained in the $L_1$and L_2, respectively, is utilized to parameterize the input frequency, the frequency splitting could be described as $\Delta\phi = \sqrt{r_p^2 + r_m' k^2 r_p}$, where r_p, and $r_m' k^2$ represent the particle reflectivity and the effective unidirectional coupling from CW to CCW, which reveals [30]

$$\Delta\phi_{EP} \approx \begin{cases} 2k\sqrt{r_p}\,, & r_p \ll k^2 \\ 2r_p\,, & r_p \gg k^2 \end{cases} \quad (4.5)$$

$$\Delta\phi_{DP} = 2r_p \quad (4.6)$$

Frequency splitting in the case of particles with smaller perturbations ($r_p \ll k^2$) scales with the $\sqrt{r_p}$, while increasing the perturbation value shifts the system away from the EP and the response of the system to the perturbations becomes linear, similar to a system operated at a DP (e.g., by removing the end mirror).

4.3 Experimental demonstration of exceptional surfaces

We have implemented the optical system shown in Fig. 4-2 using a tapered fiber coupled WGM on-chip microsphere (Fig. 4-3) and a feedback loop which simulates the end-mirror. In this system, light input to the resonator in the CW direction is transmitted in the forward direction and

then couples back to the resonator in the CCW direction via the feedback loop (end-mirror) However, when the light is input to the resonator in the CCW direction, it will be transmitted in the backward direction and there will be no coupling back to the CW direction (i.e., no end-mirror at the output of the fiber in the CCW input direction). This generates an asymmetric or unidirectional coupling between CW and CCW modes and assures that the system is operating on the ES. We control the amount of feedback using a variable optical attenuator placed in the feedback loop (i.e., this is similar to changing the reflectivity of the end-mirror).

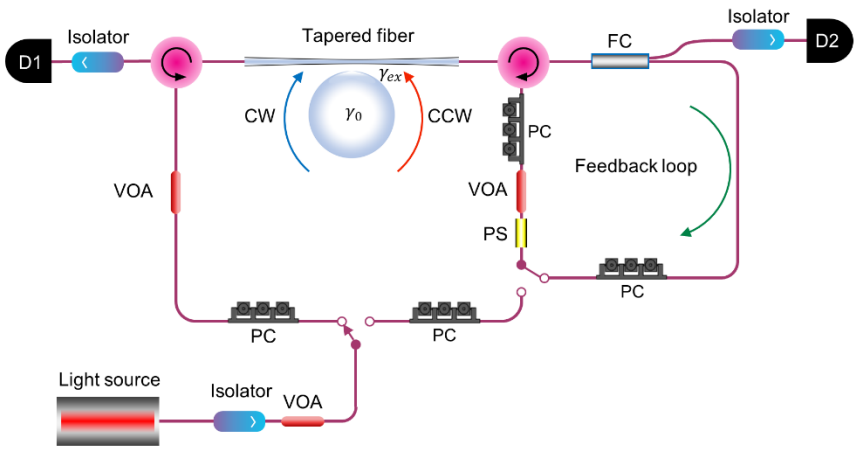

Figure 4-3: Schematic of the exceptional surface setup with feedback loop, which implements a tunable end-mirror with adjustable phase and reflectivity. D1 and D2 are photodetectors, light source is a tunable external cavity laser, FC: fiber coupler, VOA: variable optical attenuator, PS: phase shifter, PC: polarization controller.

In our experiments, we first made sure that 1) there is no intrinsic frequency splitting in the system, 2) the resonator has a high-Q mode, and 3) the system is symmetric for the inputs in the CW and CCW directions without the feedback loop. As seen in Fig. 4-4, the transmission spectrum exhibits a resonance dip in the photodetector PD1 and zero reflection signal at PD2 when the light is input in the CCW direction. For an input in the CW direction, the transmission spectrum at PD2 exhibits a transmission dip and the reflection detected at PD1 has zero signal when the light is input

in the CW direction. This confirms that there is no initial coupling between the CW and CCW modes. Figure 4-4 also confirms that the resonance frequencies, measured Q-factors, and the loading curves are the same for CW and CCW inputs (i.e., a symmetric system).. After confirming that the system is symmetric without the feedback loop, we connected the feedback loop and input the light in the CW direction. This couples the CW to CCW mode but not the other way around. By tuning the attenuation in the feedback loop, we controlled the feedback strength. Additionally, using the phase shifter in the feedback loop we controlled the phase of the reflection and studied its impact on the reflection spectrum.

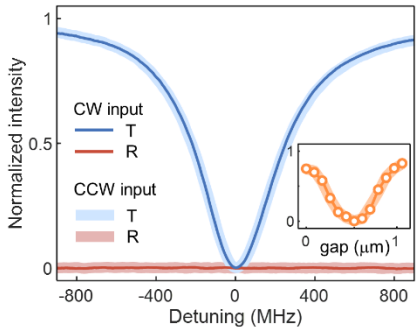

Figure 4-4: Transmission and reflection spectra in the absence of the feedback loop for input lights in the CW and CCW directions, Both CW and CCW inputs exhibit resonance dip in their transmission spectra and no signal in their reflection spectra. The resonance takes place at $\lambda_0 = 1506\,nm$ with $Q = 1.4 \times 10^6$. Inset demonstrates the loading curves for both CW and CCW inputs.

When we operate the system in the critical coupling with maximum feedback (i.e., maximal coupling from the CW mode to the CCW mode at the critical coupling), we observed a resonance dip in the reflection spectra detected at photodiode D1. In contrast to all previous experiments performed with systems exhibiting EPs, here we saw that the reflection spectrum exhibits a quartic lineshape (squared Lorentzian) rather than a quadratic lineshape (Lorentzian). Although this was expected in theoretical studies, it has not been demonstrated in the experiments until this work. Since our system is operating stably on the exceptional surface, it is always exactly at an EP. Thus,

it does not suffer from noises induced by fluctuations and instabilities and it always operate at an EP. As a result, we could observe this quartic reflection spectrum, a spectra with flat bottom (Fig. 4-5). Next, we collected a large number of reflection spectra by varying the phase and strength of feedback at different coupling conditions. We performed curve fitting to each of the collected spectra using the product $L_1.L_2$ of two Lorentzian functions L_1 and L_2. In the curve fitting process, the resonance frequencies and linewidths of the Lorentzian are used as free parameters which are adjusted for the best fitting. From the estimated data, we calculated the Δw (difference of resonance frequencies of two Lorentzian) and $\Delta\gamma$ (difference of linewidths of the Lorentzians) and plotted them as a function of the feedback phase and magnitude at each coupling condition. For ideal curve fitting and perfect noiseless experimental conditions, Δw and $\Delta\gamma$ should be zero implying that the system is on a surface in the space spanned by two system parameters, which are feedback magnitude and phase here.

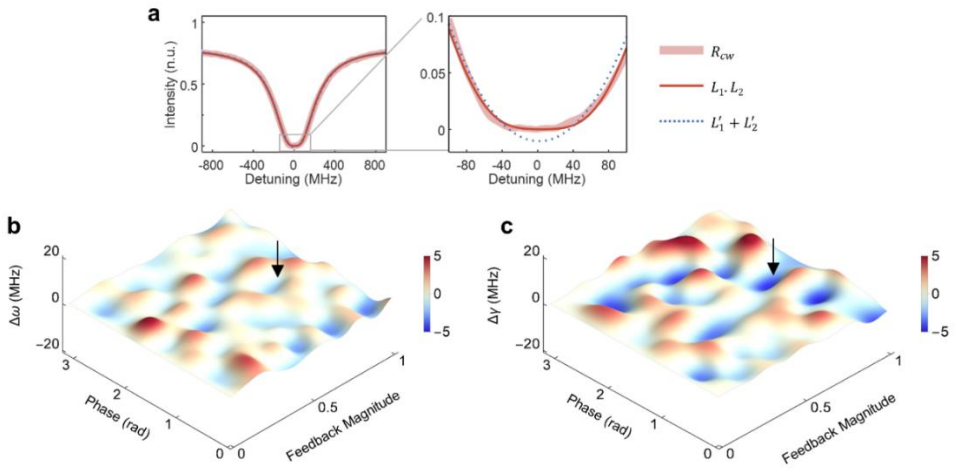

Figure 4-5: (a) Reflection spectra exhibit quartic (squared Lorentzian) lineshape for the input in the CW direction. Curve fittings were performed using product and sum of two Lorentzians. Best fitting was obtained for the product of two Lorentzians. (b), (c) Curve fitting data to the reflection spectra at various feedback magnitude and phase reveals an exceptional surface.

As seen in Fig. 4-5, Δw and $\Delta\gamma$ fluctuates within a very small band compared to the resonance frequency and linewidth of the initial mode at the critical coupling, and thus our system is on an ES and always operates at an EP. The small variations in Δw and $\Delta\gamma$ may be attributed to the numerical curve fitting noise and electrical noise etc present in the system.

4.4 Numerical Simulation of the system

Asymmetry in reflection. We confirmed our experimental results through simulations in COMSOL Multiphysics and Lumerical. Simulations revealed that for any non-zero feedback strength (i.e., non-zero end-mirror reflectivity; non-zero coupling from CW to CCW and zero coupling from CCW to CW), the system is always on an ES, leading to reflection spectra with squared Lorentzian lineshape. Figure 4-6 presents the transmission and reflection spectra of the system obtained in COMSOL simulations for CW and CCW inputs for an end-mirror with 50% reflection and 50% transmission.

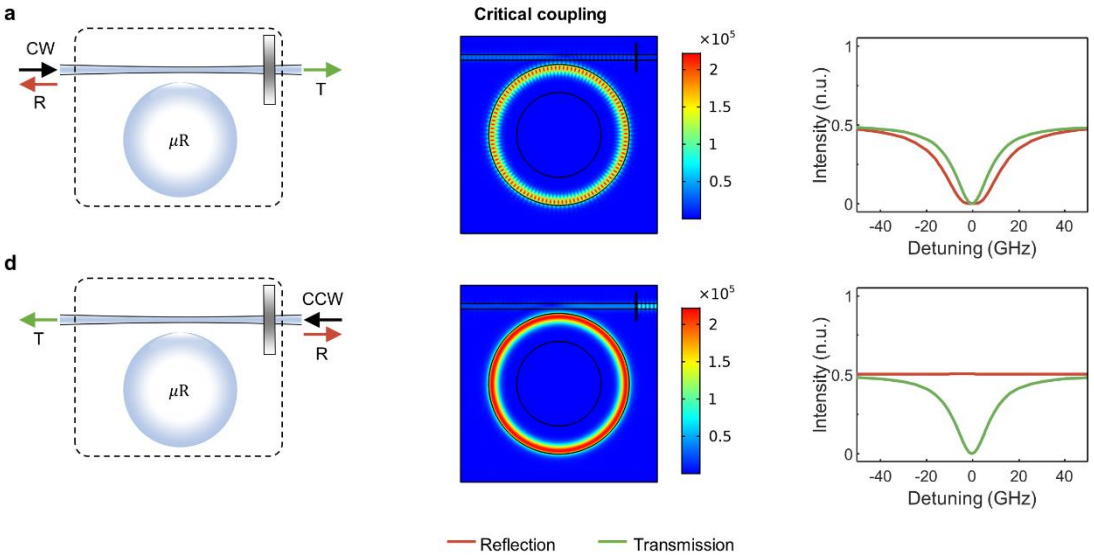

Figure 4-6: Reflection and transmission spectra obtained in COMSOL simulations for inputs in the (a) CW and (b) CCW directions when the end-mirror is half-reflecting and the system is at critical coupling.

The following are clearly seen: 1) Transmission is symmetric, that is the transmission exhibits Lorentzian resonance dips for both CW and CCW inputs. 2) Reflection is asymmetric, that is for the CW input the reflection spectrum exhibits squared Lorentzian resonance dip but for the CCW input reflection does not exhibit resonance. 3) For the CW input the field inside the cavity exhibits a standing wave pattern due to interference of the CW and CCW modes present in the cavity whereas for the CCW input field inside the cavity is a travelling wave because there is only CCW mode in the cavity.

Effect of a scatterer in the mode volume. We simulated the effect of a scatterer located in the mode volume of the system using Lumerical Interconnect. As we discussed above, such a scatterer will induce bidirectional coupling between the CCW and CW modes and hence will modify the system Hamiltonian such that both off-diagonal elements are non-zero. This should then move the system from the ES, leading to mode splitting. Such a situation can take place in sensing applications.

As seen in Fig. 4-7, when there is no scatterer ($R_{scatterer} = 0$), the system with a half reflecting symmetric mirror exhibits Lorentzian resonance dip in the transmission and squared-Lorentzian resonance dip in the reflection for the CW input. An infinitesimally small increase in $R_{scatterer}$ modifies both the reflection and transmission spectra: Reflection spectrum is no longer with a squared Lorentzian lineshape but it exhibits mode splitting. As we increase $R_{scatterer}$, frequency splitting increases, too. Similarly, reflection at zero-detuning increases with increasing $R_{scatterer}$. These features can be used for particle sensing. More interestingly, we observe that frequency splitting is first seen clearly in the reflection spectra while it is not seen in the transmission spectra although one can see modification of the transmission spectra. This implies that the reflection spectrum is more sensitive to perturbations induced by nanoparticles than the transmission spectrum.

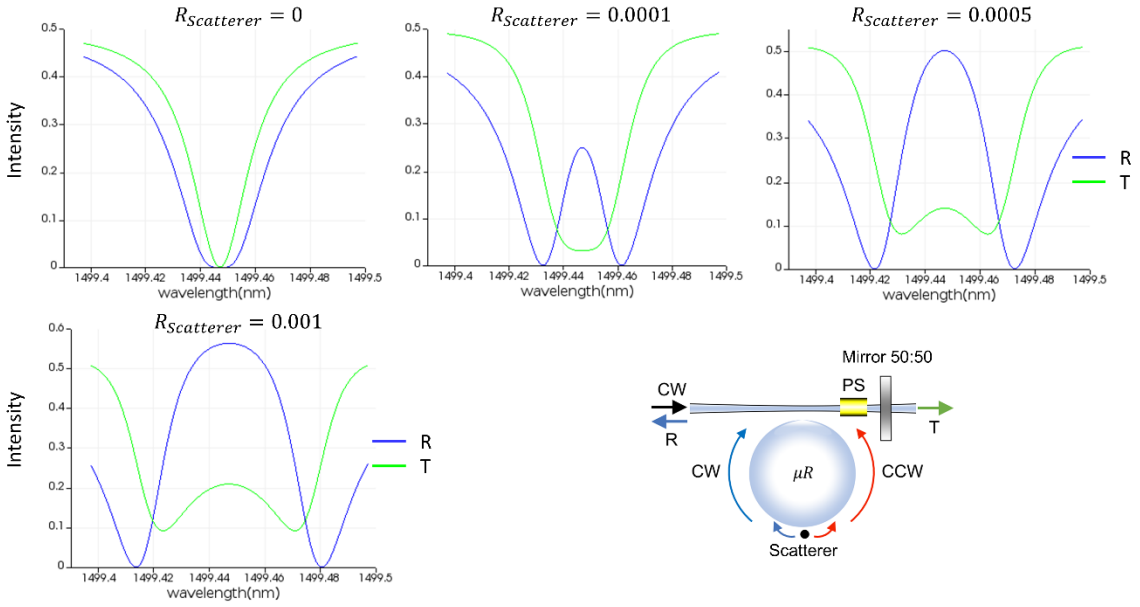

Figure 4-7: Effect of a scatterer in the transmission and reflection spectra of a waveguide-coupled resonator operating on an ES at the critical coupling.

In Fig. 4-8, we show the eigenfrequency splitting and resonance peak observed in the transmission and reflection spectra as a function of the reflectivity (i.e., $R_{scatterer}$) of a nanoparticle placed within the mode volume. The eigenfrequency splitting observed in the reflection spectra (red curve) is always greater than the splitting observed in the transmission spectra (blue curve), implying the high sensitivity of reflection spectra on ES to small perturbations. In the cases where frequency splitting is not observable, one can alternatively monitor the changes in the resonance reflection and transmission. As seen in Fig. 4-8 (a), intensity at the resonance shows a significantly higher change in reflection spectra than the transmission spectra.

In sensing applications based on frequency splitting, an important question is how the system can be brought back to its initial condition, that is to the EP or the ES. This was a challenge in previous EP-based sensors. For example, in the nanoparticle sensing application, the positions of the nanotips were tuned to bring the system back to EP after the splitting. This is certainly not a practical method. This challenge can be easily addressed in our system, that is a resonator operating

on an ES. When the reflection or transmission undergoes frequency splitting due to a scatterer, one can tune the phase of the feedback or the end-mirror reflection (or by tuning an electrically controlled phase shifter) to bring the system back to its pre-scatterer condition, that is back to the ES. Lumerical simulation results shown in Figs. 4-9 and 4-10 show that by controlling the phase of the mirror reflectivity, one can control transmission and reflection spectra. Figure 4-9 is obtained for a scatterer $R_{scatterer} = 0.0001$. It is clear that with the proper setting of this phase, the frequency splitting is removed, and the reflection spectrum returns back to a squared Lorentzian lineshape and the transmission back to its initial form. Although it is not clear, we suspect that the effect of phase on the spectra in the presence of a particle may be used to estimate particle size or polarizability. In Fig. 4-10 the effect of changing reflection phase on the transmission and reflection spectra is presented for $R_{Scatterer} = 0.01$. By increasing the phase to $PS = 3.14\ rad$ the reflection spectra present smaller eigenfrequency splitting in comparison to the transmission spectra. We think that measuring reflection and transmission spectra at different phase values may be used to estimate the polarizability or the size of a particle. This is left as a topic of further study.

We also investigated the effect of the magnitude of the end-mirror reflectivity on the transmission and reflection spectra in the presence of a scatterer $R_{scatterer} = 0.0001$ (Figure 4-11). When the end-mirror reflectivity is 0 (i.e., no end-mirror), the reflection spectrum exhibits a Lorentzian peak for a CW input while the transmission exhibits a Lorentzian dip. The Lorentzian peak in the reflection is due to the presence of the scatterer which couples the CW input field to the CCW direction. As soon as the end-mirror reflectivity becomes non-zero, we observe splitting in the reflection spectra while the transmission spectra does not exhibit splitting although it is modified. Reflection at zero-detuning increases with increasing end-mirror reflectivity until reflectivity is 50%. For reflectivity values in the range 50-100 %, the reflection value at zero-detuning decreases with increasing reflectivity but never becomes zero.

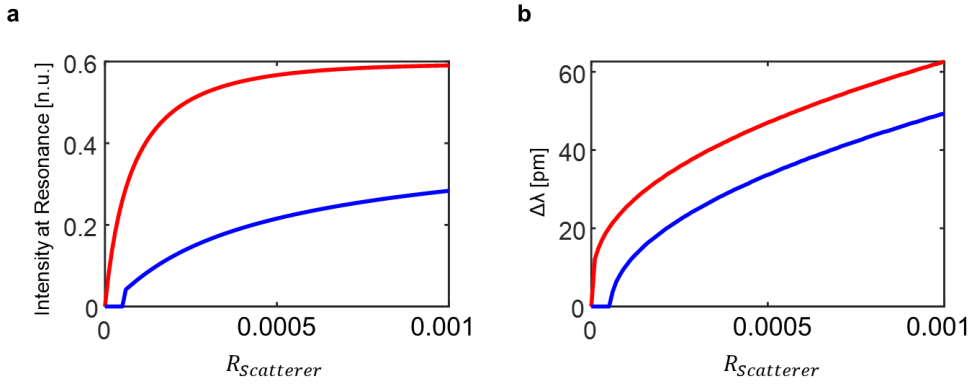

Figure 4-8: Effect of a scatterer in the transmission and reflection spectra of a waveguide-coupled resonator operating on an ES at the critical coupling. (a) Peak intensity of the reflection at the resonance (red curve) and peak intensity of the transmission at resonance (blue curve) versus $R_{scatterer}$. (b) Eigenfrequency splitting of the reflection spectra (red curve), and eigenfrequency splitting of the transmission spectra (blue curve).

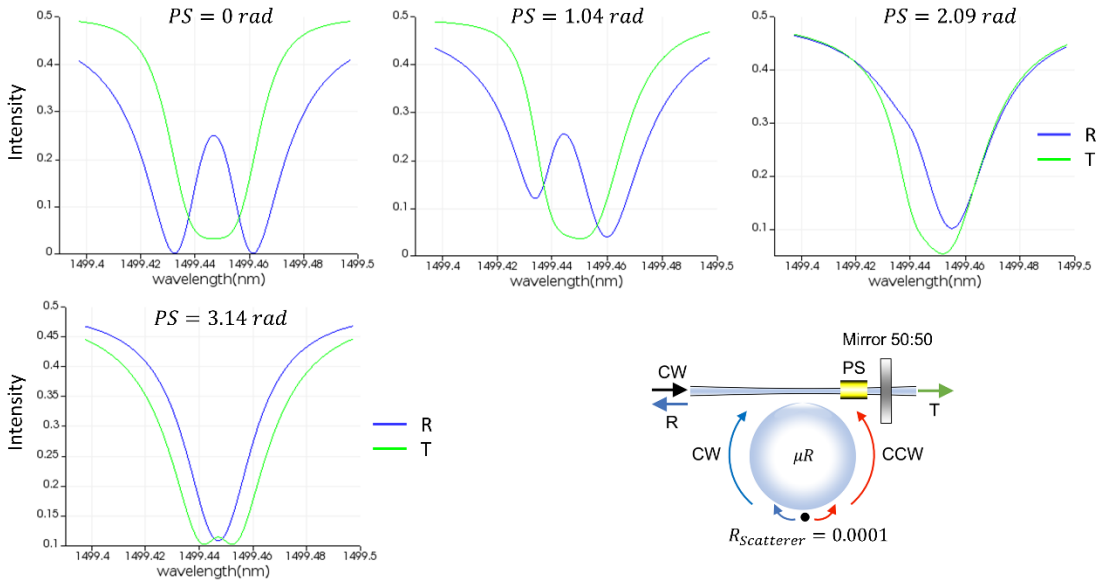

Figure 4-9: Effect of the phase of the reflectivity of the mirror on the transmission and reflection spectra in the presence of a scatterer ($R_{Scatterer} = 0.0001$) when the system was initially on the ES at the critical coupling. Clearly, scatterer leads to splitting in the reflection and modifies transmission and reflection spectra, eliminating the splitting.

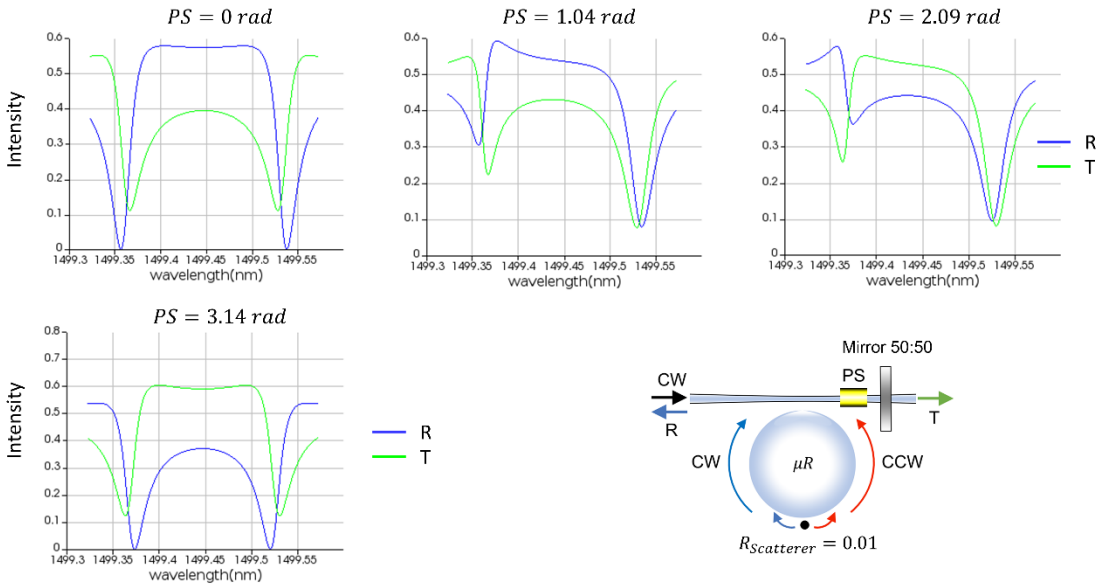

Figure 4-10:Same as Fig. 4-9, but $R_{Scatterer} = 0.01$.

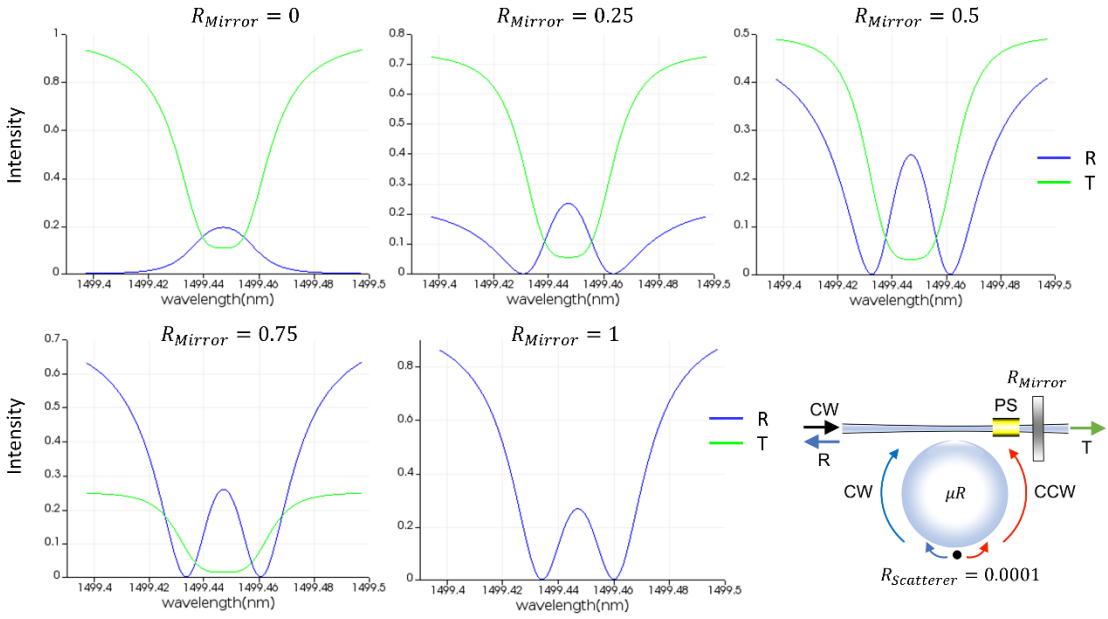

Figure 4-11: Effect of the end-mirror reflectivity on the reflection and transmission spectra at critical coupling in the presence of a scatterer $R_{scatterer} = 0.0001$.

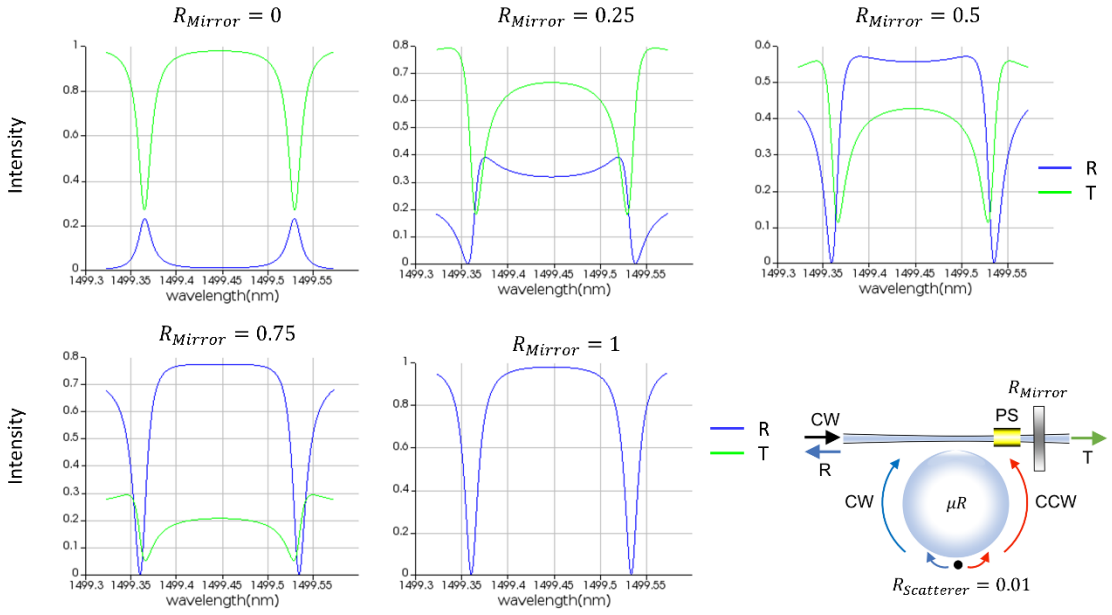

Figure 4-12: Same as Fig. 4-11, but $R_{Scatterer} = 0.01$.

Effect of placing an end-mirror in the CCW direction. We placed mirrors to each end of the fiber (i.e., end mirrors in both the CW and CCW directions). While only one end-mirror allows unidirectional coupling between CW and CCW modes, two end-mirrors will allow a tunable bi-directional coupling between the modes. Note that the system is on the ES only when the coupling between CW and CCW modes is unidirectional. Such a case can take place if there is back-scattering at the waveguide ends due to fabrication imperfections etc. In the simulation results shown in Fig. 4-13, we set the reflectivity of the end-mirror in the CW direction as 50% (i.e., $R_1 = 0.5$) and varied the reflectivity of the end-mirror in the CCW direction (i.e., R_2). Similar to the case of a scatterer, we observe splitting in the reflection spectra for non-zero R_2. As seen in Fig. 4-14 and Fig. 4-15 when the phase of the light reflected from the first end-mirror is varied, the system moves back to its initial condition as if the second mirror was not present (i.e., squared Lorentzian reflection spectra and Lorentzian transmission).

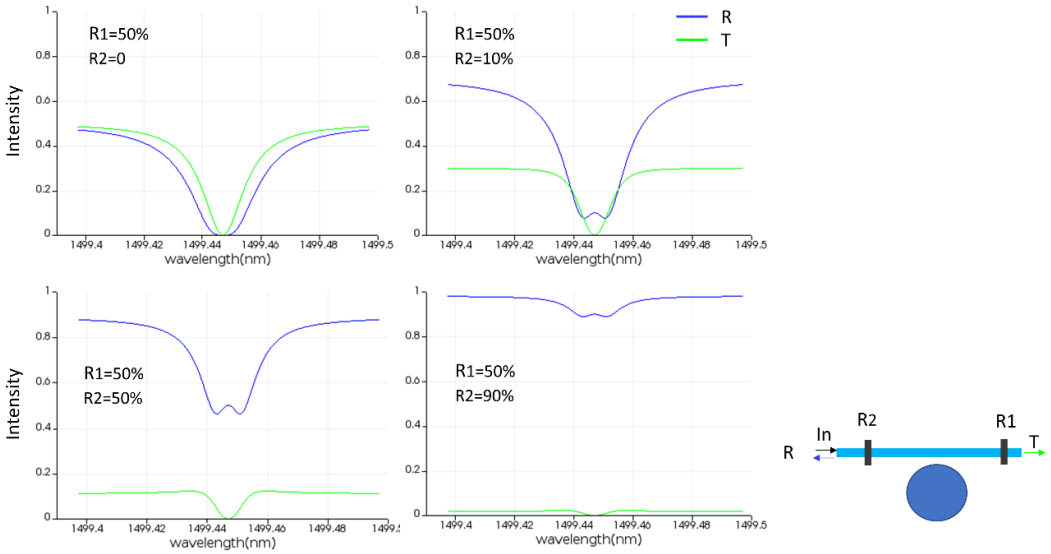

Figure 4-13: End-mirrors at both ends of the waveguide when the system is at critical coupling destroys unidirectional coupling between CW and CCW modes and leads to bidirectional asymmetric coupling between them which results in frequency splitting in the reflection spectra.

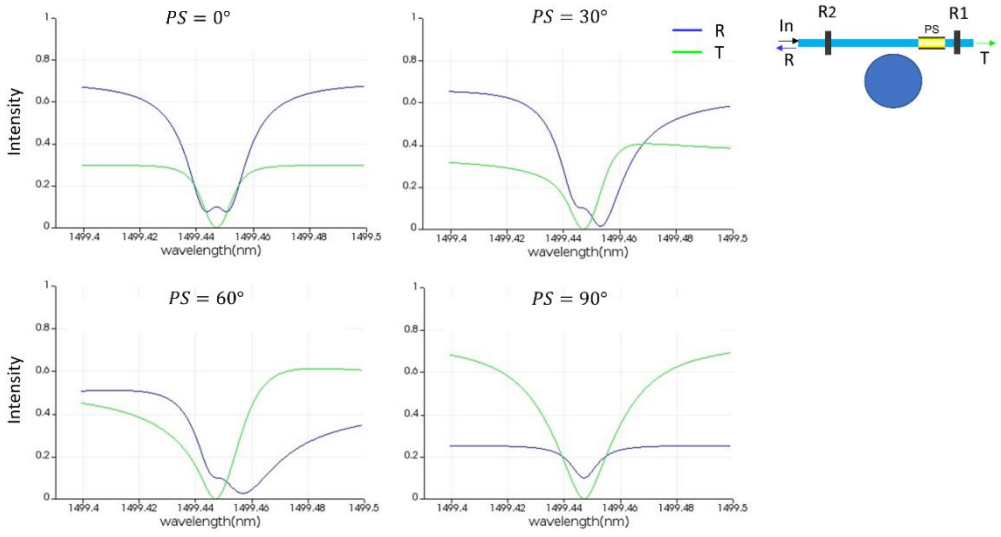

Figure 4-14: Effect of the phase of the reflected light from one of the end-mirror can help to control the lineshape of the reflection spectra. By properly setting the phase, reflection transits from splitting to no-splitting spectra. $R_1 = 50\%$ and $R_2 = 10\%$ is used in the simulations.

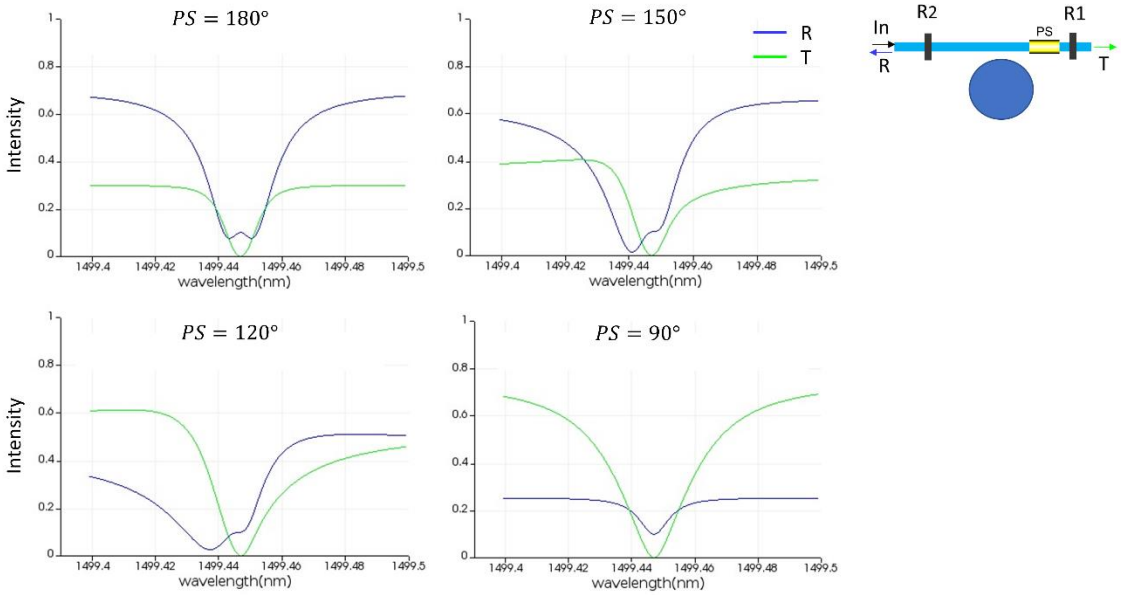

Figure 4-15: Same as Fig. 4-14.

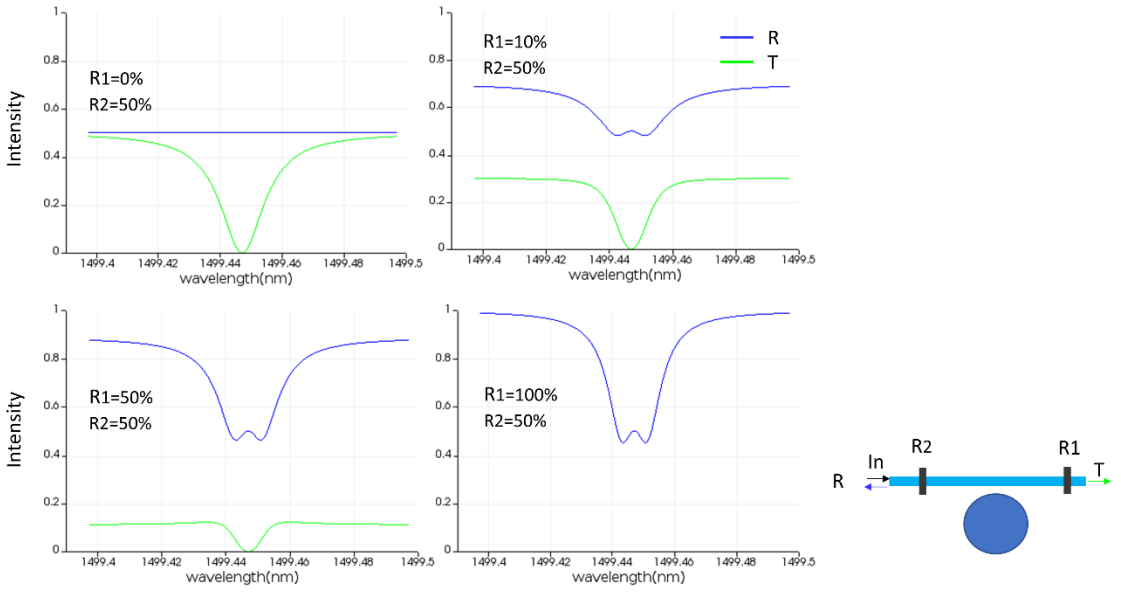

Figure 4-16: Same as Fig. 4-14 but R_1 is varied while R_2 is kept constant.

The effect of the phase is clearly seen in Fig. 4-14. This figure together with Fig. 4-9 clearly shows the important role of phases and interferences in the form of the transmission and reflection spectra. As seen in Figs. 4-16 the trend is the same if R_2 is kept fixed and R_1 is varied.

4.5 Conclusion

In conclusion, we have for the first time experimentally demonstrated an exceptional surface via chiral (i.e., uni-directional) coupling between the CW and CCW modes of a WGM microresonator. We observed quartic reflection spectra which is the hallmark of a system operating on an ES or at an EP. With numerical simulations performed in COMSOL and Lumerical, we investigated the effect of perturbations, such as a scatterer or reflections from the end facets of the waveguide, that can change the coupling from a chiral coupling to a bi-directional coupling. Such asymmetric bidirectional coupling between CW and CCW modes leads to frequency splitting in the reflection spectra, implying that we can use Ess for particle sensing, and that reflection spectra is more sensitive to perturbations than the transmission spectra. Our numerical simulations also clearly demonstrate the importance of phase relations and interferences in determining the lineshape of reflection spectra.

Chapter 5

Chiral and Degenerate Perfect Absorption on the Exceptional Surfaces

(This chapter is under review in a peer-reviewed journal. It can be found in the arXiv: https://arxiv.org/abs/2107.06019)

Designing a surface of exceptional points (EPs), (i.e., exceptional surfaces (ES)) can enable many interesting features and functionalities, which could be utilized for designing new applications and devices. One of such features is the chiral behavior at an EP, and therefore on the ES. The chirality in photonics, can provide opportunities in sensing, quantum electrodynamics, thermal imaging, as well as radiation control. As we discussed in previous sections, it has been very difficult to tune a system to the vicinity of its EPs or operating the system exactly at an EP, because as singular discreet points in the parameter space, EPs are prone to instabilities, noise, fabrication imperfections, and fluctuations during the operation of the system. Having a continuous surface of EPs, and hence an ES provides robustness against experimental instabilities because such instabilities, fluctuations and noises will move the system from one EP on the surface to another EP on the surface. As a result, many exotic features of EPs can be clearly observed and utilized allowing us to have maximum benefit from EPs. We have introduced a photonic system in Chapter 4 and demonstrated that unidirectional coupling between CW and CCW modes of a WGM resonator creates a surface of EPs, and hence an ES. In this Chapter, we utilize the chiral behavior at an EP and on ES to demonstrate chiral and degenerate perfect absorption.

5.1 Exceptional surfaces in WGM resonators via chiral coupling

EPs are consequence of non-Hermiticity in systems, and they are completely distinct from the Hermitian degeneracies known as the diabolic points (DPs). At a DP the eigenvalues of the system coalesce, however their eigenvectors are orthogonal. On the other hand, at an EP, both eigenvalues and eigenvectors of the system coalesce (i.e., the system has single eigenvalue and a corresponding eigenvector). Therefore, a system operating at an EP, losses its dimensionality and behaves as a singularity point in the parameter space [1-8]. EPs have been created in many different physical systems, and their chiral behavior and sensitivity to perturbations have been for applications [9-17]. Loss-induced lasing is another exotic feature of EPs which have attracted significant interest and fueled the research and discussions on EPs [18-22].

One can create EPs in a physical system in many ways which involves controlling the coupling strength, tuning loss-gain ratio or loss-imbalance, and creating asymmetric coupling between modes by controlling scattering behavior between them. All of these established methods rely on introducing additional loss or gain. In PT-symmetric systems with balanced gain and loss, EPs are accessed through tuning the coupling between loss and gain systems [18-19, 21-26]. Introducing loss or gain to create EPs also brings quantum noise which deteriorates coherence properties and signal-to-noise ratio which are not good for applications such as sensing [11, 30, 31], spontaneous emission control [32,33], or spectral filtering. Therefore, methods which do not require additional gain or loss are needed. One of such methods is placing Rayleigh scatterers in the mode volume of a resonator and tuning their distance and location which helps control scattering from one mode to the other to establish asymmetric coupling [9, 26]. However, accurately positioning the scatterers and keeping them stably is a very difficult task. Another method is establishing unidirectional coupling between CW and CCW modes of WGM resonators, which we have discussed in Chapter 4 [9,10]. In addition to this method, one could use parametric modulation or post-selection in quantum systems [27-29].

As discussed in Chapter 4, we achieved unidirectional coupling between the CW and CCW modes of a WGM resonator using an end-mirror at one of the output ends of the waveguide which is used to couple light in and out of the WGM resonator. Such a system can open the way for many applications [30,32, 34-39].

In Chapter 4, we have used a photonic circuit where a feedback loop with an attenuator and phase shifter was used as an end-mirror, which made it difficult to have access to reflection and transmission modes for an input in the CCW direction. In this Chapter, we replaced the feedback loop with a tunable fiber-loop mirror which remedies the problem encountered in Chapter 4. This new system is given in Figure. 5-1a, and b, where the fiber-loop mirror couples the light in the CW direction to the CCW mode, but the CCW mode does not couple back to the CW mode [28]. This system is robust against the perturbations and the noises and always operates on the ES and hence at an EP. The magnitude of the reflection of the fiber-loop mirror is tuned via in-line polarization controller inserted into the loop. A phase shifter (PS) inserted just before the fiber-loop mirror helps to control and tune the phase of the light back-reflected towards the CCW mode of the resonator. We have used this new system to probe many interesting features of Ess and demonstrate quartic reflection and absorption spectra [40]and chiral perfect absorption.

The frequency degenerate CW and CCW modes of the whispering gallery resonator used in this study are in the 1440nm band with an intrinsic quality factor of 7.7×10^5 measured at the deep undercoupling regime when the end-mirror was bypassed. Without the mirror, the system is degenerate and symmetric (Fig. 5-1c). CW and CCW modes have the same resonance frequency and linewidth (i.e., they are degenerate). The resonator was carefully fabricated and the modes were choses such that there is no inter-modal coupling between CW and CCW modes and hence there is no back-reflection for lights input in the CW and CCW directions. Transmission for the CW mode, T_{cw}, is detected at D_2 and the transmission for CCW, T_{ccw}, is detected at D_1. Reflection for the CW mode, R_{cw}, is detected at D_1 and the reflection for the CCW mode, R_{ccw}, is detected at D_2. As

shown in Fig. 5-1c that transmission spectra for inputs in the CW and CCW directions have Lorentzian dips whereas reflection spectra are zero (i.e., no resonances), proving that the system is symmetric and the modes are not coupled to each other. Hence the absorption $A_{cw(ccw)} = 1 - T_{cw(ccw)} - R_{cw(ccw)}$ is also symmetric and equal for both input directions. Moreover, the loading curve of the CW and CCW modes given in the inset of the Figure 5-1c confirms the symmetry in the waveguide-resonator coupling conditions. Figure 5-1d shows an optical microscopy image of the fiber-coupled on-chip microsphere used in our experiments.

Introducing the end-mirror as in Figure 5-1a, breaks the symmetry in the system and provides an asymmetric coupling between the CW and CCW modes. Using the coupled mode theory (CMT) we can describe our system as $\partial_t A = -iH_{ES}A$ where $A = (a_{cw}, a_{ccw})^T$, a_{cw} and a_{ccw} are the field amplitudes of the CW and CCW modes respectively. And H_{ES} corresponds to the Hamiltonian of the system and is given by

$$H_{ES} = \begin{pmatrix} \omega_0 - i\Gamma & 0 \\ \kappa & \omega_0 - i\Gamma \end{pmatrix} \quad (5.1)$$

where, $\omega_0 - i\Gamma$ are the complex frequencies of the degenerate CW and CCW modes, and $\Gamma = (\gamma_0 + \gamma_1)/2$ is the total loss, due to the waveguide-resonator coupling and the intrinsic loss, and κ is strength of the unidirectional coupling between the CW and CCW modes. The zero in the off-diagonal element implies that the coupling from one of the modes, CCW, to the other one, CW, is zero. The value of κ is related to the reflectivity of the end-mirror and waveguide-resonator coupling as $\kappa = r\gamma_1$, where the mirror reflectivity could be defined with its magnitude and phase as $r = |r|\exp(i\phi)$. This Hamiltonian has degenerate eigenvalues and eigenvectors expressed as $\omega_{1,2} = \omega_0 - i\Gamma$ and $a_{1,2} = (0, 1)^T$, respectively. For any non-zero reflectivity of the mirror, the system will be operating at the EP, and hence plotting the Eps as the phase and magnitude of the reflectivity is varied will define a surface, an ES, on which all points are Eps.

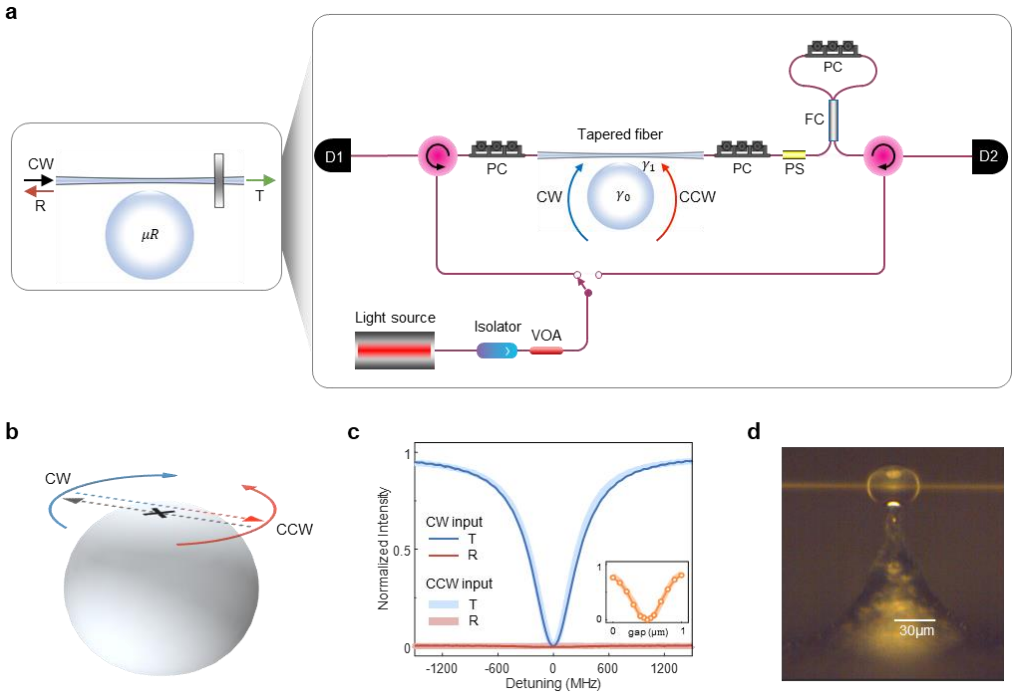

Figure 5-1:a, Optical system used in our experiments to demonstrate ES and chiral perfect absorption. End-mirror is implements using a fiber-loop reflector constructed using a 50:50 fiber coupler (FC) and a polarization controller (PC) The magnitude of the reflection is controlled via the PC and the reflection phase is controlled via a phase shifter (PS). Γ_0 is the intrinsic loss of the resonator, γ_1 is the loss due to the waveguide-resonator coupling, D1, 2 are the photodetectors, and the VOA is the variable optical attenuator. (b), The circuit in (a) establishes a unidirectional coupling between CW and CCW modes, in the sense that the CW mode couples to the CCW mode, while the CCW mode does not couple back to the CW mode. (c), Symmetric transmission and reflection spectra for the CW and CCW modes of the resonator, at the critical coupling condition, where the reflection values are zero, and the transmission spectra exhibit Lorentzian lineshapes. The inset presents the loading curve for CW and CCW modes, where by changing the gap distance between the waveguide and resonator, we are changing the coupling condition from the under coupling to the critical coupling, where the transmission becomes zero, and then to the overcoupling regime, until the fiber touches the resonator. (d), An optical microscope image of the tapered fiber coupled microsphere resonator used in the experiments.

It is clear that any perturbation (such as thermal fluctuations, environmental effects or loss affecting both the CW and CCW modes in the same way) that modifies the diagonal elements will shift the system to a new ES with a new complex frequency determined by the new resonance frequency and loss However, any perturbations, which modify off-diagonal elements or perturb the

diagonal elements in different ways, will destroy the degeneracy and move the system off the ES, leading to mode splitting. For example, a nanoscatterer in the mode volume of the resonator will scatterer light from CW to CCW and from CCW to CW modes thus modify the off-diagonal elements. If we assume that the zero off-diagonal element becomes δ because of the scatterer, the eigenvalues of the system will become $\omega_{1,2} = \omega_0 - i\Gamma \mp \sqrt{\kappa\delta}$, which implies the presence of mode splitting.

5.2 Squared Lorentzian Reflection Spectra

The Lorentzian (quadratic) lineshapes of the transmission spectra for the CW and the CCW modes of our microsphere in the absence of the end-mirror is shown Figure 5-1c. Transmission in this case can be written as $T_{cw(ccw)} \propto 1/(1 + {\gamma_0}^2/\Delta^2)$ for the critical coupling (i.e., $\gamma_0 = \gamma_1$) for both the CW and CCW modes. Indeed, even in the presence of the end-mirror, transmission spectra are given by the same expression. Reflection spectra do not exhibit any resonance and have zero value for both the CW and CCW modes in the absence of the end-mirror. However, it is significantly modified when the end-mirror is inserted: The reflection spectra for the CCW mode does not exhibit a resonance but now achieves a constant non-zero value depending on the reflectivity of the mirror. Reflection spectra for the CW mode, on the other hand, is represented by $R_{cw} \propto 1/(1 + {\gamma_0}^2/\Delta^2)^2$, which has a squared Lorentzian or a quartic lineshape. We then conclude that the system has symmetric transmission but asymmetric reflection spectra. More importantly, the reflection spectra have squared Lorentzian lineshape. Figure 5-2a shows a typical reflection spectra obtained in our experiments when the resonator-waveguide is set at critical coupling. Squared Lorentzian feature and flattening of the resonance dip is clearly seen. The experimental data is fitted via two different functions: the product of two Lorentzian functions $f_1 = L_1 L_2$, and the sum of two Lorentzian functions $f_2 = {L_1}' + {L_2}'$. The function given as the product of two

Lorentzians$L_k = A_k\Delta_k/(\Delta_k - i\Gamma_k)$ with $k = 1,2$ provides a much better fit and is able to catch the flat bottom of the reflection spectra. We measured the reflection spectra at various values of $|r|$ and ϕ when the system is operated at the critical coupling, performed curve fitting and estimated Δ_k and Γ_k from each measured spectra. We then plotted $\Delta w = \Delta_1 - \Delta_2$ and $\Delta\Gamma = \Gamma_1 - \Gamma_2$ as a function of $|r|$ and ϕ, reconstructing an ES (Figure 5-2b, c). We note that on an ES, we should have$\Delta_1 = \Delta_2$ and $\Gamma_1 = \Gamma_2$ and hence $\Delta w = 0$ and $\Delta\Gamma = 0$. ES reconstructed from the data obtained in our experiments exhibits non-zero but very small values for Δw and $\Delta\Gamma$ when compared the resonance frequency and the linewidth of the initial resonance mode before the end-mirror is inserted. The reconstructed surfaces have Δw in the range $[-6.8MHz, 3.4MHz]$ and $\Delta\Gamma$ in the range of $[-5.4MHz, 8.8MHz]$.

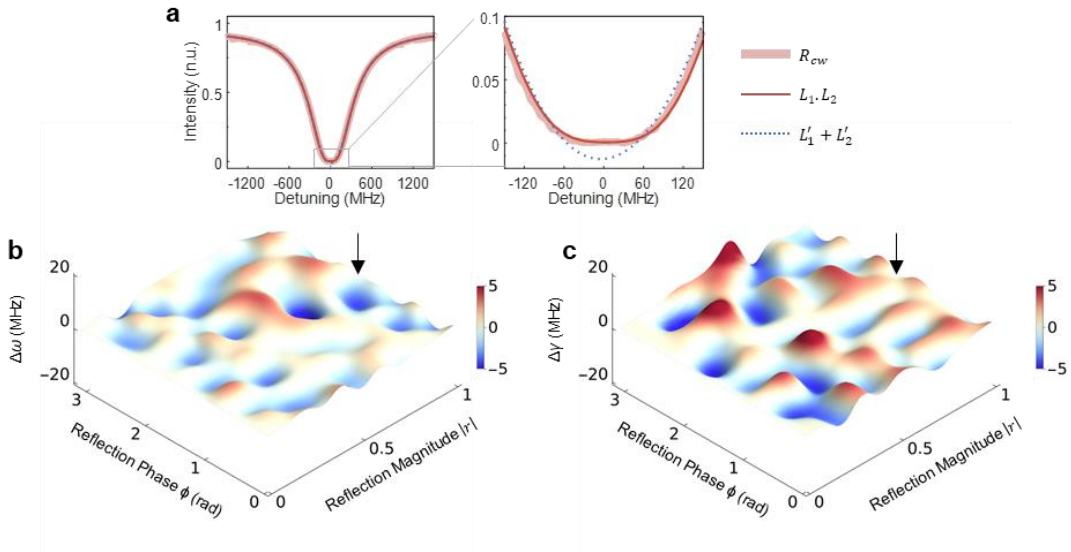

Figure 5-2: Squared Lorentzian and quartic lineshape of the reflection spectra for the CW mode, which is fitted via squared Lorentzian function $f_1 = L_1L_2$ and the sum of double Lorentzian function $f_2 = L_1{}' + L_2{}'$. Squared Lorentzian function gives a better fit implying that the reflection spectra have a quartic lineshape. (b), and (c) present the constructed surface for the Δw and $\Delta\Gamma$ respectively. The arrows are depicting the location of reflection spectra presented at (a).

If we normalized this to the frequency of the resonance at the $207.3THz$ and the linewidth $502\ MHz$ of the resonance at the critical coupling, we find $|\Delta w/\omega_0| \lesssim 10^{-8}$ and $\Delta\Gamma/\Gamma_0 \lesssim 10^{-2}$,

which is confirms that in fact our system operates on the ES. The variations from zero value for Δw and $\Delta\Gamma$ may be attributed to numerical fitting noise, electrical noise, etc.

As we discussed above, perturbations affecting the diagonal elements of the Hamiltonian will shift our system from one ES to another ES with a new complex frequency (i.e., degenerate eigenvalues). In order to show this, we performed experiments at different waveguide-resonator coupling conditions because coupling condition modifies Γ (i.e., imaginary part of the complex frequency). Typical examples of reconstructed ES obtained at the undercoupling and overcoupling regimes are shown in Figure 5-3 and Figure 5-4, respectively.

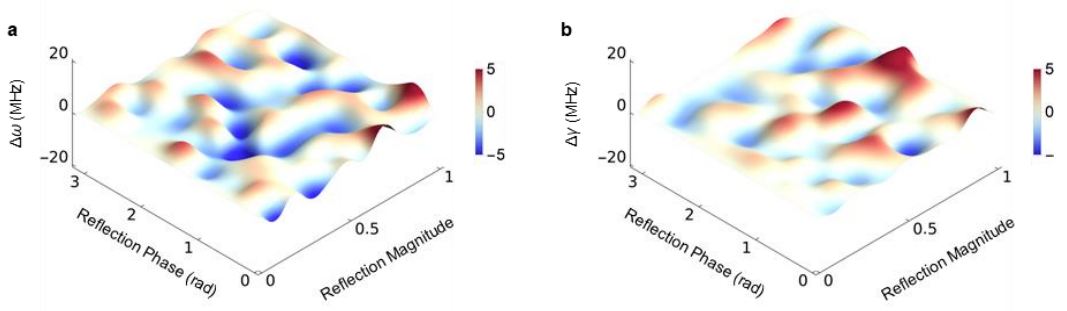

Figure 5-3: Constructed ES at the undercoupling regime. A, Δw, b, $\Delta\gamma$.

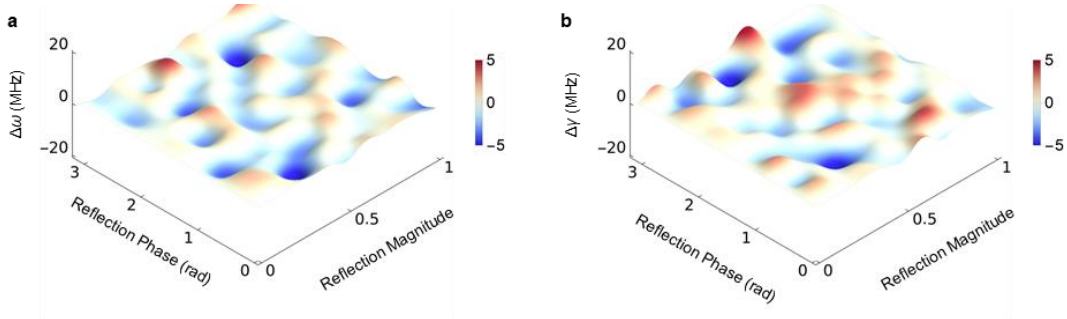

Figure 5-4: Constructed ES at the Overcoupling regime. A, Δw, b, $\Delta\gamma$.

It is worthful to note that, for all of the studied coupling regimes, Δw fluctuated in the range of $[-7.4MHz, 6.9MHz]$ and $\Delta\Gamma$ values are in the range of $[-5.5MHz, 8.8MHz]$ which when

normalized with the frequency ω_0 and linewidth Γ of the resonance without the end-mirror yield $|\Delta w/\omega_0| \lesssim 10^{-8}$ and $\Delta\Gamma/\Gamma \lesssim 10^{-2}$. This implies that our system is in fact operates on the ES.

5.3 Chiral Perfect Absorption on ES

We have measured reflection and transmission spectra for CW and CCW inputs at various coupling conditions, and then calculated the absorption spectra from these acquired spectra using $A_{cw(ccw)} = 1 - R_{cw(ccw)} - T_{cw(ccw)}$. We first set the end-mirror reflectivity to 1, that is $|r| = 1$. For this case, since all of the CCW incident (right incident in Figure 5-1a) reflects back from the mirror, no light enters to the resonator and therefore the absorption for the CCW incident is zero, however, for the CW incident (left incident in Figure 5-1a) all of the light couples to the CW mode and then after fully reflecting back from the mirror it couples to the CCW mode of the resonator. Then we can calculate the absorption spectrum using $A_{cw} = 1 - R_{cw}$. We have also measured all the absorption and insertion losses L_{cw} and L_{ccw} due to components used in the setup when the resonator is not coupled to the system, corresponding to the off-resonant losses. For the CW input mode, the loss is denoted as For the CW input, reflection is detected at D_1, and since the mirror reflectivity is $|r| = 1$, transmission (detection at D_2) is zero. Figure 5-5 presents the reflection spectra (i.e., red curve) and the calculated absorption spectra (i.e., purple curve) at undercoupling, critical coupling and overcoupling regimes. Squared Lorentzian reflection and absorption spectra are clearly seen at the critical coupling: while the reflection spectra have flat bottom, the absorption spectra have a flat top lineshape. Additionally, since the reflection becomes zero at the zero detuning frequency from the resonance, (i.e., $\Delta \to 0$ $R_{cw} = 1/(1 + {\gamma_0}^2/\Delta^2)^2 \to 0$), the absorption is 1 (i.e., $A_{cw} = 1$), referring to the perfect absorption of the light at the critical coupling Figure 5-5dpresents the measured reflection and calculated absorption at zero-detuning ($\Delta \to 0$) as we vary the coupling (i.e., distance gap between the tapered fiber and the resonator). At the $gap = 0.5\mu$m,

we observe critical coupling and hence the absorption becomes $A_{cw} = 1$. Since absorption for the CCW input is zero, this perfect absorption is chiral.

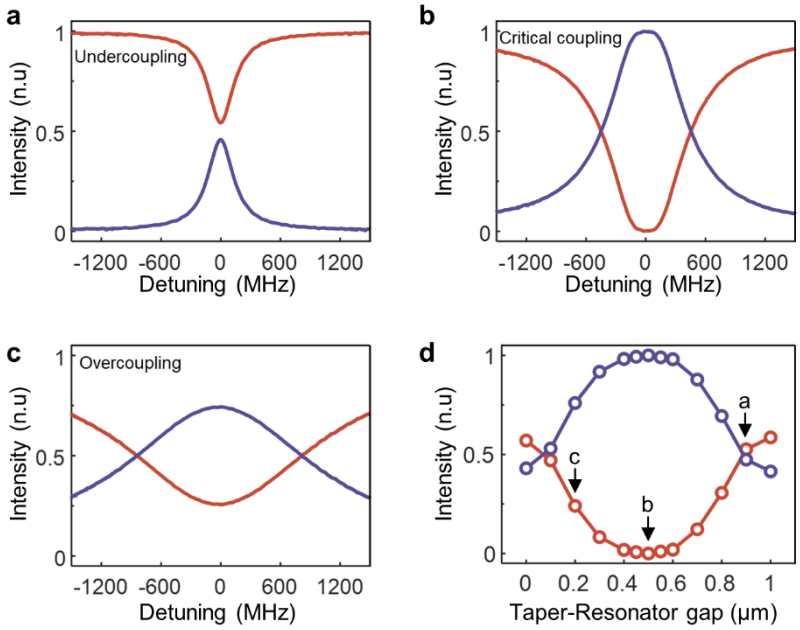

Figure 5-5: Chiral and perfect absorption on an exceptional surface with fully reflective end-mirror $|r| = 1$. Absorption spectra A_{cw} (purple curves) are inferred from the measured reflection spectra R_{cw} (red curves) using $A_{cw} + R_{cw} = 1$ for a CW input. Spectra measured at (a), undercoupling regime, (b), critical coupling, and c, overcoupling regime reveal perfect absorption on the ES with a quartic absorption lineshape only for critical coupling, as in (b). As the system moves away from the critical coupling regime the quartic behaviour becomes indiscernible. D, measured reflection and calculated absorption exactly at the ES frequency (i.e., zero detuning) for various taper-resonator coupling strength γ_1 determined by the gap between the taper and the resonator show the highest absorption at the critical coupling (i.e., gap equals to ~0.5μm) where we have $R_{cw} = 0$ and thus $A_{cw} = 1$. As the system moves from critical coupling towards undercoupling or overcoupling regimes, absorption at the resonance monotonously decreases. Circles are the values extracted from experimental data and the straight lines are inserted as guides to the eye. The labelled points in d are obtained from the spectra shown in (a), (b), and (c). For a CCW input, all the light is back-reflected by the mirror and no light reaches the resonator, therefore absorption is zero, $A_{ccw} = 0$, and hence chiral absorption on the ES.

5.4 Theoretical Model and Numerical Simulations

Our system can be described with the coupled differential equations,

$$\frac{da_{cw}}{dt} = -(i\Delta + \Gamma)a_{cw} - \sqrt{\gamma_1}a_{in,cw} \quad (5.2)$$

$$\frac{da_{ccw}}{dt} = -(i\Delta + \Gamma)a_{ccw} - \sqrt{\gamma_1}a_{in,ccw} \quad (5.3)$$

where a_{cw} and a_{ccw} are the field amplitudes of the clockwise (CW) and counter-clockwise (CCW) modes in the resonator; $a_{in,cw}$ and $a_{in,ccw}$ are the field amplitudes of the inputs to the resonator in the CW (forward) and CCW (backward) directions; Δ is the detuning between the laser and resonance frequency; and $\Gamma = (\gamma_0 + \gamma_1)/2$ with γ_1 denoting the resonator-waveguide coupling loss and γ_0 denoting the all other loss except the coupling.

Using the input-output formalism, we have $a_{out,cw} = a_{in,cw} + \sqrt{\gamma_1}a_{cw}$ and $a_{out,ccw} = d_{ccw} = a_{in,ccw} + \sqrt{\gamma_1}a_{ccw}$ as the outputs for the CW and CCW input directions, respectively, with d_{ccw} representing the field detected at the photodetector D_1. We note that $a_{out,ccw} = d_{ccw}$ represents the transmission for the input in the backward direction (CCW input) and reflection for the input in the forward direction (CW input). Thus D_1 measures the transmission (reflection) spectrum for the CCW (CW) input. A fiber-loop reflector with splitting coefficients r and t satisfying $|r|^2 + |t|^2 = 1$ splits $a_{out,cw}$ into two paths: The field in the first path, which is given by $d_{cw} = ta_{out,cw}$ goes directly to the photodetector D_2 and represents the transmitted field in the forward direction. The field $ra_{out,cw}$ in the second path propagates through a tuneable phase shifter (PS) with phase ϕ forming the back-reflected field $a_{r,cw} = re^{i\phi}a_{out,cw}$ in the CCW direction for an input in the forward direction (CW input). For the input $a_{in,ccw}$ in the CCW direction (backward

input), the field input to the tapered fiber waveguide is then given by $te^{i\phi}a_{in,ccw}$ and the reflected field is given as $ra_{in,ccw}$.

5.4.1. Input in the CW direction (left incidence, forward direction):

We first consider the case of input only in the forward direction (CW input). A portion of the $a_{out,cw}$ will be reflected into the CCW direction through the fiber-loop reflector as $a_{r,cw} = re^{i\phi}a_{out,cw}$. Therefore, when considering the system, we need to modify the rate equation describing the CCW field in the resonator as:

$$\frac{da_{cw}}{dt} = -(i\Delta + \Gamma)a_{cw} - \sqrt{\gamma_1}a_{in,cw} \tag{5.4}$$

$$\frac{da_{ccw}}{dt} = -(i\Delta + \Gamma)a_{ccw} - \sqrt{\gamma_1}a_{r,cw} = -(i\Delta + \Gamma)a_{ccw} - \sqrt{\gamma_1}re^{i\phi}a_{out,cw} \tag{5.5}$$

At steady state ($da_{cw}/dt = 0$ and $da_{ccw}/dt = 0$) we find a_{cw} and a_{ccw} as

$$a_{cw} = -\frac{\sqrt{\gamma_1}}{i\Delta+\Gamma}a_{in,cw} \tag{5.6}$$

$$a_{ccw} = -\frac{\sqrt{\gamma_1}}{i\Delta+\Gamma}a_{r,cw} = -\frac{\sqrt{\gamma_1}}{i\Delta+\Gamma}re^{i\phi}a_{out,cw} = -\frac{\sqrt{\gamma_1}}{i\Delta+\Gamma}re^{i\phi}\left(a_{in,cw} + \sqrt{\gamma_1}a_{cw}\right)$$

$$= -re^{i\phi}\frac{\sqrt{\gamma_1}}{i\Delta+\Gamma}\left(1 - \frac{\gamma_1}{i\Delta+\Gamma}\right)a_{in,cw} \tag{5.7}$$

Similarly, output in the CCW direction (corresponding to back-reflected light for the CW input) is expressed in the modified input-output relation as

$$a_{out,ccw} = d_{ccw} = a_{r,cw} + \sqrt{\gamma_1}a_{ccw} = \left(1 - \frac{\gamma_1}{i\Delta + \Gamma}\right)a_{r,cw} = \left(1 - \frac{\gamma_1}{i\Delta + \Gamma}\right)re^{i\phi}a_{out,cw}$$

$$= \left(1 - \frac{\gamma_1}{i\Delta+\Gamma}\right)re^{i\phi}\left(a_{in,cw} + \sqrt{\gamma_1}a_{cw}\right) = \left(1 - \frac{\gamma_1}{i\Delta+\Gamma}\right)re^{i\phi}\left[a_{in,cw} - \frac{\gamma_1}{i\Delta+\Gamma}a_{in,cw}\right]$$

$$= re^{i\phi}\left(1 - \frac{\gamma_1}{i\Delta+\Gamma}\right)^2 a_{in,cw} \tag{5.8}$$

Thus, the field at D_1 for the input in CW direction is $a_{out,ccw} = re^{i\phi}\left(1 - \frac{\gamma_1}{i\Delta+\Gamma}\right)^2 a_{in,cw}$ from which we find the reflection spectrum R_{cw} of the system for the CW input as:

$$R_{cw} = \left|\frac{d_{ccw}}{a_{in,cw}}\right|^2 = \left|\frac{a_{out,ccw}}{a_{in,cw}}\right|^2 = |r|^2\left|\left(1 - \frac{\gamma_1}{i\Delta+\Gamma}\right)^2\right|^2 = |r|^2\left|1 - \frac{2\gamma_1}{i\Delta+\Gamma} + \frac{{\gamma_1}^2}{(i\Delta+\Gamma)^2}\right|^2$$

$$= |r|^2\left[\frac{\Delta^2+(\Gamma-\gamma_1)^2}{\Gamma^2+\Delta^2}\right]^2 = |r|^2\left[\frac{4\Delta^2+(\gamma_0-\gamma_1)^2}{4\Delta^2+(\gamma_0+\gamma_1)^2}\right]^2 \tag{5.9}$$

Similarly, we can describe the field at D_2 as

$$d_{cw} = ta_{out,cw} = t\left(a_{in,cw} + \sqrt{\gamma_1}a_{cw}\right) = t\left(1 - \frac{\gamma_1}{i\Delta+\Gamma}\right)a_{in,cw} \tag{5.10}$$

Then the transmission spectrum T_{cw} of the system is found as

$$T_{cw} = \left|\frac{d_{cw}}{a_{in,cw}}\right|^2 = |t|^2 \left|1 - \frac{\gamma_1}{i\Delta+\Gamma}\right|^2 = |t|^2 \left[\frac{4\Delta^2+(\gamma_0-\gamma_1)^2}{4\Delta^2+(\gamma_0+\gamma_1)^2}\right] \quad (5.11)$$

Note the extra term of $\frac{{\gamma_1}^2}{(i\Delta+\Gamma)^2}$ in the expression for R_{cw} compared to T_{cw} already implies that the lineshape of R_{cw} will be significantly different than that of T_{cw}. Using the relation $A_{cw} + T_{cw} + R_{cw} = 1$, we can write the absorption for the input in the CW direction as:

$$A_{cw} = 1 - T_{cw} - R_{cw} = 1 - |t|^2 \left[\frac{4\Delta^2+(\gamma_0-\gamma_1)^2}{4\Delta^2+(\gamma_0+\gamma_1)^2}\right] - |r|^2 \left[\frac{4\Delta^2+(\gamma_0-\gamma_1)^2}{4\Delta^2+(\gamma_0+\gamma_1)^2}\right]^2 \quad (5.12)$$

which reveals that the absorption spectrum is a superposition of a Lorentzian (i.e., T_{cw} spectrum) and a squared Lorentzian function (i.e., R_{cw} spectrum). This implies that one can set the lineshape of the absorption spectrum by finely tuning the system parameters. For example, when the system is set at critical coupling ($\gamma_0 = \gamma_1$, that is $\Gamma = \gamma_0 = \gamma_1$), absorption A_{cw} is written as

$$A_{cw(\gamma_0=\gamma_1)} = 1 - |t|^2 \left(\frac{1}{1+\gamma_0^2/\Delta^2}\right) - |r|^2 \left(\frac{1}{1+\gamma_0^2/\Delta^2}\right)^2 \quad (5.13)$$

which with the choice of completely reflecting end-mirror ($t = 0, r = 1$) reduces to $A_{cw(\gamma_0=\gamma_1)} = 1 - \left(\frac{1}{1+\gamma_0^2/\Delta^2}\right)^2$, implying a squared-Lorentzian lineshape, and with the choice of completely transmitting end-mirror ($t = 1,\ r = 0$) reduces to $A_{cw(\gamma_0=\gamma_1)} = 1 - \left(\frac{1}{1+\gamma_0^2/\Delta^2}\right)$, implying a Lorentzian lineshape. Thus, provided that $\gamma_0/\gamma_1$is kept constant, one can tune the absorption lineshape from a Lorentzian to a squared-Lorentzian form by varying reflectivity of the end-mirror

(Figure 5-6). Similarly, one can tune the lineshape by tuning the waveguide-resonator coupling strength (varying γ_0/γ_1) if r and t are kept constant (Figure 5-7).

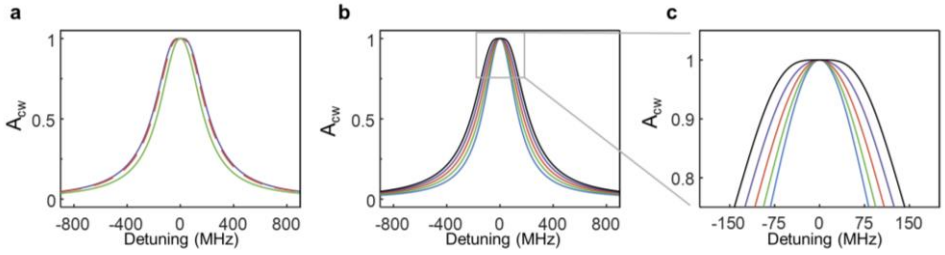

Figure 5-6. Effect of the reflectivity of the end-mirror on the normalized absorption spectra obtained on the exceptional surface (ES) at critical coupling for CW input. **(a)**, Calculated absorption spectra simulating experimentally investigated end-mirror: Fully-reflecting end-mirror ($|r|^2 = 1, |t|^2 = 0$) (purple), 50:50 half-mirror ($|r|^2 = |t|^2 = 1/2$) (green), and 10:90 mirror ($|r|^2 = 0.9, |t|^2 = 0.1$) (dashed red). **(b)**, Calculated absorption spectra simulating an end-mirror with different reflectivity values, corresponding to various settings of the fiber-loop reflector: $|r|^2$ equals to 0 (blue), ¼ (green), ½ (red), ¾ (purple), and 1 (black). These settings simulate end-mirrors with zero-reflection (blue), 25% reflection (green), 50% reflection (red), 75% reflection (purple), and 100% reflection (black), respectively. **(c)**, Enlarged view of the top part of the spectra shown in **(b)**. Transition of the spectra from Lorentzian lineshape to a flat-top quartic lineshape is clearly seen as the reflectivity of the end-mirror is increased.

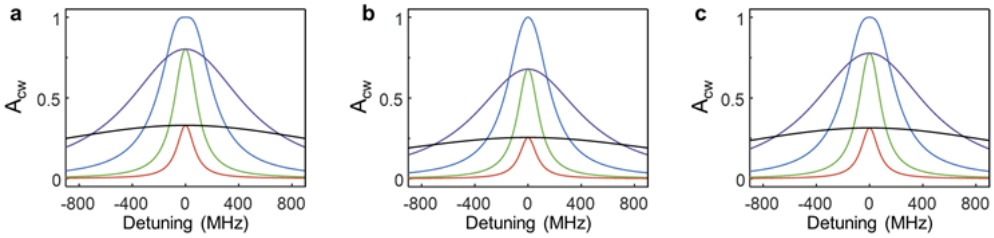

Figure 5-7. Effect of the waveguide-resonator coupling regime on the normalized absorption spectra. Coupling regime is quantified by the ratio γ_0/γ_1 (ratio of the resonator losses γ_0 including material, scattering and radiation, to the waveguide-resonator coupling loss γ_1). In the simulation results shown in (a), (b), and (c), we used $\gamma_0/\gamma_1 = 1$ (critical coupling, blue), $\gamma_0/\gamma_1 = 5$ (undercoupling, green), $\gamma_0/\gamma_1 = 20$ (deep undercoupling, red), $\gamma_0/\gamma_1 = 1/5$ (overcoupling, purple), and $\gamma_0/\gamma_1 = 1/20$ (deep overcoupling, black). Calculated absorption spectra simulating experimentally investigated end-mirrors: (a), Fully-reflecting end-mirror ($|r|^2 = 1, |t|^2 = 0$), (b), 50:50 half-mirror ($|r|^2 = |t|^2 = 1/2$), and (c), 10:90 end-mirror with 90% reflection ($|r|^2 = 0.9, |t|^2 = 0.1$). Flat-top quartic lineshape is clearly seen at the critical coupling $\gamma_0/\gamma_1 = 1$ in **(a)** and (c) but not in (b), implying the effect of end-mirror reflectivity on the process. As the system is moved to undercoupling or overcoupling regime, the flat-top becomes obscure and the lineshape becomes Lorentzian.

5.4.2. Input in the CCW direction (left incidence, backward direction):

We now consider the case where the input is in the backward direction (CCW input). The output field $a_{out,ccw}$ goes directly to the detector D_1(i.e., no back-reflection into the CW mode). The field input to the waveguide after the fiber-loop reflector is $te^{i\phi}a_{in,ccw}$. There is no input in the CW direction, thus we have $a_{in,cw} = 0$ and $a_{cw} = 0$ (i.e., no coupling between the CW and CCW modes and input only in the CCW direction). Thus, it is enough to consider only the modified rate equation:

$$\frac{da_{ccw}}{dt} = -(i\Delta + \Gamma)a_{ccw} - \sqrt{\gamma_1}te^{i\phi}a_{in,ccw} \quad (5.14)$$

At steady state ($da_{ccw}/dt = 0$) we find a_{cw} and a_{ccw} as

$$a_{ccw} = -\frac{\sqrt{\gamma_1}te^{i\phi}}{(i\Delta+\Gamma)}a_{in,ccw} \quad (5.15)$$

Substituting into the modified input-output relation $a_{out,ccw} = d_{ccw} = te^{i\phi}a_{in,ccw} + \sqrt{\gamma_1}a_{ccw}$:

$$a_{out,ccw} = te^{i\phi}a_{in,ccw} + \sqrt{\gamma_1}a_{ccw} = te^{i\phi}a_{in,ccw} - \frac{\gamma_1 te^{i\phi}}{(i\Delta+\Gamma)}a_{in,ccw} =$$

$$te^{i\phi}\left(1 - \frac{\gamma_1}{(i\Delta+\Gamma)}\right)a_{in,ccw} \quad (5.16)$$

The field detected at D_1 for the input in CCW direction gives the transmission spectrum T_{ccw} as:

$$T_{ccw} = \left|\frac{d_{ccw}}{a_{in,cw}}\right|^2 = \left|\frac{a_{out,ccw}}{a_{in,cw}}\right|^2 = |t|^2 \left|\left(1 - \frac{\gamma_1}{(i\Delta + \Gamma)}\right)\right|^2 = |t|^2 \frac{\Delta^2 + (\Gamma - \gamma_1)^2}{\Gamma^2 + \Delta^2}$$

$$= |t|^2 \left(\frac{4\Delta^2 + (\gamma_0 - \gamma_1)^2}{4\Delta^2 + (\gamma_0 + \gamma_1)^2}\right) \quad (5.17)$$

For the CCW input, we calculate the reflection R_{ccw} as

$$R_{ccw} = \left|\frac{re^{i\phi} a_{in,ccw}}{a_{in,ccw}}\right|^2 = |r|^2 \quad (5.18)$$

which is constant for all frequencies and is significantly different from R_{cw} which exhibits a squared Lorentzian lineshape. We can then use the relation $A_{ccw} + T_{ccw} + R_{ccw} = 1$ to write absorption for the input in the CCW direction as

$$A_{ccw} = 1 - T_{ccw} - R_{ccw} = 1 - |r|^2 - |t|^2 \left(\frac{4\Delta^2 + (\gamma_0 - \gamma_1)^2}{4\Delta^2 + (\gamma_0 + \gamma_1)^2}\right) = |t|^2 \left(1 - \frac{4\Delta^2 + (\gamma_0 - \gamma_1)^2}{4\Delta^2 + (\gamma_0 + \gamma_1)^2}\right) \quad (5.19)$$

which reveals an absorption spectrum with Lorentzian lineshape. At critical coupling ($\gamma_0 = \gamma_1$, that is $\Gamma = \gamma_0 = \gamma_1$), absorption spectra A_{ccw} for a CCW input becomes

$$A_{ccw(\gamma_0 = \gamma_1)} = |t|^2 \left(1 - \frac{\Delta^2}{\Delta^2 + \gamma_0^2}\right) = |t|^2 \left(\frac{\gamma_0^2}{\Delta^2 + \gamma_0^2}\right) = |t|^2 \left(\frac{1}{1 + \Delta^2/\gamma_0^2}\right) \quad (5.20)$$

5.5. Intracavity field intensity at exceptional surfaces of different coupling regimes:

We performed numerical simulations of the system using COMSOL Multiphysics which allowed us to observe the intracavity field for CW and CCW inputs at different coupling regimes and hence on different exceptional surfaces (Figures 5-8 and 5-9). We performed the simulations

for two specific cases, that is for a perfectly reflecting end-mirror (Figure 5-8) and for an end-mirror with half reflecting and half transmitting, $|r|^2 = |t|^2 = 1/2$ (Figure 5-9).

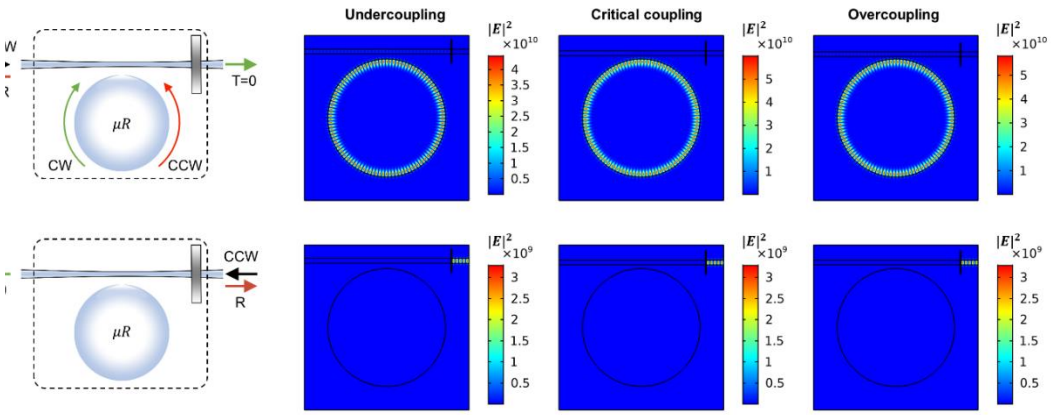

Figure 5-8**.** Intracavity field intensity for (a), clockwise CW and (b), counterclockwise CCW input on the exceptional surfaces associated with different waveguide-microresonator (μR) coupling regimes for a system with fully reflective end-mirror. Dotted boxes in the left panels represent the ES-device composed of a waveguide-coupled resonator with the end-mirror. Black arrows denote the CW and CCW input ports of the ES-device. Intracavity field intensity for the CW input is highest at the critical coupling. Note the absence of field inside the resonator for the CCW input.

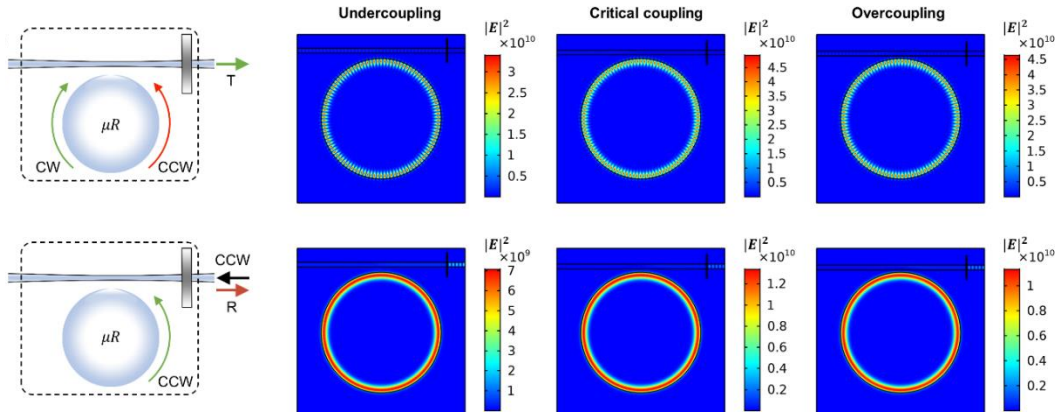

Figure 5-9. Intracavity field intensity for (a), clockwise CW and (b), counterclockwise CCW input on the exceptional surfaces associated with different waveguide-microresonator (μR) coupling regimes when the end-miror is half reflecting and half transmitting. Dotted boxes in the left panels represent the ES-device composed of a waveguide-coupled resonator with the end-mirror. Black arrows denote the CW and CCW input ports of the ES-device. Intensity for the CW input is highest at the critical coupling. Note the standing-wave like pattern for the CW input and the traveling wave pattern for the CCW input.

Simulations show the formation of a standing-wave like pattern inside the resonator only for the CW input. This is because, the reflector is placed at only one of the waveguide ends (the end in the CW direction) and thus the light transmitted through.

The waveguide-coupled resonator in the CW direction is back reflected in the CCW direction. As a result, there are two fields propagating in the CW and CCW directions in the resonator even if the input to the system is in the CW direction. The response of the system for these end-mirrors (i.e., the fully reflective and the partially reflective end-mirrors) differ significantly for the CCW input: In Figure 5-8 there is no field in the resonator (thus no absorption for CCW input) because the CCW input is fully reflected and does not reach to the resonator. In Figure 5-9, while half of the input CCW field is reflected back to the input port, the other half travels and couples into the resonator in the CCW direction (thus there is absorption for CCW input). Since there is no end-mirror in the CCW input direction, there is only CCW traveling wave in the resonator for the CCW input (Figure 5-9). This asymmetric response for the CCW input is observed at all exceptional surfaces associated with waveguide-resonator coupling regimes. Simulations also show that the ES emerging at the critical coupling leads to the highest intracavity-field intensity for CW input. On a given ES associated with a coupling strength, the intracavity field intensity is stronger for the CW input than for the CCW input.

5.6. Normalization procedure to assess the absorption from experimentally obtained spectra:

To correctly assess the absorption on exceptional surfaces, it is important that all losses in the system (i.e., including the insertion and return losses of various components and the propagation losses in the connecting fibers but not the resonator-related losses) incurred during light propagation in the experimental setup are measured and are considered in the normalization

process. We have measured losses in the path of the fields input in the CW and CCW directions from the setup input-point until the detection at the detectors D_1 and D_2. Since these paths are different for different input directions, the losses are different, and they should be measured individually and included in the normalization of the associated experimentally obtained spectra. We measured these losses by recording off-resonant (i.e., without the resonator) transmission (reflection) and reflection (transmission) for the input in the CW (CCW) direction at detectors D_1 and D_2, respectively.

5.6.1 Normalization for CW input:

If there were no losses, off-resonant transmitted and reflected field intensities for an input with intensity $I_{in/cw}$ in the CW direction would be given as $I_{T/cw-off-\,lossless} = |t|^2 I_{in/cw}$ and $I_{R/cw-off-\,lossless} = |r|^2 I_{in/cw}$. When the resonator is inserted into the setup, we can take the losses into account by multiplying the measured transmitted field intensity $I_{T/cw}(\omega)$ and the measured reflected field intensity $I_{R/cw}(\omega)$ respectively with $\left(I_{T/cw-off-\,lossless}/I_{T/cw-off}\right)$ and $\left(I_{R/cw-off-\,lossless}/I_{R/cw-off}\right)$. Here, $I_{T/cw-off}$ and $I_{R/cw-off}$ denote the measured off-resonant transmitted and reflected field intensities, respectively. Thus, transmission and reflection spectra normalized with respect to the input $I_{in/cw}$ after taking the losses into account is given by the normalized transmission $T_{cw}(\omega)$

$$T_{cw}(\omega) = \frac{I_{T/cw}(\omega)\left(\frac{I_{T/cw-off-lossless}}{I_{T/cw-off}}\right)}{I_{in/cw}} = \frac{I_{T/cw}(\omega)\left(\frac{|t_1|^2 I_{in/cw}}{I_{T/cw-off}}\right)}{I_{in/cw}} = \frac{I_{T/cw}(\omega)}{I_{T/cw-off}}|t|^2 \quad (5.21)$$

and the normalized reflection $R_{cw,N}(\omega)$

$$R_{cw}(\omega) = \frac{I_{R/cw}(\omega)\left(\frac{I_{R/cw-off-lossless}}{I_{R/cw-off}}\right)}{I_{in/cw}} = \frac{I_{R/cw}(\omega)\left(\frac{|r_1|^2 I_{in/cw}}{I_{R/cw-off}}\right)}{I_{in/cw}} = \frac{I_{R/cw}(\omega)}{I_{R/cw-off}}|r|^2 \quad (5.22)$$

In our experiments, effective reflection and transmission by the end-mirror is controlled by polarization controllers in the fiber loop. We can tune the reflectivity of the end-mirror that controls the coupling of the CW light into the CCW between 0 and 1. The normalized absorption spectra is then given as $A_{cw}(\omega) = 1 - T_{cw}(\omega) - R_{cw}(\omega)$:

$$A_{cw}(\omega) = 1 - \frac{I_{\frac{T}{cw}}(\omega)}{I_{\frac{T}{cw}-off}}|t|^2 - \frac{I_{\frac{R}{cw}}(\omega)}{I_{\frac{R}{cw}-off}}|r|^2 = 1 - \frac{I_{T/cw}(\omega)}{I_{T/cw-off}} + \left(\frac{I_{T/cw}(\omega)}{I_{T/cw-off}} - \frac{I_{R/cw}(\omega)}{I_{R/cw-off}}\right)|r|^2 \quad (5.23)$$

.

5.6.2. Normalization for CCW input:

Since the paths CW and CCW fields propagate are different, the losses they experience are different, too. For CCW input, off-resonant transmission measured at D_1 helps determine the losses for the CCW input in the system before the resonator is inserted. This loss is given as $I_{T/ccw-off-lossless} = |t|^2 I_{in/ccw}$. When a resonator is inserted into the setup, we can in principle take the losses into account by multiplying the measured transmitted field intensity $I_{T/ccw}(\omega)$ and the measured reflected field intensity $I_{R/ccw}(\omega)$ respectively with $\left(I_{T/ccw-off-lossless}/I_{T/ccw-off}\right)$ and $\left(I_{R/ccw-off-lossless}/I_{R/ccw-off}\right)$. Here, $I_{T/ccw-off}$ and $I_{R/ccw-off}$ denote the off-resonant transmitted and reflected field intensities, respectively. We note that $I_{R/ccw-off-lossless}/I_{R/ccw-off} = 1$ in our system because resonator does not play any role. Following the procedure outlined for CW input above, we find the expression for the normalized transmission spectra for the input in CCW direction as

$$T_{ccw}(\omega) = \frac{I_{T/ccw}(\omega)\left(\frac{I_{T/ccw-off-lossless}}{I_{T/ccw-off}}\right)}{I_{in/ccw}} = \frac{I_{T/ccw}(\omega)\left(\frac{|t|^2 I_{in/ccw}}{I_{T/ccw-off}}\right)}{I_{in/ccw}} = \frac{I_{T/ccw}(\omega)}{I_{T/ccw-off}}|t|^2 \quad (5.24)$$

The normalized reflection spectrum is just given by the normalized drive of VOA and that is

$$R_{ccw}(\omega) = \frac{I_{R/ccw}(\omega)\left(\frac{I_{R/ccw-off-lossless}}{I_{R/ccw-off}}\right)}{I_{in/ccw}} = \frac{I_{R/ccw}(\omega)}{I_{in/cw}} = |r|^2 \quad (5.25)$$

Then we calculate the normalized absorption spectrum as

$$A_{ccw}(\omega) = 1 - T_{ccw}(\omega) - R_{ccw}(\omega) = 1 - \frac{I_{T/ccw}(\omega)}{I_{T/ccw-off}}|t|^2 - |r|^2$$

$$= \left(1 - \frac{I_{T/ccw}(\omega)}{I_{T/ccw-off}}\right)|t|^2 \quad (5.26)$$

5.7 Experimental results

Here we provide experimental data and evidence that support the theoretical model and conclusions derived from it.

5.7.1 Effect of end-mirror reflectivity on the reflection and absorption spectra at critical coupling

The theoretical model predicts that when the system is at the critical coupling, reflection spectra on the ES exhibit squared Lorentzian lineshape with perfect absorption occurring at the ES frequency. The experimentally obtained reflection spectra R_{cw} reveal the expected squared Lorentzian lineshape (i.e., flat bottom) at the critical coupling at all end-mirror reflectivity values (Figure 5-10). We note that when the end-mirror reflectivity is varied from $|r| = 1$ to $|r| = 0.2$,

there is gradual change in the lineshape of the absorption spectra from quartic lineshape (squared Lorentzian, flat top) to a Lorentzian-like lineshape while the reflection spectra stay squared Lorentzian all the time. This is expected from Eqs. (5-13) and (5-23) which state that the absorption spectra is a superposition of a Lorentzian and squared Lorentzian lineshapes, and the value of $|r|$ determines the weight of the squared Lorentzian lineshape in the superposition: The higher the $|r|$ is, the more squared Lorentzian the absorption spectra are.

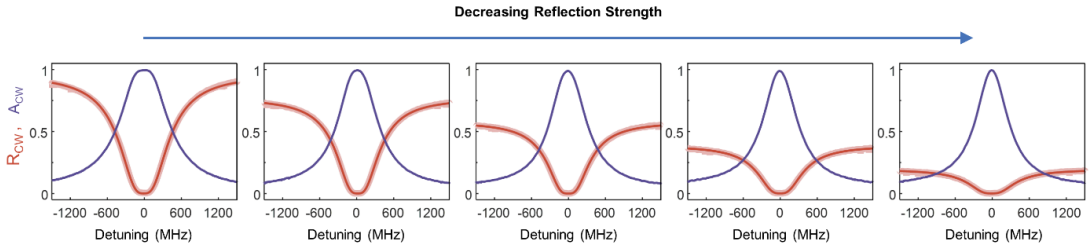

Figure 5-10**.** Experimentally obtained normalized reflection spectra R_{cw} and the calculated absorption spectra A_{cw} on the exceptional surface associated with critical coupling at various values of the reflection magnitude |r| of the end-mirror. Reflection and absorption spectra exhibit squared Lorentzian lineshapes with flat bottom and flat top respectively. Perfect absorption takes place at the ES-frequency at all non-zero values of |r| . Reflection and absorption at frequencies other than the ES-frequency depend on |r|.

We also observe that decreasing the reflectivity of the end-mirror, the FWHM of the absorption spectra decreases from 880 MHz to 500MhzRecall that if $|r| = 0$, the system will not be on ES and all the light in the CW direction will be transmitted to output port of the fiber exhibiting a Lorentzian transmission spectrum. It is also important to note that since Fig. 5-10 is obtained at the critical coupling, we always observe perfect absorption even if $|r|$ is very small but not zero. This is also expected as the theory suggests that the system is on an ES with squared Lorentzian reflection spectra any non-zero value of the end-mirror reflectivity (see also experimental data in Figure 5-6).

5.7.2 Effect of coupling regime on the reflection and absorption spectra

We have performed experiments at different coupling regimes using end-mirrors with various reflectivities. If all parameters of the system are kept constant but only the resonator-waveguide coupling strength is modified, a new ES will emerge at each coupling regime as we experimentally showed in Figs. 5-3 and 5-4.

We first set the end-mirror reflectivity to $|r| = 1$ (fully reflecting end-mirror) and varied the coupling from undercoupling to overcoupling through the critical coupling point. We experimentally obtained the reflection spectra R_{cw} and calculated the absorption spectra A_{cw} as $A_{cw} = 1 - R_{cw}$ (Note that in this case $T_{cw} = 0$). We observed that although the system always stays on an ES at all coupling conditions, perfect absorption with quartic (i.e., squared Lorentzian) lineshape is seen only at the critical coupling (Figure 5-11). As the system moves away from the critical coupling, the ES emerging at the new coupling regimes does not satisfy the perfect absorption condition. While the ES at the critical coupling clearly exhibits a quartic lineshape in the reflection and absorption spectra, this feature is not clear as the system moves away from critical coupling.

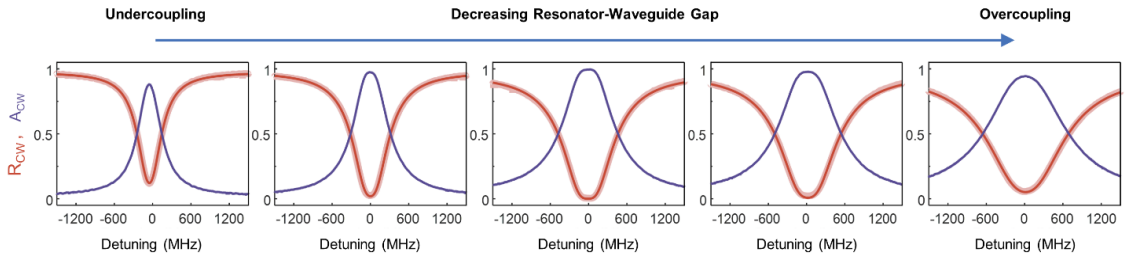

Figure 5-11. Experimentally obtained reflection and absorption spectra on exceptional surfaces associated with different resonator-waveguide coupling regimes. Quartic lineshape (squared Lorentzian) with flat bottom resonance dip for the reflection spectra R_{cw} (red) and with flat top resonance peak for absorption spectra A_{cw} (purple) is clearly seen at the critical coupling. As the resonator-waveguide coupling strength moves away from critical coupling towards undercoupling (increasing gap) or overcoupling (decreasing gap) regimes, quartic features fade away and spectra look more like Lorentzian. CPA takes place only at critical coupling.

Next, show that an ES in our system leads to chiral and perfect absorption also for partially reflecting end-mirrors. The tuneable fiber-loop reflector allows us to construct symmetric mirrors with varying reflection and transmission coefficients. As examples, here we present the results of experiments performed with a 10:90 end-mirror (10% transmission and 90% reflection) and a 50:50 end-mirror (50% transmission and 50% reflection) at different taper-waveguide coupling regimes. The spectra are normalized with the power input to the tapered waveguide for left incidence and with the power just before the reflector for right incidence. We note that varying the reflection phase ϕ does not affect the observed features. Typical spectra obtained for the 10:90 and 50:50 end-mirrors at different taper-waveguide coupling regimes are shown in Figure 5-12 and Figure 5-13, respectively.

When the end-mirror is not 100% reflecting, we have access to reflection and transmission spectra (T_{cw}, R_{cw}) and (T_{ccw}, R_{ccw}) for left (CW direction) and right incidence (CCW direction) from which the normalized absorption spectra A_{cw} and A_{ccw} can be calculated using the expression $A_{cw(ccw)} + R_{cw(ccw)} + T_{cw(ccw)} = 1$. In the experiments, $T_{cw(ccw)}$ for left and right incidence exhibit typical resonance dips at the ES frequency with Lorentzian lineshapes. However, reflection spectra differed significantly: R_{cw} has a squared Lorentzian lineshape with a flattened resonance dip around the ES frequency (see Figure. 5-12) whereas R_{ccw} is constant ($e.g., R_{ccw} = 0.9$ for the 10:90 end-mirror and 0.5 for the 50:50 end-mirror) at all frequencies because it does not involve the resonator (see Figures 5-12 and 5-13). The chirality in this behaviour (asymmetry in reflection) stems from the larger absorption for the left incidence compared to the right incidence, and the degeneracy in the absorption is the result of the strong coupling between the CW and CCW modes of the resonator for left incidence (no coupling between them for right incidence). Indeed, the absorption spectrum A_{cw} for CW input (left incidence) is a superposition of a Lorentzian term coming from the transmission T_{cw} and a squared-Lorentzian term from R_{cw}, whereas A_{ccw} for

CCW input is always a Lorentzian. The weights of the Lorentzian and squared-Lorentzian terms in the superposition are determined by the reflectivity of the end-mirror (i.e., A_{cw} is squared Lorentzian for a 100% reflecting mirror and it is Lorentzian for a 0% reflecting mirror) and hence the effective unidirectional coupling κ between the CW and CCW modes. Another parameter that affects κ and thereby the contribution of Lorentzian and squared-Lorentzian terms to the final lineshape is the waveguide-resonator coupling strength γ_1 through the expression $\kappa = r\gamma_1$. Thus, when the taper-resonator coupling or the reflectivity of the end-mirror is varied, the system continues to be on an ES but the lineshape and the overall amount of the absorption are altered.

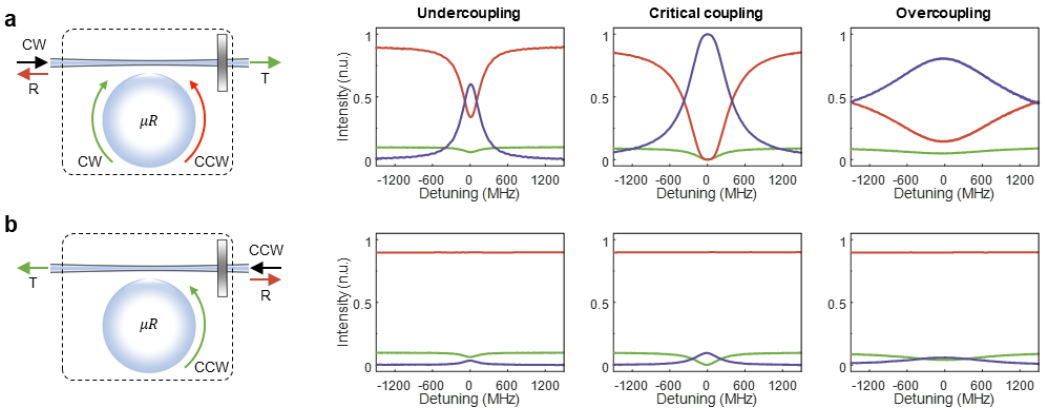

Figure 5-12: Chiral perfect absorption on an exceptional surface. Dotted boxes in the left panels in a and b represent the ES-device composed of a waveguide-coupled microresonator (μR) with an end-mirror with 90% reflection and 10% transmission. Black arrows denote the CW and CCW input ports of the ES-device, and red and green arrows represent the corresponding reflection and transmission ports. In the case of CW input as in a, the field inside μR has both CW and CCW components whereas it has only CCW component for the CCW input as in b. Measured transmission $T_{cw(ccw)}$ (green) and reflection $R_{cw(ccw)}$ (red) spectra and calculated absorption $A_{cw(ccw)} = 1 - R_{cw(ccw)} - T_{cw(ccw)}$ (purple) spectra of the ES-device at the undercoupling, critical coupling and overcoupling regimes for CW (upper panel) and CCW (lower panel) inputs. T_{cw} and T_{ccw} have Lorentzian lineshapes with resonance dips at zero-detuning (ES frequency) at all coupling regimes; R_{ccw} is constant at all frequencies; and R_{cw} exhibits squared Lorentzian spectra. Perfect absorption on the ES with quartic lineshape is observed at the critical coupling for CW input only implying chiral perfect absorption. A_{cw} is at least ten times larger than A_{ccw}, and hence chiral absorption at all coupling conditions.

Interestingly, a gradual transition from a quartic (squared-Lorentzian) form to a quadratic (Lorentzian) form in the A_{cw} lineshape takes place as the taper-resonator coupling moves from the critical coupling towards the undercoupling or overcoupling regime (see Figures 5-12 and 5-13, upper panels) or the reflectivity of the end-mirror is tuned. Perfect absorption with flat-top squared Lorentzian lineshape is clearly seen when the system is at the critical coupling and the input is CW (see Figures 5-12 and 5-13).

To summarize, we have observed: i) perfect absorption on the exceptional surface with quartic lineshape at the critical coupling for the CW input; ii) chiral absorption in the sense that absorption for CW input is much larger than that for CCW input on all exceptional surfaces created at different waveguide-resonator coupling; iii) while the quartic feature is dominant and is clearly seen for the reflection and absorption spectra obtained for the ES at the critical coupling, these features become vague for exceptional surfaces obtained when the system moves away from critical coupling; and iv) T_{cw} and T_{ccw} have Lorentzian lineshapes with resonance dips at zero-detuning (ES frequency) at all coupling regimes; R_{ccw} is constant at all frequencies; and $\mathrm{R_{cw}}$ exhibits squared Lorentzian spectra.

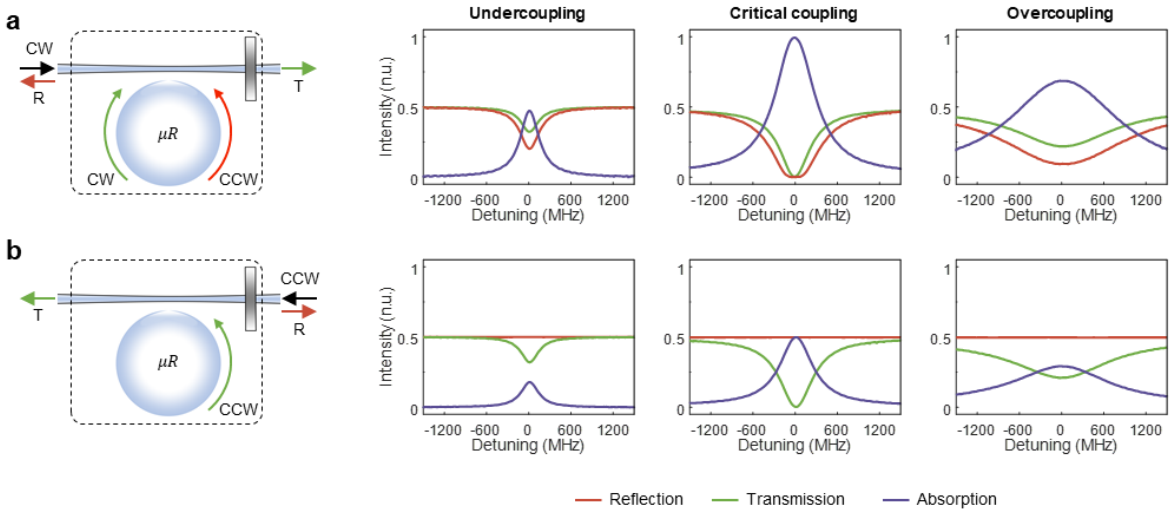

Figure 5-13. Chiral perfect absorption on exceptional surfaces at different resonator-waveguide coupling regimes for a 50:50 end-mirror. Dotted boxes in the left panels in (a) and (b) represent the ES-device composed of a waveguide-coupled microresonator (μR) with an end-mirror with 50% reflection and 50% transmission. Black arrows denote the CW and CCW input ports of the ES-device, and red and green arrows represent the corresponding reflection and transmission ports. In the case of CW input as in (a), the field inside μR has both CW and CCW components whereas it has only CCW component for the CCW input as in (b). Measured transmission $T_{cw(ccw)}$ (green) and reflection $R_{cw(ccw)}$ (red) spectra and calculated absorption $A_{cw(ccw)} = 1 - R_{cw(ccw)} - T_{cw(ccw)}$ (purple) spectra of the ES-device at the undercoupling, critical coupling and overcoupling regimes for CW (upper panel) and CCW (lower panel) inputs. T_{cw} and T_{ccw} have Lorentzian lineshapes with resonance dips at zero-detuning (ES frequency) at all coupling regimes; R_{ccw} is constant at all frequencies; and R_{cw} exhibits squared Lorentzian spectra. Perfect absorption on the ES is observed at the critical coupling for CW input only, implying chiral perfect absorption. A_{cw} is always larger than $A_{(ccw)}$, and hence chiral absorption at all coupling conditions.

5.7.3 Effect of losses that are not related to the waveguide-coupled resonator coupling regime on the reflection and absorption spectra

Absorption spectra presented so far have been obtained using the normalization process introduced previously. This process considers the effect of losses, which do not originate directly from the waveguide-coupled resonator with an end-mirror. These losses include insertion, return, and propagation losses induced by the optical components and connectors used in the setup. Such losses are measured without inserting the resonator into the setup. One may consider two different alternatives to the method introduced previously. One such approach may be to use $A_{cw(ccw)} =$

$1 - R_{cw(ccw)} - T_{cw(ccw)}$ where $R_{cw(ccw)}$ and $T_{cw(ccw)}$ are the measured transmission and reflection, respectively, and $A_{cw(ccw)}$ is the calculated absorption which includes all losses (i.e., not related with the resonator and the end-mirror). Normalization is then done with respect to the input power. Another approach may be to measure off-resonant losses $L_{cw(ccw)}$ and use it in the absorption calculation as $A_{cw(ccw)} = 1 - R_{cw(ccw)} - T_{cw(ccw)} - L_{cw(ccw)}$ where normalization is again done with respect to the input power. Figures 5-14 to 5-16 present a comparison of these different ways of calculating absorption for 0:100 (fully reflecting), 50:50, and 10:90 end-mirrors, respectively. Note that for the 0:100 end-mirror, absorption for a CCW input is zero because all the input light is back-reflected

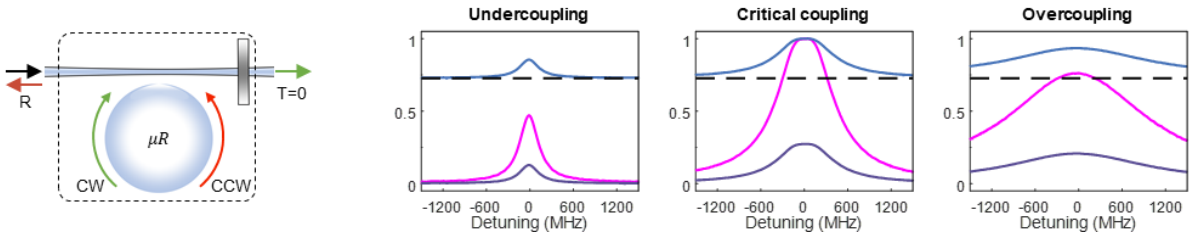

Figure. 5-14. Absorption spectra calculated from experimentally obtained transmission and reflection spectra on exceptional surfaces at different resonator-waveguide coupling regimes for a fully reflecting end-mirror (0:100) for CW input. Dashed line in the spectra denotes the level of losses not directly related to the resonator. Absorption spectra are calculated using $A_{cw(ccw)} = 1 - R_{cw(ccw)} - T_{cw(ccw)}$ (blue: spectra includes losses), $A_{cw(ccw)} = 1 - R_{cw(ccw)} - T_{cw(ccw)} - L_{cw(ccw)}$ (purple: losses are considered separately), and $A_{cw(ccw)} = 1 - R_{cw(ccw)} - T_{cw(ccw)}$ (magenta: normalization takes the losses into account. See Section I). Perfect absorption $A_{cw} = 1$ is achieved for the first and last cases (blue and magenta spectra). Since for a CCW input, all the light is reflected back and no light reaches the resonator, absorption is zero, $A_{ccw} = 0$ for all the cases. Thus, the system exhibits chiral absorption.

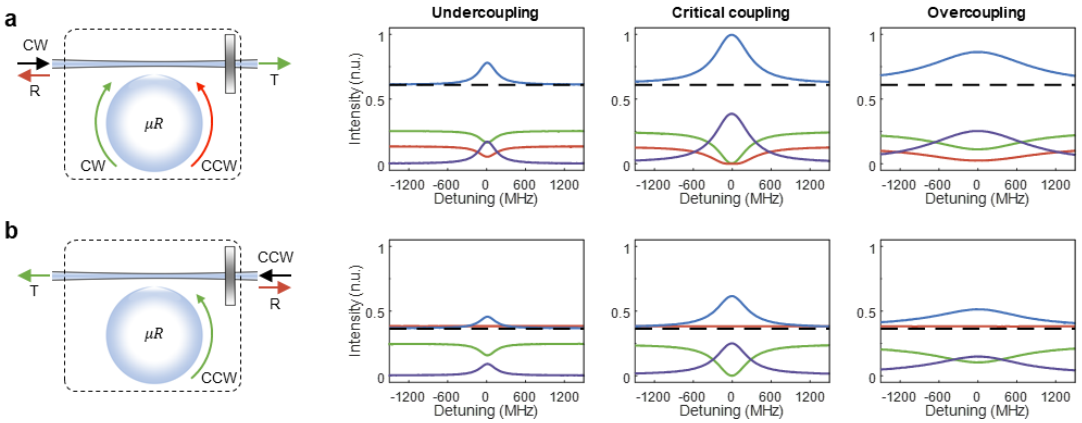

Figure 5-15. Chiral absorption on exceptional surfaces at different resonator-waveguide coupling regimes for a 50:50 end-mirror. Dashed line in the spectra denotes the level of losses not directly related to the resonator. Transmission $T_{cw(ccw)}$ (green) and reflection $R_{cw(ccw)}$ (red) spectra are measured with the resonator in place. Absorption spectra are calculated using $A_{cw(ccw)} = 1 - R_{cw(ccw)} - T_{cw(ccw)}$ (blue) or $A_{cw(ccw)} = 1 - R_{cw(ccw)} - T_{cw(ccw)} - L_{cw(ccw)}$ (purple). The latter denotes the absorption of the field remained after the losses are subtracted. Normalization is done with respect to input power. $A_{cw(ccw)} = 1 - R_{cw(ccw)} - T_{cw(ccw)}$ reaches unity at the ES-frequency at the critical coupling. Amount of observation in $A_{cw(ccw)} = 1 - R_{cw(ccw)} - T_{cw(ccw)} - L_{cw(ccw)}$ is limited by the losses $L_{cw(ccw)}$. For all cases, A_{cw} is always larger than $A_{(ccw)}$, and hence chiral absorption.

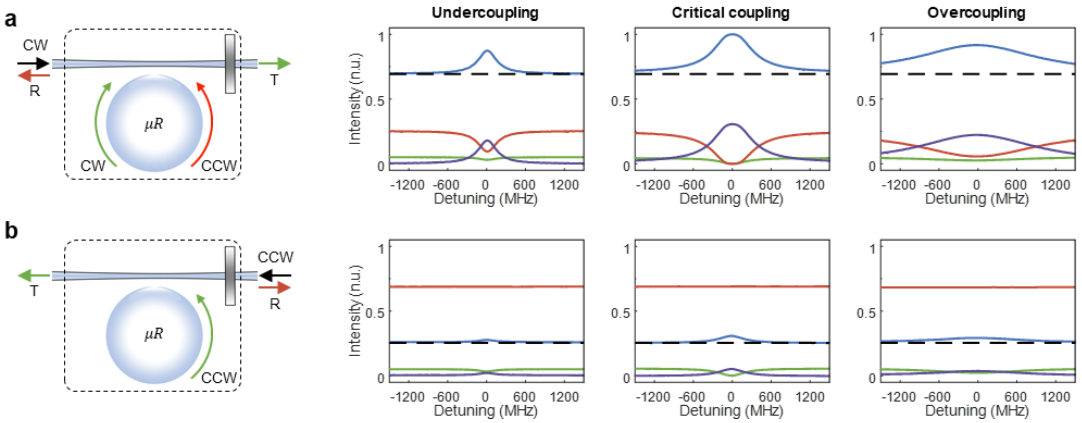

Figure 5-16. Chiral absorption on exceptional surfaces at different resonator-waveguide coupling regimes for a 10:90 end-mirror. Dashed line in the spectra denotes the level of losses not directly related to the resonator. Transmission $T_{cw(ccw)}$ (green) and reflection $R_{cw(ccw)}$ (red) spectra are measured with the resonator in place. Absorption spectra are calculated using $A_{cw(ccw)} = 1 - R_{cw(ccw)} - T_{cw(ccw)}$ (blue) or $A_{cw(ccw)} = 1 - R_{cw(ccw)} - T_{cw(ccw)} - L_{cw(ccw)}$ (purple). Normalization is done with respect to input power. $A_{cw(ccw)} = 1 - R_{cw(ccw)} - T_{cw(ccw)}$ reaches unity at the ES-frequency at the critical coupling. Amount of observation in $A_{cw(ccw)} = 1 - R_{cw(ccw)} - T_{cw(ccw)} - L_{cw(ccw)}$ is limited by the losses $L_{cw(ccw)}$. For all cases, A_{cw} is always larger than $A_{(ccw)}$, and hence chiral absorption.

For all the cases considered here, chiral absorption on the ES and squared Lorentzian absorption spectra are clearly seen. Perfect absorption with quartic lineshape at critical coupling is seen for the first two methods, that is for the normalization method introduced in the previous sections and for the case when losses are not separately considered. When off-resonant losses are included as in $A_{cw(ccw)} = 1 - R_{cw(ccw)} - T_{cw(ccw)} - L_{cw(ccw)}$, the amount of absorption $A_{cw(ccw)}$ at the ES frequency is limited by $L_{cw(ccw)}$. The absorption is maximum at the ES frequency but does not exhibit perfect absorption.

5.8 Degree of Chiral Absorption on ES:

Finally, we steer the system on the ES and determine the absorption A_{cw} and A_{ccw} at the ES frequency for the left CW (see Figure. 5-17a) and the right CCW (see Figure. 5-17b) incidence, respectively, by tuning the fiber-loop mirror parameters and the taper-resonator coupling. We present the results in Figure. 5-17 demonstrating that perfect absorption on an ES ($A_{cw} = 1$ at resonance with squared-Lorentzian lineshape) takes place for left incidence at the critical coupling for all reflectivity values $|r|$ of the end-mirror (Figure. 5-17a). For right incidence, on the other hand, conventional perfect absorption ($A_{ccw} = 1$ at resonance with Lorentzian lineshape) occurs at the critical coupling only for $|r| = 0$ (i.e., completely transmitting end-mirror), and A_{ccw} decreases with increasing $|r|$. As the taper-resonator gap increases from zero (i.e., overcoupling), A_{cw} and A_{ccw} first increase reaching its maximum value at the critical coupling, and then starts decreasing as the gap increases (the system moves towards deep undercoupling regime). Chirality of absorption can be better seen in the ratio $\xi = A_{ccw}/A_{cw}$ (Figure. 5-17c) which can be tuned in the range [0,1]: $\xi = 0$ denotes no absorption for right incidence ($A_{ccw} = 0$) corresponding to a fully reflecting end-mirror; $\xi = 1$ denotes equal absorption for incidence in both directions ($A_{ccw} =$

A_{cw}); and all other values of $0 < \xi < 1$ imply chiral absorption, that is $A_{cw} > A_{ccw}$, with higher chirality at higher $|r|$ and at taper-resonator gaps closer to the critical coupling condition.

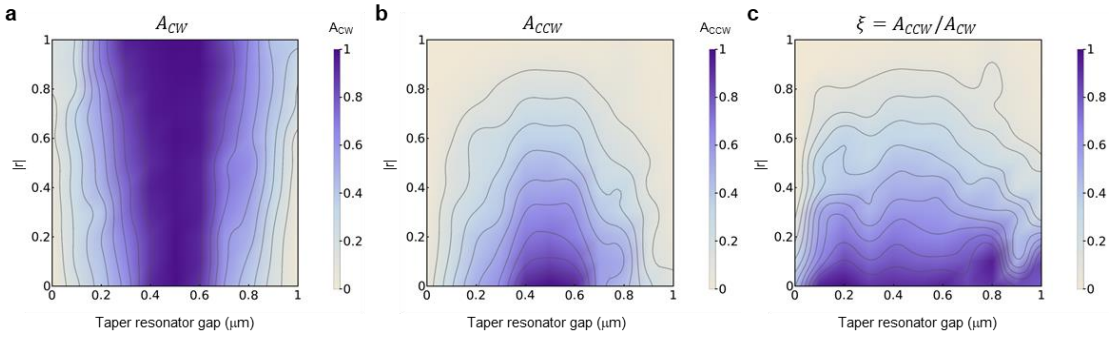

Figure 5-17: Tunable chiral absorption on an exceptional surface by varying reflection from the end-mirror or the waveguide-resonator coupling strength. (a), (b), The amount of absorption at the ES frequency for left (CW input) and right (CCW input) incidence can be tuned by controlling taper-resonator gap and the reflectivity |r| of the end-mirror, implemented with the fiber loop with a polarization controller. (c), Absorption ratio $\xi = A_{ccw}/A_{cw}$ of right incidence to left incidence at the ES frequency. CPA-ES is obtained at the critical coupling for left incidence. Critical coupling is achieved when the taper-resonator gap is 0.5 μm, with the gap smaller than 0.5 μm corresponds to overcoupling and a gap larger than 0.5 μm corresponds to undercoupling.

It is worth noting that ES does not only allow chiral absorption at the ES frequency but the involved degeneracy also provides a way to control the absorption bandwidth. We have observed that the absorption bandwidth defined as full-width at half-maximum is different for left and right incidence (i.e., chirality in bandwidth). More interestingly, we have found that compared to the conventional one-channel CPA at critical coupling, the absorption bandwidth on the ES is 1.26, 1.41, and 1.59 times larger for 50:50, 10:90, and fully reflecting end-mirrors, respectively. These values are close to the theoretically predicted values of 1.27, 1.50, and 1.55. The flattened absorption spectrum in the vicinity of critical coupling for left incidence may provide a remedy to the narrow absorption bandwidth of a conventional one-channel CPA (i.e., a waveguide-coupled

resonator operating at critical coupling)—a problem that has hindered progress in technologies relying on CPA.

5.9 Conclusion

In conclusion, we demonstrate a non-Hermitian optical device which exhibits exceptional surface (ES) and chiral perfect absorption. Since the device operates always exactly at an EP when on the ES, it provides a stable and controllable platform to study EP-related phenomena and processes, revealing chiral and degenerate perfect absorption on an ES with quartic reflection and absorption lineshapes as the defining hallmark. Our results will pave the way towards control of various optical processes and light-matter interactions exactly at an EP (not limited to the spectra in the vicinity of an EP), with potential applications ranging from chiral light-matter interaction, lasing, and emission to chiral nonlinear photonics and photovoltaics. Creating ES through a simple unidirectional coupling route between two modes can be extended to other physical platforms where the coupling between modes and systems can be made unidirectional by electrical, optical, photonics or acoustic feedback or back-reflection. Since no additional loss or gain is introduced into the system, ES obtained through unidirectional coupling can also benefit studies of quantum dynamics in non-Hermitian systems.

Chapter 6

Thermal response of WGM Microresonators on the Exceptional Surfaces

In this chapter we experimentally analyze the thermal response of the WGM microresonators on exceptional surfaces. It is well-known that the absorption of the input light by the resonator material produces heat which in turn shifts the resonance frequency via the thermo-optic effect. In Chapter 5, we have demonstrated perfect chiral absorption in a microresonator when it is operated on an ES. This perfect absorption should present itself as an increase in the temperature of the mode and hence as a shift in the resonance frequency. In this Chapter we study such thermal processes on an ES.

6.1 Introduction

Temperature changes affect a resonator in two ways. First, through the thermo-optic effect which describes how the refractive index of a material changes with temperature. For example, the thermo-optic coefficient for silica is reported as $dn_{eff}/dT = 1.19 \times 10^{-5} C^{-1}$. Second, through thermal expansion which will show itself as the increase of decrease in the size. For silica, thermal expansion coefficient is reported as $\frac{(1/R)dR}{dT} = 5.5 \times 10^{-7} C^{-1}$. Taking these two effects into account, we can describe the change in the resonance wavelength of a silica microresonator as [79]

$$\frac{\Delta\lambda}{\lambda} = \frac{\Delta n_{eff}}{n_{eff}} + \frac{\Delta R}{R} \quad (6.1)$$

An interesting thermal effect in WGM resonators emerges when a high-power tunable laser is used to probe the resonances: As the wavelength of the laser approaches the resonance wavelength of the WGM, light gradually couples into the cavity leading to heat generation due to material absorption, which in turn shift the resonance wavelength. When the wavelength of the laser is up-

scanned from shorter to longer wavelengths, the temperature increase in the mode will red-shift the resonance wavelength to longer wavelengths. This leads to resonance broadening. When the laser is down-scanned from longer to shorter wavelengths, the resonance wavelength shifts in the opposite direction of the laser, so the mode narrows down. We note that resonance broadening is observed when the frequency

Resonance broadening has been used for thermal locking of a laser to a resonance mode, and it allows to input light into the resonance mode for an extended time and helps build higher intracavity power enabling the observation of nonlinear processes easily.

In the following, we present our experimental results which clarify the effect of ES on the thermal response of a resonator.

6.2 Thermal Characterization

Figure 6-1 is the schematic of the experimental setup used for the thermal characterization of WGM resonator operating on an ES. We first investigated the dynamic thermal effect at various laser powers and wavelength scanning speeds. Speeds. In the absence of the end-mirror (i.e., fiber-loop mirror is removed), we measured the transmission spectra for the inputs in the CW and CCW directions, observing a resonance mode at 1472 nm with a Q-factor of 8×10^5. Figure 6-2 obtained at a laser power of $2.3mW$ and laser scanning speed of 8.7nm/sec (1.2THz/sec) shows a clear resonance broadening. The amount of broadening is the same for both the CW and the CCW modes (i.e., symmetric system).

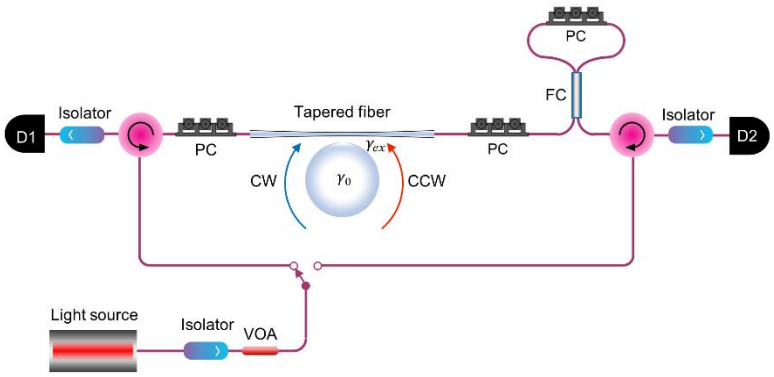

Figure 6-1: Schematic of the thermal characterization experiment.

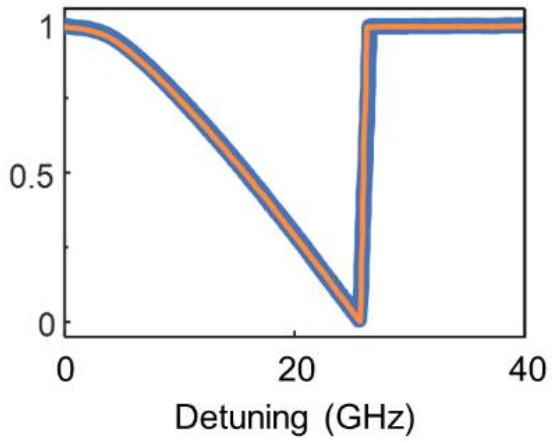

Figure 6-2: Resonance broadening in the absence of the end-mirror. The system is symmetric and thus the resonance broadening is symmetric, too, that is amount and the shape of the broadening is the same for CW and CCW inputs. Spectra are obtained at the laser power of $2.3mW$ and laser scanning speed of 8.7nm/sec (1.2THz/sec).

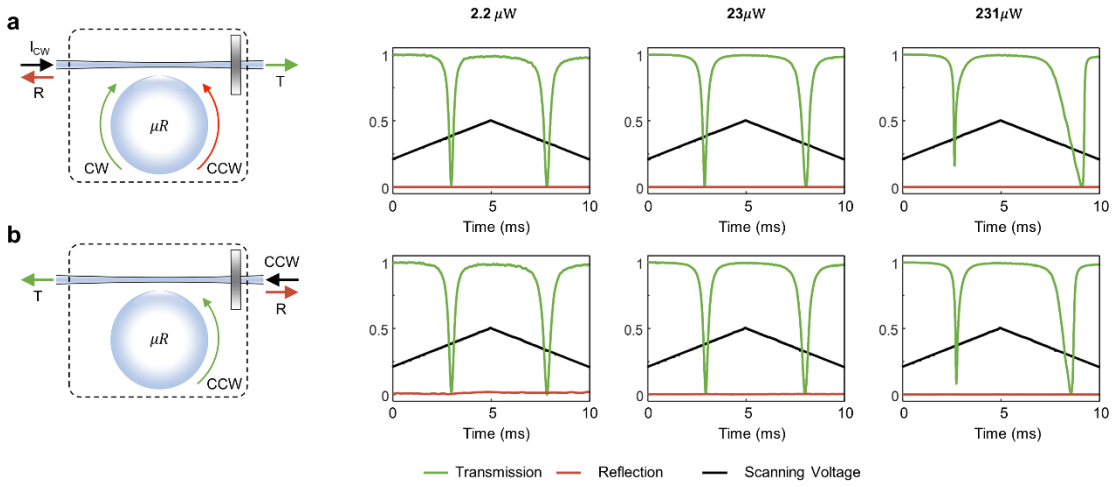

Figure 6-3: Transmission (green) and reflection (red) spectra for (a) CW and (b) CCW inputs for different input powers as the frequency of the input laser is scanned at 8.7nm/sec (1.2THz/sec) (black). Resonance broadening (narrowing) in the transmission is observed during frequency down scan (up scan).

Next, we inserted the end-mirror into the setup but set its reflectivity to zero and measured transmission spectra for CW and CCW inputs at various powers and constant laser scanning speed. Figure 6-3 shows the measured transmission spectra at powers of $2.2\mu W$, $23\mu W$ and $231\mu W$. We clearly see resonance broadening which increases as the power increases. We could not observe broadening at power levels lower than $2.2\mu W$. There is a small discrepancy in the amount of broadening for CW and CCW inputs. This discrepancy stems from the loss difference in the CW and CCW paths (i.e., $L_{cw} \neq L_{ccw}$). Figure 6-4 presents the frequency down-scan part of Fig. 6-3 to give an enlarged view of resonance broadening.

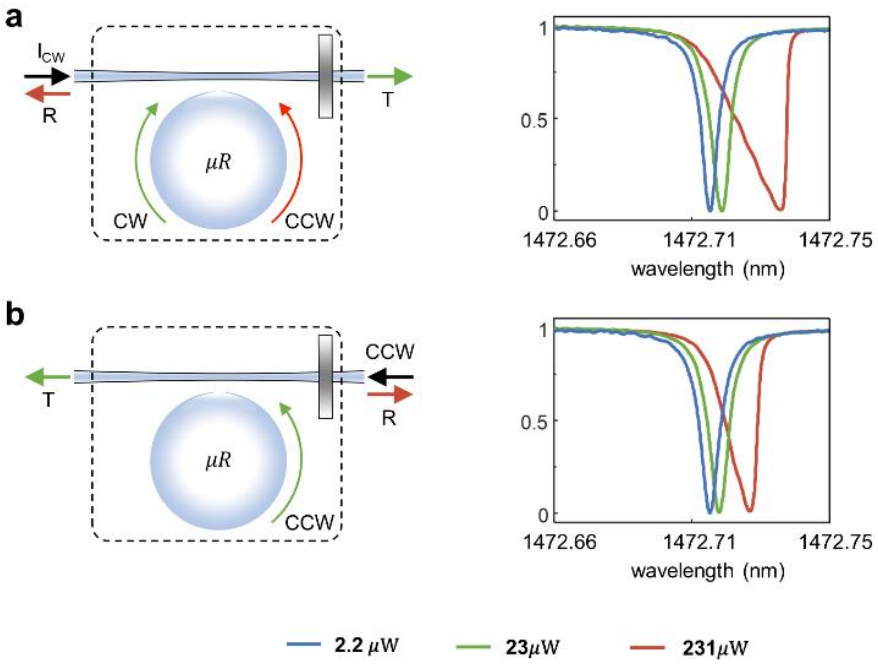

Figure 6-4: Enlarged view of the transmission spectra shown in Fig. 6-3. Only the frequency down-scan (wavelength up-scan) section is given here. Blue, green and red spectra are obtained at input powers of the $2.2\mu W$, $23\mu W$, $231\mu W$, respectively.

Next, by setting the end-mirror reflectivity to non-zero values, we operated the system on an ES and compared the thermal responses with the case when the end-mirror reflectivity is zero (not operating on an ES). Figure 6-5 compares the thermal response in the Lorentzian transmission spectra when the end-mirror reflectivity is set to $|r| = 0$ with the thermal response in the squared Lorentzian reflection spectra when $|r| = 1$ (no transmission spectra). It is clearly seen that the broadening is much larger in the reflection spectra obtained when the system in on the ES than that in the transmission spectra obtained when the system is not on the ES. In addition to the difference in the amount of broadening, we see a significant difference in the shape of the broadening, which exhibits a strong nonlinearity in the reflection spectra when the system is on the ES at (Fig. 6-5a). This nonlinearity is not observed at lower powers as shown in Fig. 6-5c. In order to better observe the resonance spectral differences for the full transmission and the full reflection cases, we zoomed

in the resonance dips in the spectra at which we observe a larger red-shift and flat bottom feature in the reflection spectra obtained on the ES (Fig. 65b, d).

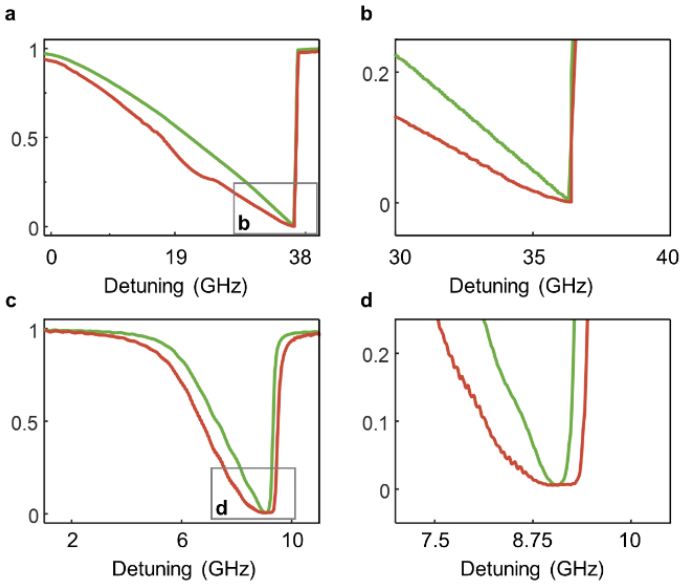

Figure 6-5: Transmission and reflection spectra obtained for CW input for end-mirror reflectivity $|r| = 0$ (no ES, green curve) and $|r| = 1$ (system is on the ES, red curve), respectively. (a) incident power is $38mW$, (b) zoomed resonance spectra of a, (c) incident power is $231\mu W$, and (d) zoomed resonance spectra of c.

In Figure 6-6, we present the experimental results showing the effect of the end-mirror reflectivity on the resonator thermal response for the CW incident (i.e., left incident) light with a power of $38mW$ We see that nonlinearity in the broadened resonance is clearly seen in the reflection spectra at end-mirror reflectivities as small as $R = 0.2$. Such a nonlinear shape is not seen in the transmission spectra. As it can be observed in the Figure 6-7, for CCW incident (i.e., right incident) we do not see the nonlinearity for the transmission spectra. For the CCW incident, the amount of thermal broadening is smaller than that for the CW input because power reaching to

the resonator-taper coupling point is smaller. This discrepancy between CW and CCW inputs is a result of the chiral or asymmetric absorption when the system is operated on an ES.

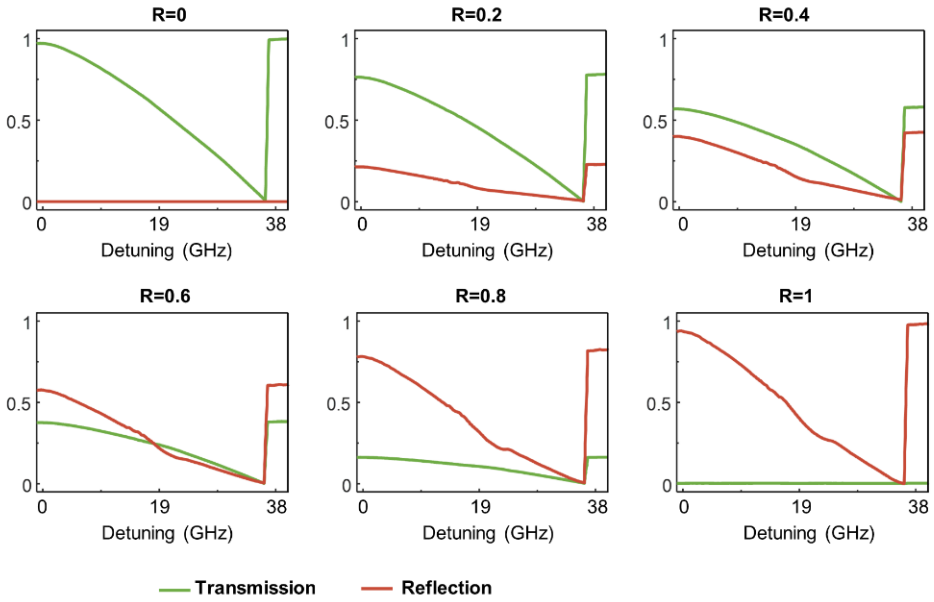

Figure 6-6: Effect of end-mirror reflectivity R on the thermal response of the resonator for CW input at a power of $38mW$. Reflection spectra (red) and transmission spectra (green).

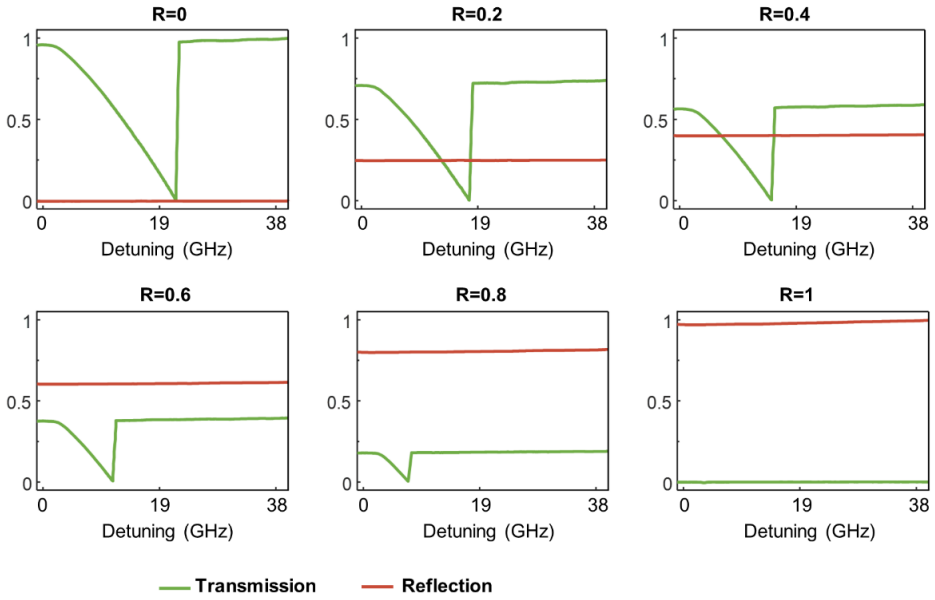

Figure 6-7: Effect of end-mirror reflectivity R on the thermal response of the resonator for CCW input at a power of $38mW$. Reflection spectra (red) and transmission spectra (green).

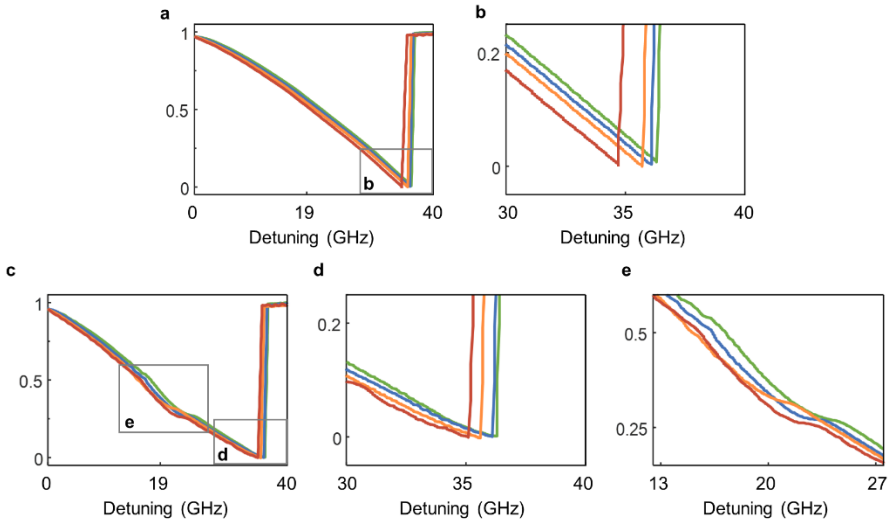

Figure 6-8: Effect of laser scanning speed on the thermal response for CW input when end-mirror reflectivity is a) zero (system is not on an ES) and c) one (system is on the ES). Red, yellow, blue and green curves are obtained for the scanning speeds of 35.4nm/sec (4.8THz/sec), 17.8nm/sec (2.4THz/sec), 8.7nm/sec (1.2THz/sec), 4.3nm/sec (0.6THz/sec), respectively. a) Transmission spectra when system is not on an ES ($|r| = 0$), b) Close up view of transmission resonance close to its dip, c) Reflection spectra when the system is on the ES with $|r| = 1$,d) close up view of reflection resonance close to its dip, e) close up view of the nonlinear section of the broadened reflection spectra.

Figure 6-8 shows the effect of the laser frequency scanning speed on the thermal response when the system is not on an ES (i.e., zero mirror reflectivity, $|r| = 0$) and when it is operated on an ES ($|r| = 1$) with input in the CW mode direction. As expected, thermal broadening decreases with increasing scan speed because at higher speeds the laser scans and passes the resonance very quickly and power build up inside the cavity becomes much smaller than the build up at slower scan rates.

6.3 Conclusion

In this chapter we studied the dynamic thermal behavior of a WGM resonance when the system is operated on an ES. The effect of chiral absorption is seen as the difference in the amount and the lineshape of the broadened resonance for CW and CCW inputs. We have shown that thermal response is significant in the reflection spectra compared to that in the transmission spectra when the system is on an ES.

Chapter 7

Optical Forces in Parity-Time Symmetric Waveguides

7.1 Introduction

In this chapter, we discuss the results of our theoretical studies on optical forces in non-Hermitian photonic systems. We extensively studied the optical forces induced on a dielectric nanoparticle (100 nm in diameter) in a parity-time (PT) symmetric coupled waveguide system where one of the waveguides is lossy and the other has optical gain. We assumed that the waveguides and the particle are in an optofluidic environment. The study is performed considering the optical forces acting on a particle by the symmetric and anti-symmetric modes of the coupled waveguides operating at a wavelength of 1550nm, but the findings can be translated to other spectral domains. The refractive indices of the nanoparticle and optofluidic environment are set to $n_p = 1.56$, and $n_e = 1.33$, respectively. The complex refractive index profile of the waveguides is given by $n = n_R + in_I$, where the n_R and n_I are real and imaginary parts, respectively. We assume that the refractive index profile is spatially symmetric for $n_R(x) = n_R(-x)$ while it is spatially asymmetric for the imaginary part $n_I(x) = -n_I(-x)$ [2]. We performed simulations using Lumerical and in-house developed Matlab codes. We used finite difference time domain (FDTD) method in order to compute the supermodes as well as the propagation of the electromagnetic waves. Maxwell Stress Tensor (MST) analysis is performed within the simulation to calculate the total optical forces acting on the particle in all three dimensions.

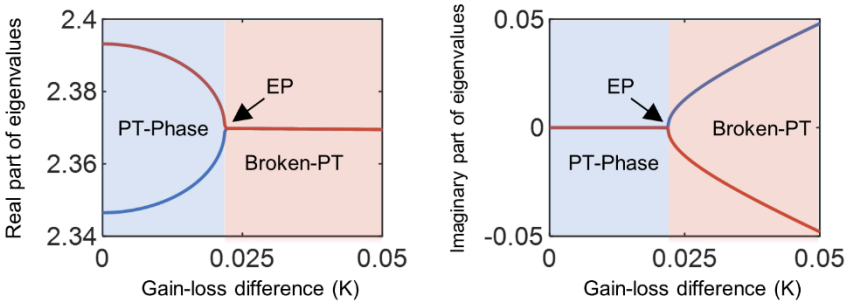

Figure 7-1: The evolution of the real and imaginary parts of eigenvalues of a PT-symmetric coupled waveguides system as a function of gain-loss difference between the waveguides.

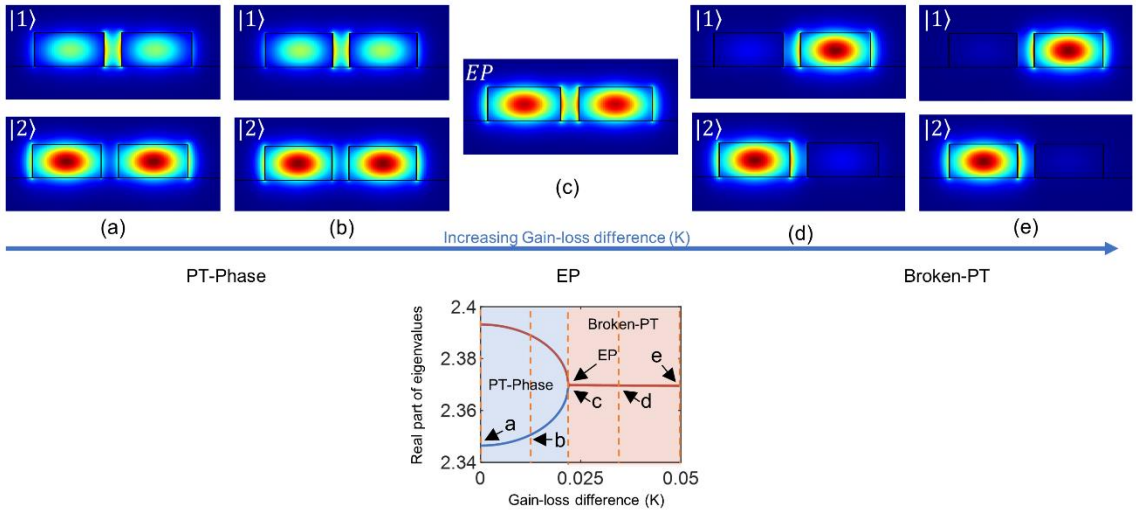

Figure 7-2: The evolution of the real and imaginary parts of eigenvalues of a PT-symmetric coupled waveguides system as a function of gain-loss difference between the waveguides.

A PT-symmetric coupled waveguide system is formed by coupling two waveguides, one of which is lossy and the other has optical gain. If the coupling strength is fixed, one can tune the loss-gain difference to study the evolution of the eigenvalues of the coupled system. Here the gain-loss differences refer to the value of the imaginary part of the refractive index n_I in the loss

waveguide, which is $-n_I$ for the gain waveguide. As seen in Fig. 7-1, when the gain-loss difference is zero, that is the gain in one waveguide compensates the loss in the other waveguide, the eigenmodes bifurcate in their real parts (frequency splitting) if the coupling is sufficiently strong. At the same time, the imaginary parts of the eigenvalues are zero due to balancing gain and loss. As the gain-loss balance is broken and the difference is reduced, the splitting in the real part starts decreasing. At a critical value of the difference, the real parts become exactly the same (they coalesce) and stay the same past this critical point. Meanwhile, the bifurcation takes place in the imaginary parts of the eigenvalues, leading to two supermodes one of which becomes progressively lossy and the other amplifying. The critical point where the bifurcation starts is the EP of the system. The region with splitting in the real parts is known as exact PT-phase whereas the region with splitting in the imaginary parts is known as the broken PT-phase. The eigenmodes corresponding to the eigenvalues in the exact PT-phase denoted as $|1\rangle$, and $|2\rangle$ correspond to the symmetric and antisymmetric modes, respectively. If the propagation constant of the single waveguide is $\beta_0 = \beta_R + i\beta_I$, in the PT-symmetric coupled waveguide system, the propagation constants of the supermodes are given by,

$$\beta_{\mp} = \beta_R \mp \sqrt{k^2 - {\beta_I}^2} \qquad (7.1)$$

An illustration of the the system is given in Fig. 7-3, together with the electric field distributions of a single waveguide, and that of symmetric and asymmetric modes in a coupled system. It is seen that the field of the symmetric mode mostly localized in the region between the waveguides whereas the asymmetric mode is mostly localized in the waveguides.

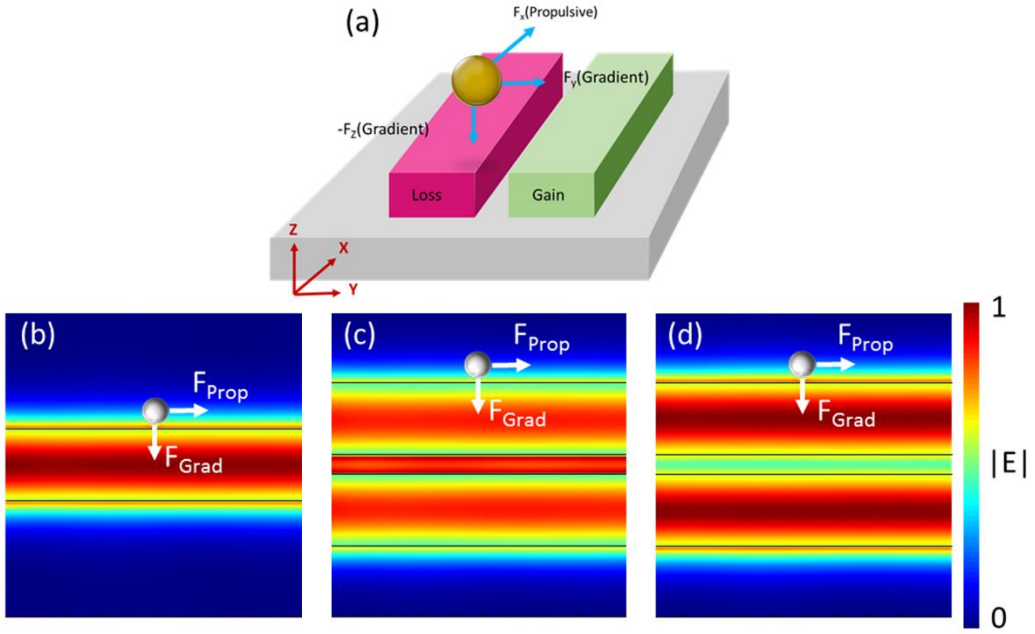

Figure 7-3: (a) Schematics illustration of the problem: a PT-symmetric coupled waveguide system inducing force on a nanoparticle inside a microfluidic channel. (b) Crossection of the electric field profile of TE mode supported by a single waveguide and acting forces F_{prop} (propulsive force) and F_{Grad} (gradient force) on the particle, (c) crossection of electric field profile of TE symmetric mode, (d) crossection of electric field profile of TE asymmetric mode.

7.2 Optical Forces on the particle in the exact and broken PT-phases and at the EP

Coupling strength and the loss-gain difference are two knobs that can be used to control eigenmodes and eigenvalues of the system, as well as to control optical forces acting on the particle. Figure 7-4 shows the profiles of propulsive force (in x-direction) and gradient forces (in y and z-directions) acting on the particle placed in the gap between the waveguides as a function of imaginary parts n_I of the refractive index of the waveguides (i.e., gain-loss difference).

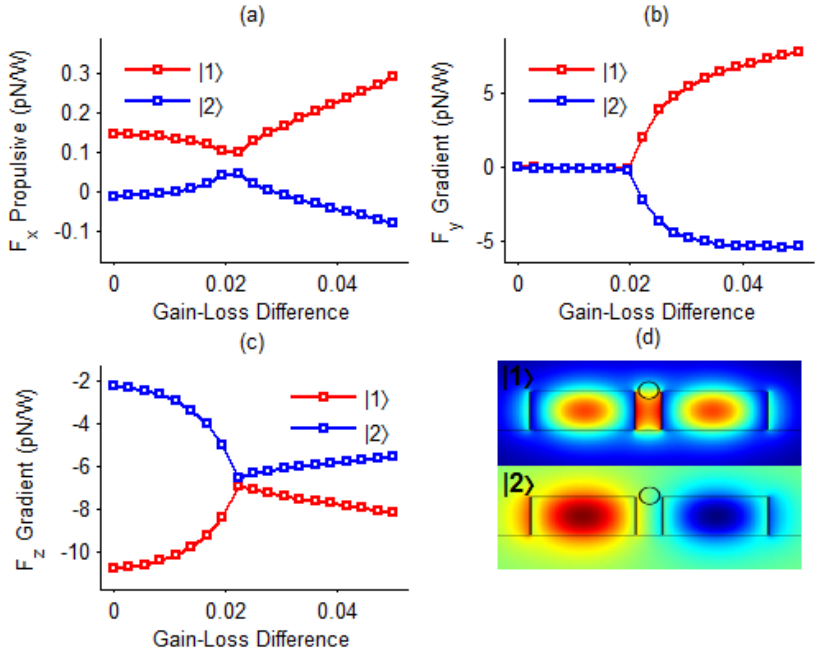

Figure 7-4: Propulsive and gradient forces induced by symmetric, |1⟩ , and asymmetric, |2⟩, modes, acting on the particle positioned in the gap between coupled waveguides. (a) propulsive force in x-direction (the direction of the light propagation), (b) gradient forces in y-direction, (c) gradient force in z-direction, (d) field distributions of symmetric |1⟩ and asymmetric |2⟩ modes.

We first recall that in a coupled waveguide system, the symmetric mode |1⟩ is mostly concentrated in the gap region between the waveguides and the asymmetric mode |2⟩ mostly confined in the waveguides. This difference will show itself on the forces they exert on a particle in the gap between the waveguides. As we see in Fig. 7-4a, in the exact PT-phase (the region defined by gain-loss difference between 0 and ~0.02), the scattering force F_x (propulsive force) exerted on the particle in the direction of light propagation is higher for the symmetric mode because this mode has higher intensity in the gap. However, as the gain-loss balance is varied and the system gradually approaches the EP, symmetric and asymmetric modes approach to each other, starting to overlap and becomes identical exactly at the EP. Thus, at the EP we have coalesced modes and the force exerted on the particle is due to this coalesced mode. In the vicinity of the EP, there still exist two modes but these modes are neither symmetric nor asymmetric (i.e., they have

both components, and one can only say one mode is dominantly symmetric or antisymmetric). As a result, as the system approaches the EP, field distributions of the fields changes and F_x exerted by the symmetric mode decreases whereas that exerted by the asymmetric mode increases until they meet at the EP. As the gain-loss difference is further varied such that the system passes the EP, one of the modes progressively becomes localized in the waveguide with gain and thus the force it exerts on the particle increases whereas the other mode becomes more and more localized in the loss waveguide and thus force it exerts on the particle decreases as the system moves away from the EP. A remarkable observation here is that when the system passes from exact to broken PT-phase through the EP, the force exerted by the mode which is being more localized in the lossy waveguide changes its direction (a transition from $F_x > 0$ to $F_x < 0$) while the force exerted by the other mode localized in the gain waveguide stays $F_x > 0$. This suggests that by controlling the gain-loss difference by exciting the proper mode one can control the direction of the propulsive (scattering) force.

The gradient force F_y in y- direction (i.e., the force pulling the particle in the gap towards or away from the waveguides depending on the field gradient), however, is zero in this exact PT-phase region because both the symmetric and asymmetric fields are distributed symmetrically (Fig. 7-4b). This symmetric distribution of the fields does not change as we vary the gain-loss difference. Thus, the particle in the gap is pulled towards the waveguides (in opposite directions) with equal amounts of gradient forces, and thus the net force on the particle is zero ($F_y = 0$). However, as the system passes the EP, and one mode becomes localized in the lossy and the other in the gain waveguide, F_y is no longer zero because the gradient forces exerted by the fields in the waveguides cannot cancel each other. The mode localized in the gain waveguide will pull the particle towards the gain waveguide ($F_y > 0$) and the mode localized in the lossy waveguide will pull the particle to the lossy waveguide ($F_y < 0$) as seen in Fig. 7-3b. The positive and negative sign just implies

the direction of the force. In Figure 7-4 I we observe that both of the $|1\rangle$, and $|2\rangle$ modes are applying a negative force in the z-direction, which is due to the fact that the highest intensity of the field is located below the position of the particle.

These simulations suggest that by tuning the PT-symmetric coupled waveguides properly and by the correct excitation profile, we can control the optical forces exerted on a particle located in the gap between the waveguides. One can for example control the magnitude and direction of the force which could be used for particle trapping, accelerated particle drive, or changing the movement direction of the particle in the three-dimensional space of the optofluidic medium.

Next, we performed the same study for a particle located beside the lossy waveguide and not in the gap between the waveguides. The results are presented in Fig. 7-5. We find that propulsive forces in x-direction have negative values in the PT-broken regime revealing that the particle is pulled backward in the negative x-direction, while light is propagating in the positive x-direction. This could be explained as follows: The particle is positioned close to the lossy waveguide, and in the PT-broken regime the intensity of the mode $|2\rangle$, which is concentrated in the lossy waveguide, decreases in the positive x-direction. As a result of the attenuation, the particle experiences a negative field gradient and thus is pulled back towards the higher intensity region. This gradient force is enhanced by increasing the balanced gain and loss in the system. This gradient force overcomes the scattering force, which is acting in the positive x-direction, in the PT-broken regime. When $n_I = 0.025$, the propulsive force experiences a zero-crossing, which is the trapping position for the particle.

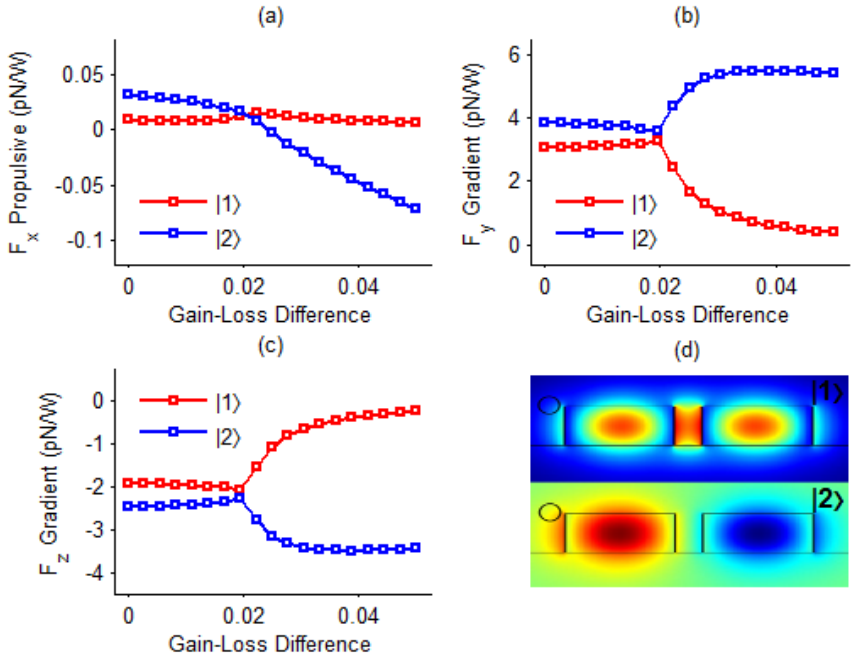

Figure 7-5: Propulsive and gradient forces induced by symmetric, $|1\rangle$, and asymmetric, $|2\rangle$, modes, acting on the particle positioned beside the waveguide with loss. (a) Propulsive force in x-direction (the direction of the light propagation), (b) Gradient forces in y-direction, (c) Gradient force in z-direction, (d) symmetric $|1\rangle$ and asymmetric $|2\rangle$ modes supported by the waveguides.

7.3 Generalized Wigner Smith Operator and Optimizing Eigenmodes Methods

In order to better understand whether the forces observed in PT-symmetric coupled waveguide systems are the optimal or maximal forces, we compared them with the values obtained in two different approaches: Generalized Wigner-Smith (GWS) operator and Eigenmode Optimization (Oei). For these, we excited the superposition of the supported supermodes of the system with proper amplitude and phase.

Generalized Wigner-Smith (GWS) operator, Q operator, is defined for Hermitian systems as,

$$Q = -iS^{-1}\frac{dS}{d\alpha} \qquad (7.2)$$

where S is the scattering matrix, and α could be an arbitrary variable of the system, such as the position of a particle, momentum, frequency or time [17]. The derivative with respect to α in the above definition gives the Wigner-Smith operator for the variable that is conjugate to α. For example, for the conjugate variables frequency and time one should take the derivative of the S-matrix with respect to the frequency to obtain the Wigner-Smith time-delay operator. In our case, since we want to find the force acting on the particle or momentum transferred to the particle, we need to calculate the Wigner-Smith operator for momentum by taking the derivative of the scattering matrix with respect to position, which is conjugate to momentum (i.e., the conjugate quantity of the momentum is the position, therefore we use the derivative of the S-matrix with respect to the particle position, $\frac{dS}{dx}$). If the coupled waveguide system supports orthogonal eignenmodes $|u_\alpha^i\rangle$ one can write

$$Q_\alpha|u_\alpha^i\rangle = \lambda_\alpha^i|u_\alpha^i\rangle \qquad (7.3)$$

where the λ_α^i are the eigenvalues of the Q_α [17]. The eigenvector associated with the maximum eigenvalue corresponds to the mode which exerts the maximum force on the particle.

In this study, we performed FDTD simulations of our system for various particle positions to reconstruct the S-matrix of the system. This S-matrix is used to calculate the GWS operator and its eigenvalues as well as the associated eigenmodes. Then we determined the largest eigenvalue and the associated eigenmode using a Matlab code. Finally, we performed FDTD simulations in which the system is excited with the eigenmode associated with the largest eigenvalue to find the field profile in the system. This field profile is used in MST to calculate the forces acting on the particle. We found that 1) the field is always focused on the location of the particle and thus applies the maximum force on the particle in that specific position, and 2) the propulsive force exerted on the particle by exciting the superposition mode, which is the linear combination of the symmetric and asymmetric modes calculated by the GWS method, has magnitude two times greater than the

force exerted on the particle when either symmetric or asymmetric mode is excited, which implies that GWS provides the eigenmode with the highest force at the position of the particle.

Since we want to calculate the maximum force acting on the particle in a non-Hermitian PT-symmetric system, we employed an alternative method called the Eigenmode Optimization (Oei), which can be used both for non-Hermitian and Hermitian systems. The Oei method calculates the optimized eigenmode to be excited by utilizing the quadratic dependence of light and matter interactions, which could be written as [18];

$$m^{(A)}(E,H) = a^{\dagger} M^{(A)} a \qquad (7.4)$$

Here, E and H represents the electric and magnetic fields, respectively, (A) denotes the light-matter interaction, which in our case is represented by the momentum transferred to the particle. The momentum operator $m^{(F)}(E,H)$ calculates the momentum transferred to the particle by the field composed of the specific E and H components. If E_j represent the supported modes, a and $a^{\dagger}$ are the vectors of the superposition mode with the weights a_j, the superposition is given by,

$$\{E,H\} = \{\sum_{j=1}^{N} a_j E_j, \sum_{j=1}^{N} a_j H_j,\} \qquad (7.5)$$

In our specific case, we have two orthogonal eigenmodes and thus N is equal to 2. The elements of the matrix M are given by [18],

$$4M_{jk}^{(F)} = m^{(F)}\left(E_j + E_k, H_j + H_k\right) - im^{(F)}\left(E_j + iE_k, H_j + iH_k\right) - m^{(F)}\left(E_j - E_k, H_j - H_k\right) + im^{(F)}\left(E_j - iE_k, H_j - iH_k\right) \qquad (7.6)$$

After determining the optimized eigenmode (i.e., superposition state of E and H with specific weights) using a Matlab code, we excited this optimized mode in FDTD simulations and calculated the momentum transferred to the particle. Similar to the GWS method, the eigenmode of M matrix associated with the largest eigenvalue leads to the highest force exerted on the particle. The field distributions obtained using the results of GWS and the Oei methods are very similar at any particle position. Thus, the highest forces exerted on the particle are also the same. Figure 5

represents the field distribution of the eigenmodes associated with the largest eigenvalues obtained from GWS and Oei methods. The force values on the particle calculated by these two methods are close to each other and higher than the values calculated if only symmetric or asymmetric mode is excited: $F_{x(OEi)} = 59.92\ pN/W$, and $F_{x(GWS)} = 54.96\ pN/W$, while $F_{x(|1\rangle)} = 29.2\ pN/W$, and $F_{x(|2\rangle)} = 30.86\ pN/W$.

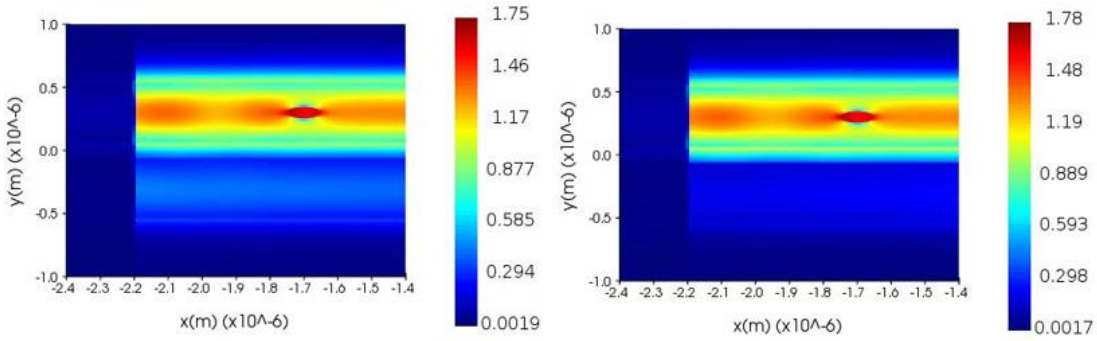

Figure 7-6: Field profile of the superposition mode determined using (left) GWS operator and (right) Oei. The force exerted on the particle are $F_{x(GWS)} = 54.96\ pN/W$ and $F_{x(OEi)} = 59.92\ pN/W$.

7.4 Optimizing Eigenmodes method in PT-Symmetrically Coupled Waveguides

Using the optimizing eigenmodes (Oei) method, and the generalized Wigner-Smith (GWS) operator, we successfully optimized the propulsive optical forces acting on the particle inside the waveguide in the previous section, where the coupled waveguide system had no gain and loss, and the radiation losses in the system were negligible. Thus, the system was considered as Hermitian. GWS operator could be used for Hermitian systems, however, one can use the Oei for both Hermitian and non-Hermitian systems.

The optical forces acting on the particle in three directions is presented in the Figure 7-7. The particle is assumed to be on the gain waveguide. The EP emerges at the gain-loss difference value of 0.21. In the broken-PT regime the first mode $|1\rangle$, corresponds to the mode inside the gain waveguide, and the second mode $|2\rangle$, corresponds to the mode in the loss waveguide. Enhancement

of the propulsive forces (i.e., F_x, and Figure. 7-7(a)) after the EP for the mode in the gain waveguide is clear. On the other hand, the propulsive force due to mode $|2\rangle$ decreases. In Figure 7-7(b) since the symmetric mode is mainly concentrated in the middle of two waveguides the gradient forces in Y-direction are negative for $|1\rangle$, and positive for $|2\rangle$. After EP, due to the amplification of the mode $|1\rangle$, the forces become positive in an increasing manner in both of the gradient forces in Y and Z directions.

With the trend of forces shown in Fig. 7-7 for a PT-symmetric system (without optimization), we turned our attention to optimized eigenmode analysis for the PT-symmetric waveguides. For each gain-loss difference value, we found the optimized eigenmode and thus the optimized force it exerts on the particle. As it is seen in Figure 7-8, in this PT-symmetric waveguides system, we could successfully find the optimized eigenmode and compute the associated forces in the exact and broken PT-phases as well as the at the EP. In the exact PT-phase and at the EP, forces exerted by the optimized eigenmode obtained from Oei method is larger than or equal to the forces exerted by the symmetric and asymmetric modes. However, after the EP and in the PT-broken regime, the optical forces acting via $|1\rangle$ is larger. We note that in this study, we have considered the particle at a specific location on the gain waveguide. In order to further assess PT and optical forces in comparison with the optimized eigenmode from Oei method, we will continue the study by looking at the cases where particles are located in different locations.

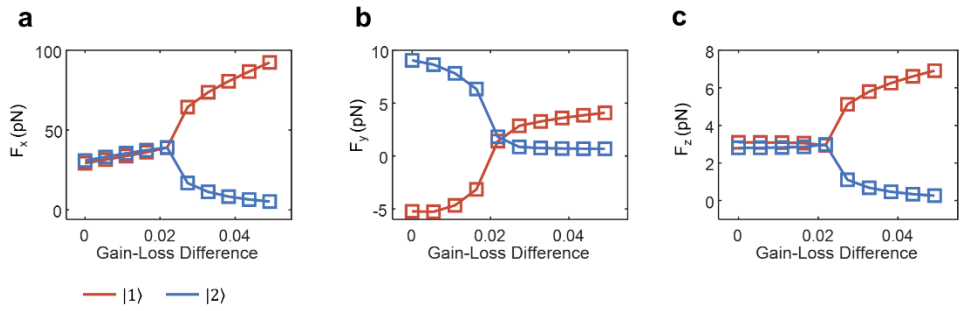

Figure 7-7: Forces acting on particle in (a) x-direction (i.e., propulsive forces), (b) y-direction (i.e., gradient forces in y-direction), (c) z-direction (i.e., gradient forces in z-direction). Red and blue curves are for |1⟩ and |2⟩ modes, respectively.

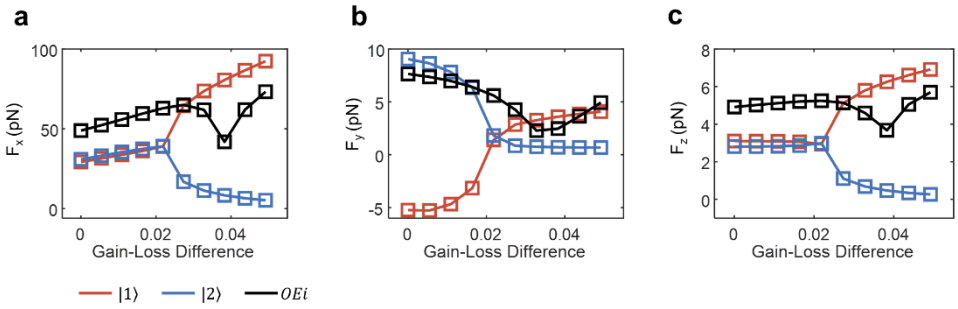

Figure 7-8: Optimized forces with Oei (black curve), compared to Forces acting on particle in (a) x-direction (i.e., propulsive forces), (b) y-direction (i.e., gradient forces in y-direction), (c) z-direction (i.e., gradient forces in z-direction). Red and blue curves are for |1⟩ and |2⟩ modes, respectively.

7.5 Conclusion

In this chapter, the optical forces acting on the particle in a PT-symmetrically coupled waveguides systems is calculated via Maxwell Stress Tensor. Additionally, using GWS operator and Oei method, and for the Hermitian case (i.e., no gain and loss in the waveguides) we could increase the propulsive forces acting on the particle by optimizing the excited superposition of two modes, which clearly presented that by exciting the modes found from GWS and Oei the propulsive

forces can be increased. Similarly, we employed Oei in a coupled gain-loss waveguide system and found optimized eigenvalues that maximizes the forces. We then compared these values of forces with the forces obtained when either of the symmetric or asymmetric modes is excited. Our results show that modes found using Oei provides more force than the symmetric and asymmetric modes in the exact PT-phase while in the broken PT-phase this reverses and the excitation of the mode which is located in the gain waveguide becomes larger.

References

[1] T. Kato, Perturbation Theory of Linear Operators (Springer, Berlin, 1966).

[2] Özdemir, Ş. K., Rotter, S., Nori, F. & Yang, L. Parity-time symmetry and exceptional points in photonics. *Nat. Mater.* **18,** 783-798 (2019).

[3] El-Ganainy, R. *Et al.* Non-Hermitian physics and PT symmetry. *Nat. Phys.* **14**, 11–19 (2018).

[4] Miri, M. A. & Alù, A. Exceptional points in optics and photonics. *Science* **363**, eaar7709 (2019).

[5] Feng, L., El-Ganainy, R. & Ge, L. Non-Hermitian photonics based on parity-time. *Nat. Photon*. **11**, 752–762 (2017).

[6] El-Ganainy, R., Khajavikhan, M., Christodoulides, D. N. & Özdemir, Ş. K. The dawn of non-Hermitian optics. *Commun. Phys.* **2**, 37 (2019).

[7] Berry, M. V. M. The Adiabatic Phase and Pancharatnam's Phase for Polarized Light. *J. Mod. Opt*. **34**, 1401-1407 (1987).

[8] Yarkony, D. R. Diabolical conical intersections. *Rev. Mod. Phys.* **68**, 985–1013 (1996).

[9] Peng, B. et al. Chiral modes and directional lasing at exceptional points. *Proc. Natl. Acad. Sci. U.S.A.* **113,** 6845-6850 (2016).

[10] Chen, W., Özdemir, Ş. K., Zhao, G., Wiersig, J. & Yang, L. Exceptional points

enhance sensing in an optical microcavity. *Nature* **548**, 192-196 (2017).

[11] Hodaei, H. *et al.* Enhanced sensitivity at higher-order exceptional points. *Nature* **548**, 187–191 (2017).

[12] Lau, H.-K. & Clerk, A. A. Fundamental limits and non-reciprocal approaches in non-Hermitian quantum sensing. *Nat. Commun.* **9**, 1–13 (2018).

[13] Lai, Y.-H., Lu, Y.-K., Suh, M.-G., Yuan, Z. & Vahala, K. Observation of the exceptional-point-enhanced Sagnac effect. *Nature* **576**, 65–69 (2019).

[14] Hokmabadi, M. P., Schumer, A., Christodoulides, D. N. & Khajavikhan, M. Non-Hermitian ring laser gyroscopes with enhanced Sagnac sensitivity. *Nature* **576**, 70–74 (2019).

[15] Wang, H., Lai, Y.-H., Yuan, Z. , Suh, M.-G., and Vahala, K. Petermann-factor sensitivity limit near an exceptional point in a Brillouin ring laser gyroscope. *Nat. Comm.* **11**, 1610 (2020).

[16] Wiersig, J. Review of exceptional point-based sensors. *Photon. Res.* **8**, 1457-1467 (2020).

[17] Park, JH., Ndao, A., Cai, W. *et al*. Symmetry-breaking-induced plasmonic exceptional points and nanoscale sensing. *Nat. Phys.* **16**, 462–468 (2020).

[18] Guo, A. *et al*. Observation of PT-Symmetry Breaking in Complex Optical Potentials. *Phys. Rev. Lett.* **103**, 093902 (2009).

[19] Peng, B. *et al.* Loss-induced suppression and revival of lasing. *Science* **346**, 328–332 (2014).

[20] Brandstetter, M. *et al*. Reversing the pump dependence of a laser at an

exceptional point. *Nat. Commun*. **5**, 4034 (2014).

[21] Bender, C. M., and Boettcher, S. Real spectra in non-Hermitian Hamiltonians having PT symmetry. *Phys. Rev. Lett.* **80**, 5243–5246 (1998).

[22] Peng, B. *et al*. Parity-time-symmetric whispering-gallery microcavities. *Nat. Phys.* **10**, 394-398 (2014).

[23] Rüter, C. E. *Et al*. Observation of parity-time symmetry in optics. *Nat. Phys.* **6**, 192-195 (2010).

[24] Jing, H., Ozdemir, S. K., Lu, X.-Y., Zhang, J., Yang, L. and Nori, F. PT-symmetric phonon laser. *Phys. Rev. Lett.* **13**, 053604 (2014).

[25] Zhen, B. *et al*. Spawning rings of exceptional points out of Dirac cones. *Nature* **525**, 354-358 (2015).

[26] Zhang, J. *et al*. A phonon laser operating at an exceptional point. *Nat. Photon.* **12**, 479–484 (2018).

[27] Naghiloo, M., Abbasi, M., Joglekar, Y.N. & Murch, K.W. Quantum state tomography across the exceptional point in a single dissipative qubit. *Nat. Phys.* **15**, 1232-1236 (2019).

[28] Xiao, L. *et al*. Observation of critical phenomena in parity-time-symmetric quantum dynamics. *Phys. Rev. Lett.* **123**, 230401 (2019).

[29] Xu, H., Jiang, L., Clerk, A.A. & Harris, J.G.E. Nonreciprocal control and cooling of phonon modes in an optomechanical system. *Nature* **568**, 65-69 (2019).

[30] Zhong, Q. et al. Sensing with exceptional surfaces in order to combine sensitivity with robustness. *Phys. Rev. Lett.* **122,** 153902 (2019).

[31] McDonald, A. & Clerk, A.A. Exponentially-enhanced quantum sensing with non-Hermitian lattice dynamics. *Nat Commun* **11**, 5382 (2020).

[32] Zhong, Q., Hashemi, A. , Ozdemir, S. K., and El-Ganainy, R. Control of spontaneous emission dynamics in microcavities with chiral exceptional surfaces. *Phys. Rev. Research* **3**, 013220 (2021).

[33] M. Khanbekyan and J. Wiersig, Decay suppression of spontaneous emission of a single emitter in a high-Q cavity at exceptional points. *Phys. Rev. Research* **2**, 023375 (2020).

[34] Zhou, H., Lee, J. Y., Liu, S., and Zhen, Bo. Exceptional surfaces in $\mathcal{PT}$-symmetric non-Hermitian photonic systems. *Optica* **6**, 190-193 (2019).

[35] Okugawa, R., and Yokoyama, T. Topological exceptional surfaces in non-Hermitian systems with parity-time and parity-particle-hole symmetries. *Phys. Rev. B* **99**, 041202(R) (2019).

[36] Budich, J. C, Carlström, J., Kunst, F. K., and Bergholtz, E. J. Symmetry-protected nodal phases in non-Hermitian systems. *Phys. Rev. B* **99**, 041406® (2019).

[37] Zhang, X., Ding, K., Zhou, X., Xu, J., and Jin, D. Experimental Observation of an Exceptional Surface in Synthetic Dimensions with Magnon Polaritons. *Phys. Rev. Lett.* **123**, 237202 (2019).

[38] Q. Zhong, S.K. Ozdemir, A. Eisfeld, A. Metelmann, and R. El-Ganainy. Exceptional-Point-Based Optical Amplifiers. *Phys. Rev. Applied* **13**, 014070 (2020).

[39] Zhong, Q., Nelson, S., Özdemir, Ş. K. & El-Ganainy, R. Controlling directional absorption with chiral exceptional surfaces. *Opt. Lett.* **44**, 5242-5245 (2019).

[40] Sweeney, W. R., Hsu, C. W., Rotter, S. & Stone, A. D. Perfectly Absorbing Exceptional Points and Chiral Absorbers. *Phys. Rev. Lett.* **122**, 093901 (2019).

[41] Asano, M., Takeuchi, Y., Chen, W., Ozdemir, S. K., Ikuta, R., Imoto, N., Yang, Y., Yamamoto, T., Observation of optomechanical coupling in microbottle resonator. Laser and photonics review, vol. 10, issue. 4, 2016.

[42] Rayleigh, L., The problem of the whispering gallery. Phil. Mag. 20, 1001-1004, 1910.

[43] Lee, H., et. Al., Chemically etched ultrahigh-Q wedge-resonator on silicon chip. Nature Photonics, vol.6, 2019.

[44] Little, B. H., Laine, J. P. and aus, H. A., Anaytic theory of coupling from tapered fibers and half-blocks into microshpere resonators. J Lightwave technology, 17, 704-715, 1999.

[45] Gorodetsky, M. L., and Ilchenko, V. S., Optical microsphere resonators: optimal coupling to high-Q whispering-gallery modes. J opt Soc Am B 16, 147-154, 1999.

[46] Rabiei, P., Steier, W. H., Zhang, C., Dalton, L. R., Polymer micro-ring filters and modulators. J Lightwave Technology 20, 1968-1975, 2002.

[47] Srinivasan, K., Boreselli, M., and Painter, O., Cavity Q, mode volume, and lasing threshold in small diameter AlGaAs microdisks with embeded quantum dots. Opt Express 14, 1094-1105, 2006.

[48] Sakurai, J. J., Napolitano, J. Modern quantum mechanics; Pearson, 2nd ed, 2010.

[49] Özdemir, K., Rotter, S., Nori, F. & Yang, L. Parity–time symmetry and exceptional points in photonics. *Nat. Mater.* (2019) doi:10.1038/s41563-019-0304-9.

[50] Miri, M. A. & Alù, A. Exceptional points in optics and photonics. *Science (80-.).* **363**, (2019).

[51] El-Ganainy, R. *et al.* Non-Hermitian physics and PT symmetry. *Nature Physics* vol. 14 11–19 (2018).

[52] Feng, L., El-Ganainy, R. & Ge, L. Non-Hermitian photonics based on parity-time symmetry. *Nature Photonics* vol. 11 752–762 (2017).

[53] Balci, S. *et al.* Tunable Plexcitonic Nanoparticles: A Model System for Studying Plasmon-Exciton Interaction from the Weak to the Ultrastrong Coupling Regime. *ACS Photonics* (2016) doi:10.1021/acsphotonics.6b00498.

[54] Thomas, P. A., Tan, W. J., Fernandez, H. A. & Barnes, W. L. A New Signature for Strong Light-Matter Coupling Using Spectroscopic Ellipsometry. *Nano Lett.* (2020) doi:10.1021/acs.nanolett.0c01963.

[55] Zhao, H. *et al.* Non-Hermitian topological light steering. *Science (80-.).* (2019) doi:10.1126/science.aay1064.

[56] Bender, C. M. & Boettcher, S. Real spectra in non-hermitian hamiltonians having PT symmetry. *Phys. Rev. Lett.* **80**, 5243–5246 (1998).

[57] Wiersig, J. Sensors operating at exceptional points: General theory. *Phys. Rev. A* **93**, 1–9 (2016).

[58] Pick, A. *et al.* General theory of spontaneous emission near exceptional points. *Opt. Express* **25**, 12325 (2017).

[59] Peng, B. *et al.* Loss-induced suppression and revival of lasing. *Science (80-.).* **346**, 328–332 (2014).

[60] Xu, H., Mason, D., Jiang, L. & Harris, J. G. E. Topological energy transfer in an

optomechanical system with exceptional points. *Nature* (2016) doi:10.1038/nature18604.

[61] Sweeney, W. R., Hsu, C. W., Rotter, S. & Stone, A. D. Perfectly Absorbing Exceptional Points and Chiral Absorbers. *Phys. Rev. Lett.* **122**, 093901 (2019).

[62] Zhang, J. *et al.* A phonon laser operating at an exceptional point. *Nature Photonics* vol. 12 479–484 (2018).

[63] Kim, J. *et al.* Practical lineshape of a laser operating near an exceptional point. *Sci. Rep.* **11**, 6164 (2021).

[64] Peng, B. *et al.* Parity-time-symmetric whispering-gallery microcavities. *Nat. Phys.* (2014) doi:10.1038/nphys2927.

[65] Xu, H., Mason, D., Jiang, L. & Harris, J. G. E. Topological energy transfer in an optomechanical system with exceptional points. *Nature* **537**, 80–83 (2016).

[66] Geiser, M., Scalari, G., Castellano, F., Beck, M. & Faist, J. Room temperature terahertz polariton emitter. *Appl. Phys. Lett.* **101**, (2012).

[67] Shi, C. *et al.* Accessing the exceptional points of parity-time symmetric acoustics. *Nat. Commun.* **7**, 1–5 (2016).

[68] Li, Y. *et al.* Anti-parity-time symmetry in diffusive systems. *Science (80-.).* (2019) doi:10.1126/science.aaw6259.

[69] Kakenov, N., Ergoktas, M. S., Balci, O. & Kocabas, C. Graphene based terahertz phase modulators. *2D Mater.* **5**, (2018).

[70] Brown, E. R., Bjarnason, J. E., Fedor, A. M. & Korter, T. M. On the strong and narrow absorption signature in lactose at 0.53 THz. *Appl. Phys. Lett.* **90**, 2005–2008 (2007).

[71] Ernzerhof, M., Giguère, A. & Mayou, D. Non-Hermitian quantum mechanics and exceptional points in molecular electronics. *J. Chem. Phys.* **152**, 244119 (2020).

[72] Flick, J., Ruggenthaler, M., Appel, H. & Rubio, A. Atoms and molecules in cavities, from weak to strong coupling in quantum-electrodynamics (QED) chemistry. *Proc. Natl. Acad. Sci. U. S. A.* **114**, 3026–3034 (2017).

[73] Graf, A. *et al.* Electrical pumping and tuning of exciton-polaritons in carbon nanotube microcavities. *Nat. Mater.* **16**, 911–917 (2017).

[74] Kang, E. S. H. *et al.* Strong Plasmon-Exciton Coupling with Directional Absorption Features in Optically Thin Hybrid Nanohole Metasurfaces. *ACS Photonics* **5**, 4046–4055 (2018).

[75] Ilchenko, V. S. & Matsko, A. B. Optical resonators with whispering-gallery modes-part II: applications. *IEEE J. Sel. Top. Quantum Electron.* **12**, 15–32 (2006).

[76] Toropov, N. Review of biosensing with whispering gallery mode lasers, Nature, 10, 42, 2021.

[77] Armani, D., Ultra-High-Q Planar Microcavities and applications, PhD Thesis, California Inistitude of Technology, 2005.

[78] Kippenberg, T. J. A. Nonlinear optics in ultra-high-Q whispering-gallery optical microcavities, PhD thesis, California Inistitude of Technology, 2004.

[79] He, L. Whisperring gallery mode microresonators for lasing and singl nanoparticle detection, PhD thesis, Washington University in St. Louis, 2012.

VITA

Sina Soleymani

Sina Soleymani received his M.Sc. and B.Sc. degrees in nanotechnology engineering (Nanoelectronics) and electrical engineering (Electronics) from University of Tabriz in 2015, and University of Bonab in 2013, respectively. After three years of professional electronic circuit designing, he was awarded graduate council fellowship from University of Alabama (UA) in 2017, and he joined Electrical Engineering department, UA, in order to complete his education in photonics and in PhD level. In 2018 he joined the Engineering Science and Mechanics department of the Pennsylvania State University to continue his Ph.D. His research interests include non-Hermitian photonics, parity-time symmetric photonics, and optomechanics.

Selected Publications:

1. S. Soleymani et. al, "Chiral Coherent Perfect Absorption on Exceptional Surfaces" https://arxiv.org/abs/2107.06019
2. M. S. Ergoktas, et. al, "non-Hermitian engineering of terahertz light using exceptional points in electrically tunable collective light-matter interactions" https://arxiv.org/abs/2108.12033
3. Sina Soleymani, M. Z. Güngördü, P. Kung, S. M. Kim "Ultra-High Efficiency and Broad Band Operation of Infrared Metasurface Anomalous Reflector based on Graphene Plasmonics" Scientific Reports 9(1), 1249, 2019.
4. S. Soleymani and S. Golmohammadi, "Surface Plasmon Polaritons Propagation along Armchair Single-Wall Carbon Nanotubes with Different Radii" IEEE Transaction on Nanotechnology, 2017.
5. D. C. Ullery, S. Soleymani, A. Heaton, J. Orphee, L. Johnson, R. Sood, P. Kung, S. M. Kim, "Strong Solar Radiation Forces from Anomalously Reflecting Metasurfaces for Solar Sail Attitude Control" Scientific Reports, 8(1), 10026, 2018.